An Experimental Investigation of Aerodynamics and Flow Characteristics of Slender and Non-Slender Delta Wings

Muneeb Dogar

Department of Mechanical Engineering
McGill University, Montreal, Quebec, Canada
April 2012

Thesis submitted to McGill University in partial fulfillment of the requirements of the degree of Master of Engineering

Acknowledgements

The author owe an immerse debt of gratitude to Professor Tim Lee for his continuous support, patience and invaluable guidance over the past two years. Without his encouragement and suggestions this thesis would never has materialized in its present form. Furthermore, the author wishes to express his appreciation for colleagues at Experimental Aerodynamics Laboratory; Jennifer Pereira, Lok Sun Ko, Hafiz Laiq-ur-Rehman, Ying Yu Su and Gautum Virdi. More personally, the author would like to thank his siblings, parents and Omer Sheikh for their emotional presence and inspiration. A special mention goes to his beloved wife ‘Aana’ for providing him with emotional and motivational support.

Abstract

The leading-edge vortical flow structure over a 65° slender (DW65) and a 50° non-slender (DW50) delta wing was investigated at Reynolds number of order 10^5. Particular emphasis was placed in the variation of vortex flow quantities and critical flow parameters with change in angle of attack and chordwise distance. In addition, the progression of vortex breakdown with angle of attack was documented based on pressure and three-dimensional velocity information. A glimpse of wake-vortex evolution was also discussed. Moreover, aerodynamic lift and drag forces were evaluated based on wake survey analyses and compared with direct force balance measurements. Special attention was focused on drag characterization based on lift dependency where Maskell formulation was adopted for the estimation of induced drag. The results showed that the flow over DW65 and DW50 has some qualitative resemblances but quantitatively they are two contrasting flows. Prior to the breakdown, in the case of DW65, the vortical flow is near-axisymmetric but in the case of DW50, the vortex and axial core never matches and even the definition of distinctive vortex center is often ambiguous except at higher angles of attack, moreover the axial core was always accompanied by large momentum deficit. The variation of vortex flow quantities in streamwise direction showed self-similar behavior when plotted against radial distance scaled by local semi-span while interestingly for DW50 self-similar behavior was showed only by the variation of total pressure loss about the pressure core. It was established that the flow over DW50 was marred by an active interaction of vortical and boundary layer flow due to the close proximity of vortex to the wing surface. For the first time the progression of vortex breakdown over the wing surface was reported on the basis of three-dimensional flow information which elucidated the respective indicators of breakdown for slender and non-slender delta wings. Lastly, wake survey analyses were carried and comparison of different lift computational models and direct measurement were presented. Moreover, the estimation of profile drag is sensitive to the definition of wake region whereas vortex breakdown upstream of trailing-edge resulted in underestimation and overestimation of induced drag and C_L, respectively. For all the cases of slender wing and high angle of attack cases of non-slender delta wing showed that the induced drag always constituted more than 50% of the total drag. The results provided here provided a deepened and extended insight on vortical and aerodynamics characteristics of slender and non-slender delta wing.

Résumé

La structure de pointe d’écoulement tourbillonnaire d’une aile delta élancée à 65 ° (DW65) et non élancée à 50 ° (DW50) a été étudiée au nombre de Reynolds de l'ordre 10^5. Un accent particulier a été mis dans la variation des quantités d’écoulement tourbillonnaire et les paramètres d’écoulement critique avec un changement de l'angle d'attaque et de la distance en corde. En outre, la progression de l’éclatement du tourbillon avec l'angle d'attaque a été documentée sur la base de la pression et de l’information sur la vitesse tridimensionnelle. On a également discuté d’un aperçu de l’évolution de la turbulence de sillage. De plus, les forces aérodynamiques de portance et de traînée ont été évaluées sur la base des analyses de l'enquête sur le sillage et comparées avec des mesures directes de l'équilibre des forces. Une attention particulière a été portée sur la caractérisation de la traînée fondée sur la dépendance de la portance où la formulation de Maskell a été adoptée pour l'estimation de la traînée induite. Les résultats ont montré que l'écoulement sur DW65 et DW50 ont quelques ressemblances qualitatives, mais elles sont quantitativement deux écoulements contrastés. Avant l’éclatement, dans le cas de DW65, l'écoulement tourbillonnaire est quasi axisymétrique, mais dans le cas de DW50, le tourbillon et le noyau axial ne correspondent jamais et même la définition de centre du tourbillon distinctif est souvent ambiguë, sauf à des angles d'attaque plus élevés. D'ailleurs, le noyau axial était toujours accompagné par un déficit dynamique important. La variation de la quantité d'écoulement tourbillonnaire dans la direction de l'écoulement a montré un comportement auto similaire lorsqu'elle est portée contre la distance radiale réduite par semi-envergure locale. Pendant que, fait intéressant, pour la DW50, un comportement auto similaire a été montré seulement par la variation de la perte de pression totale aux environs du *cœur* de la pression. Il a été établi que l'écoulement sur DW50 a été marqué par une interaction active de l'écoulement tourbillonnaire et de la couche limite en raison de la proximité du tourbillon de la surface de l'aile. Pour la première fois, la progression de l’éclatement du tourbillon sur la surface de l'aile a été signalée sur la base de l’information du système d'écoulement tridimensionnel qui a élucidé les indicateurs respectifs d’éclatement pour les ailes delta élancées et non élancées. Enfin, les analyses des enquêtes ont été menées et des comparaisons de différents modèles informatiques de portage et de mesure directe ont été présentées. En outre, l'estimation de la traînée de profil est sensible à la définition de la région de sillage tandis que l’éclatement tourbillonnaire en amont du bord de fuite a entraîné une sous-estimation et une surestimation de la traînée induite et du C_L, respectivement. Pour tous les cas de l'aile élancée et les cas de l'angle d'attaque de l’aile delta non élancée ont montré que la traînée induite a toujours constitué plus de 50% de la traînée totale. Les résultats fournis ici ont fourni un aperçu approfondi et étendu sur les caractéristiques tourbillonnaires et aérodynamiques de l'aile delta élancée et non élancée

Table of Contents

Nomenclature

AR	Aspect ratio, b^2/s
b	wing Span
c	wing chord
C_D	drag coefficient, $D/\frac{1}{2}\rho U_\infty^2 S$
C_L	lift coefficient, $L/\frac{1}{2}\rho U_\infty^2 S$
$C_{l\alpha}$	lift curve slope = $dC_l/d\alpha$
D	drag force
DW65_a10_x0.4	65^o delta wing at an $\alpha = 10^o$ and $x/c = 0.4$
D_i	lift-induced drag
D_p	profile drag
K_p	potential lift coefficient
K_v	vortex lift coefficient
L	lift force
LEV	leading-edge vortex
P	total pressure
PV	primary vortex
p	static pressure
q	dynamic pressure, $\frac{1}{2}\rho U_\infty^2 S$
Re	Reynolds number, $\rho c U_\infty/\mu$
r	radial coordinate
rms	root mean squared
SV	secondary vortex

S	wing planform area
s	wing semi span, b/2
t/c	thickness to chord ratio
u, v, w	streamwise, traverse and spanwise velocity component
u_c	core axial velocity
VBD	vortex breakdown
x, y, z	streamwise, traverse and spanwise coordinate
Γ	vortex circulation
α	angle of attack
Δ	grid resolution
Λ	leading-edge sweep angle
ζ	axial vorticity

Subscript

c	core vortex value (bounded by $v_{\theta max}$)
o	outer vortex value (bounded by 99% of asymptotic value)
θ	value about the angular coordinate
∞	free stream value
max	maximum value in a given region
peak	peak value in a given region

Chapter 1

1 Introduction

1.1 Problem Statement

The study of delta wing has been popular among aerodynamicist for decades due to its research and technological significance. Over 150 peer reviewed articles are published every year on related topics. From direct aerodynamic measurements to derived quantities, from static time-averaged measurements to dynamic time-accurate measurements are under investigation since the inception of the planform in the 1950s. A crude classification says that any planform above 55^{o}-60^{o} sweep is said to be a slender delta wing while the planform below this limit are non-slender delta wing.

For several decades, delta wings found their application in combat fighters, supersonic aircrafts and recently in low Reynolds number flight of Micro Air Vehicles (MAVs) as a main lift generating body. They have the ability to form stable vortical structures which can create suction pressure over the wing surface for a range of high incidences. Furthermore, in supersonic conditions the leading-edge remained behind the shock wave generated by the nose of the aircraft which therefore moderates the contribution of wave drag. The coherent vortical structures guarantee the lift increment even at high angles of attack until the vortices suffer the breakdown, typically reported by flow visualization studies. Over the years the static and dynamic behaviour of the delta wings have been extensively studied particularly, slender delta wings. On the other hand, renewed interests attributed to future unmanned and micro air vehicles have highlighted the potential use of non-slender delta wing. This incites the efforts to understand the flow topology and behaviour over the high aspect ratio delta wings (low sweep). Besides the aforementioned advantages, delta wings have some disadvantages. The main adversity lies in the characteristic massive flow separation which not only increases the profile drag but undermines the downstream control surfaces. In addition, the strong cross-flow velocities induce significant lift-induced drag as compared to conventional high aspect ratio wings. Consequently delta wings have poor L/D ratio, hence are less fuel efficient and requires longer take-off and landing strips. Moreover, some of the drawbacks are exclusive of non-slender delta wings where the earlier breakdown further complicates the vortical flow behaviour and intensifies the fluid-structure interactions.

The process of leading-edge vortex formation and evolution is quite complex and hence demands considerable effort to fully understand the related physical mechanisms. Due to the unsteadiness and transient nature of flow, researchers often opt for a selective approach involving a few rationally high angles of attack and certain chordwise locations based on the motive behind the research. Ironically, even for the static cases, the unsteady and transient phenomena overshadow the classical steady flow approximations therefore despite the tremendous research effort the basic aerodynamics of the delta wing are still in question. Besides this lack, technological advancement and state-of-the-art experimental techniques have incited a whole new chapter of parametric studies, extending from exploiting the morphing properties of flexible materials to sophisticated active and passive flow control techniques. This demands a need of extensive insight into the vortical flow behaviour and aerodynamics of the delta wings, especially for the sweep angles in the vicinity of slender-non-slender interface.

1.2 Objective

The purpose of this work was to investigate and characterize the aerodynamics and flow characteristics of slender (65^o) and non-slender (50^o) delta wings in greater detail. This was carried out for a combination of various angles of attack and chordwise stations by using a seven-hole pressure probe (SHP). The ultimate goal of investigation is to document the variation in flow quantities and critical flow parameters with increasing incidence and distance from the wing apex. Furthermore, in contrast to conventional flow visualization methods to report the vortex breakdown locations, information acquired from seven-hole pressure probe was dissected for the documentation of breakdown locations. Detailed wake analyses were conducted for stations aft of the trailing-edge to investigate the wake-vortex evolution along with the indirect determination of aerodynamic loading, paying particular attention to the computation of induced drag.

The author's intention is not to duplicate the existing literature, but to expand the extent of information on the characteristics of leading-edge vortices and flow behaviour in the vicinity of vortex breakdown. It is anticipated that this work will contribute to a deeper understanding of contrasting vortical flow fields over slender and non-slender delta wings. The experimental data can be used for the validation of computational models and as a baseline in parametric studies.

Chapter 2

2 Background

Delta wing aerodynamics is usually dominated by vortex flows which appear over a range of high angle of attacks and were the primary reason for its development in 1950s. Evolutionary defence technologies and modern combats demand high performance and high speed manoeuvres, which involve flights at high angle of attacks and expanding flight envelopes, while in contrast the modern reconnaissance and emerging UAVs and MAVs industries demand low speed lift producing planforms. For such demands, delta wings are often used and the varying aerodynamic performance (high and low speed) can be achieved by varying the sweep angle only. Massive data has been collected and published for slender delta wing planform, even under the umbrella of National Aeronautics and Space Administration (NASA), and often the flow behaviour can be accurately predicted. On the other hand limited literature has been published for low sweep delta wings. The behavioural shift in aerodynamics and flow properties is quite visible with changes in sweep angle.

At higher incidences, the potential (attached flow) lift generation by streamlined airfoil section is haunted by the upstream progression of a separation point which eventually results in massive flow separation and lift and moment stall. Meanwhile stable separated flow on delta wing planforms allows high lift coefficients (> 1.5) at high angle of attacks (> 30^{o}) and gave birth to whole new subjects in high speed and fighter aerodynamics. On the down side, by definition, they are low aspect ratio wings which result in low L/D ratio and lift curve slope lesser than rectangular planforms. Therefore at given lift there is no respite except pitching up the wing to high angles which consequently increases the drag. Alongside, the vortical flow termed as leading-edge vortices may breakdown under certain circumstances and induce discontinuities and loss of suction.

Research on delta wings is very extensive and includes both experimental and computational investigations. The main experimental technique used to visualise vortices is by introducing a marking material into the flow, either in an air or water tunnel. The latter is preferred over the former because of advantages in capturing maximum information in low speed water stream (Reynolds number). This provides an invaluable description of flow behaviour but primarily the information is qualitative. Therefore quantitative measurements are necessary to study the detailed flow characteristics. Experimental techniques like hot-wire anemometry, pressure probes, laser Doppler velocimetry, surface pressure transducers, and particle image velocimetry are usually employed for capturing the detailed flow parameters, i.e., three dimensional velocity and pressure fields.

The majority of the published work is dedicated to slender delta wings rather than non-slender planforms. The following review will discuss the concerted efforts made in this field while the limited literature on non-slender planforms will also be presented at the end of each sub-section.

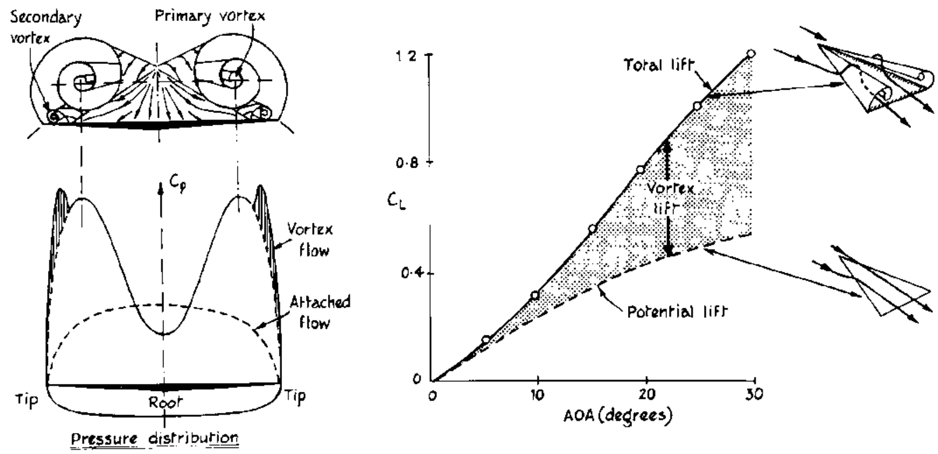

Figure 1.2-1 Flow structure over a Delta wing, Pressure distribution and Lift curve [1]

2.1 Vortex Characteristics

Before describing the aerodynamic characteristics of delta wings, a thorough description is provided on the structure of vortical flows. It has been observed for slender wings that boundary layer separation is often fixed at the apex by the sharp leading-edge which results in the formation of 3-D shear layers [4]. These shear layers ultimately roll up to form stable coherent pair of leading-edge vortices which when viewed in the lateral plane are near axisymmetric and are regions of high vorticity concentration [5]. These vortices inherit various forms of instabilities [6] as a consequence of their developing mechanism which then induce unsteadiness and nurtures vortical substructures which progress along the primary vortex.

The detailed flow structure of primary vortex, or leading-edge vortex, can be divided into three different regions [7]: a) the shear layer, formed by flow separation at the leading-edge which subsequently rolls up to form the vortex structure and feeds vorticity, b) rotational core, whose diameter is about 30% of the local semi-span and circumferential velocities are

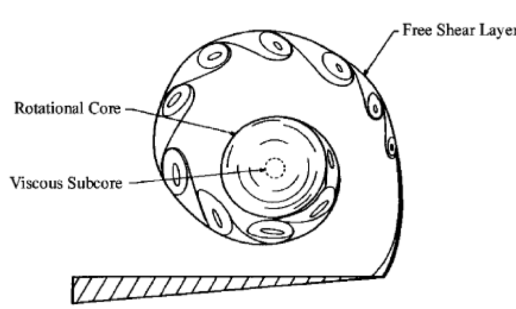

Figure 2.1-1 Three regions in Leading-edge Vortex [3]

isolated from the effect of the vortex sheet, c) viscous sub-core, extended to about 5% of the local semi-span, Here the gradients of flow parameters, i.e., pressure and velocities are very high and in the case of slender wings the tangential and axial velocity can reach 2-3 times the free stream velocity [8, 9].

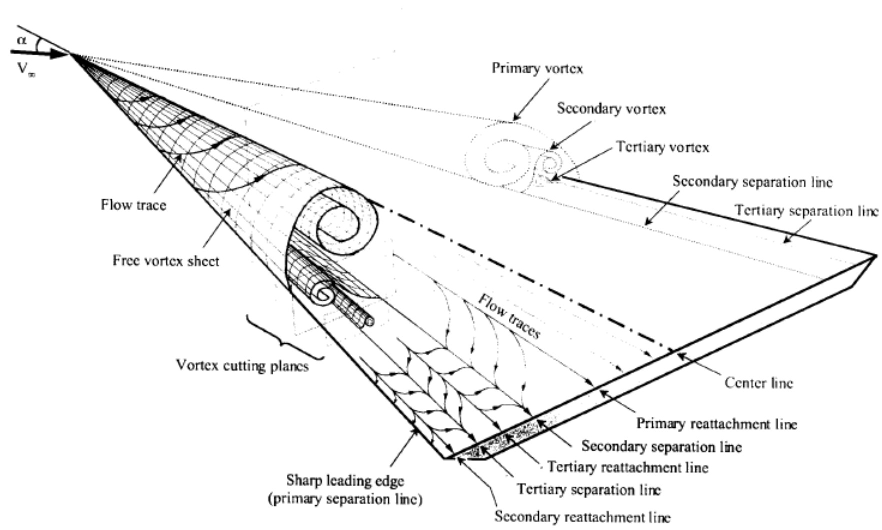

Figure 2.1-2 Detail flow structure over a sharp-edged Delta wing at high incidence [2]

With respect to the vortex formation, the rolling up of the shear layer touched the wing surface which creates an attachment line. This attachment can be traced along the chord in the streamwise direction and is similar to flow reattachment in the laminar separation bubble. The location and extent of this reattachment is a flow dependent phenomenon and varies with angle of attack. As a consequence an attached flow is created just beneath the primary vortex and shear layer is then redirected towards the low pressure region near the leading-edge area. This spanwise progression of the attached shear layer is then hindered by an adverse pressure gradient near the leading-edge and thereby caused the secondary flow separation. Eventually the adverse gradient rolls up this separated shear layer in an opposite sense of the primary vortex to form the secondary vortex. Moreover the jet-like axial convection of high radial gradients aggravated the interaction among the vortical and boundary layer flow which supplemented the formation of the secondary vortex. This region of opposite sign vorticity spurs the relocation of the primary vortex towards the centerline and away from the wing surface [10]. Interestingly, the near surface formation of the secondary vortex makes it sensitive to Reynolds number. In the turbulent regime, the vigorous momentum exchange increases the ability of flow to withstand the adverse pressure gradient and therefore prolongs the primary attachment which results in a smaller secondary vortex compared to the laminar regime. The velocity field across these vortices is also of interest and will be discussed in coming sections.

Unlike the slender delta wings, the vortical flow over a non-slender delta wing is not widely studied. The global flow structure is somewhat similar, i.e. the existence of primary and secondary vortices, shear layer instabilities, vortical sub-structures, etc., but despite these similarities, non-slender delta wings possesses some distinctive features. An overview of the existing knowledge on basic flow structure is presented here.

Taylor et al. [11] conducted an experimental investigation into the vortex structure over a low sweep delta wing. Water tunnel flow visualization and Digital Particle Image Velocimetry (DPIV) were used for qualitative and quantitative flow analyses on a 50^o delta wing for a range of low Reynolds numbers from 4300 – 34700. They showed from surface oil flow visualisation that coherent vortical structures existed even at very low angle of attack, 2.5^o, with visible traces of primary and secondary separation along the span. Furthermore, it was found that viscosity has profound effects on the trajectory of the vortex and a noticeable aggravation in vortex breakdown was also witnessed for increasing Reynolds number. A similar investigation by Ol and Gharib [12] stated that qualitative features of the flow, such as location of primary vortex, do not change significantly with Reynolds number. In contrast, an obvious shift in vortex location was observed by Taylor et al. [11] with variation in Reynolds number.

Like the slender wing, the structure of vortical flow over a non-slender delta wing is composed of many flow phenomena and is dependent on many parameters. One of the distinctive features of low sweep delta wing is the dual vortex structures which are multiple peaks of same sign vorticity [13, 14]. The first observance was made in a computational result [13-15] that a shift from single to multiple vorticity concentration occurred over a non-slender wing at moderate Reynolds numbers. The corresponding vorticity peak is embedded in the shear layer due to near-wall interactions. This has been confirmed by the aforementioned [11] DPIV investigation that multiple peaks do occur and are highly sensitive to experimental setup and flow condition. This type of behaviour is quite predictable since the low proximity of leading-edge vortex to the wing surface [16] intensifies the boundary layer and vortex flow interaction [11, 17]. This dual vortex structure cannot be formed at very low Reynolds number (< 10000) where viscous effects dominates and for larger Reynolds numbers they can only exist up to 10^o [18] because the outboard vortex suffers ealry breakdown. With increasing incidence the primary vortex moves away from the wing surface and hence the flow started mimicking the vortical flow over a slender wing, a single vortex of high vorticity concentration.

Reviewing the experiments on vortical flow characteristics, it is evident that researchers prefer to publish selected cases, either different x/c at a specific incidence [5] or different incidences at a specific x/c [19]. This usually refers to a location well upstream of breakdown, in the case of mechanical probes to mitigate the probe induced breakdown [9], and at an incidence where vortical flow is fully developed with high axial and radial gradients.

Like the tip vortices of rectangular wings, leading-edge vortices are usually characterized by axial and swirl velocities, vorticity, and circulation which are in turn useful for detailing core parameters and prescribing correlations among different physical and mathematical parameters. The following subsections present an overview on flow characteristics associated with vortical flow.

2.1.1 Velocity

Axial velocity along the vortex core plays a central role in the characterization of the leading-edge vortex up to the extent that vortex is considered to be in pre-breakdown state if its core velocity is higher than the free stream velocity. Whereas the conical profile across the vortex is imperative in describing the flow behaviour over the wing and regarded as a comparison tool among different cases. Both intrusive [5, 9, 20-22] and non-intrusive methods [11, 12, 19] are employed for capturing the velocity field.

Historical work in predicting the flow parameters has been done by Hall [23]. He proposed a theoretical model to estimate the axial velocity along the vortex core. The model was based on assumptions that the flow is continuous and rotational and the viscous diffusion is confined to a relatively slender subcore. The calculated pressure field within the core was in qualitative agreement with experimental data. The velocity profiles across the core are informative in determining the evolution along the span and post and pre breakdown behaviour. The core location was based on maximum velocity for cross-wire data [5] and corresponds to minimum pressure coefficient for seven-hole probe data [22]. Leading-edge vortices usually exhibits a strong jet-like flow with values as high as 3.5 times the free stream velocity [6]. This strong axial convection is a consequence of the radial equilibrium (cyclostrophic balance; when the centrifugal forces are balanced by the pressure forces) required for the conservation of momentum augmented by the vortex sheet spiralling around the vortex axis [24]. Due to the downstream progression of the flow these vortex lines are inclined to the vortex axis and hence have a streamwise component supplementing the axial flow. Moreover with downstream distance, the vortex increases in strength through continuous feeding of vorticity by free shear layer separated from the leading-edge. The resulting chordwise increase in swirl velocity induces a favourable pressure gradient along the vortex axis.

Visser and Nelson [5] used a cross wire probe to acquire the velocity distributions for delta 75° at an incidence of 20^{o}. The horizontal spread of axial velocity is a good Gaussian fit but only prior to the breakdown reaching the trailing-edge. Moreover along the span at different chordwise stations the velocity profiles exhibited a self-similar behaviour. The other noticeable feature is the relative size of jet core is larger than the swirl velocity peak-to-peak distance. As the angle of attack increases to 27^{o} the jet core diffuses to an extent of 50% of local semi-span, while on the other hand, swirl core spreads to 5-10% of local semi-span [3]. The swirl line plots across the core showed high radial gradient and can be viewed as a tight confinement of vorticity within the vortex core [5]. On the other hand high frequency time resolved measurements reveal the unsteadiness of vortical flow even at locations well upstream of breakdown where it was accompanied by large amplitude velocity fluctuations [25]. The maximum rms circumferential/tangential velocity often exceeds the free stream velocity depending on the angle of attack and reaches its peak at time averaged vortex axis. These large fluctuations are a consequence of vortex meandering [25] rather than the instabilities associated with the separated shear layer [26]. Devenport et al [27] suggested that this phenomenon of vortex meandering/wandering has a connection with free stream turbulence and found its origin in tunnel unsteadiness. This topic has been extensively studied under the umbrella of trailing vortices to reduce the undesirable data corruption induced by high frequency core oscillations. In the case of slender delta wings this vortex core random displacement is also explained by an existence of non-linear interactions between secondary and primary vortex.

Recent interest in UAVs and MAVs anticipated studies at low Reynolds flow to understand the vortex structure. A version of Stereoscopic Digital Particle Image Velocimetry (SDPIV) was used to investigate the velocity field of 65° and 50° sweep delta wings with 30° bevelling on the windward side [12]. Flow visualization was also conducted to complement the velocity field data. The camera spot is the near apex region for the range of comparably low angles of attack 5°-20° at a Reynolds number of 6000-15000. The flow over slender wings is expectedly conical with a nearly a linear increase in peak axial velocity with angle of attack, while for non-slender wing different case studies revealed that conical behaviour is only limited to near apex region. The velocity profiles upstream of $x/c = 0.3$ for 12.5° and 15° angles of attacks highlighted the slender-like conical development of flow. Ol and Gharib concluded that beyond 10° the flow over a 50° sweep wing deviated from the behaviour of a 65° sweep wing due to peculiar upstream progression of breakdown at low incidences and intensified interaction between the vortical and boundary layer flow as discussed previously. It is understood that a complete understanding of the flow structure cannot be developed without the knowledge of axial and swirl velocities. In the case of non-slender delta wings, the line plots across the vortex center showed that, at low angle of attacks, axial velocity never exceeds free stream velocity even at points well upstream of any observable breakdown [28]. On the contrary, over a 45° delta wing at an incidence of 15°, Honkan and Andreopoulos [21] reported a maximum axial velocity of 1.3 times the free stream velocity.

2.1.2 Vorticity

Numerous investigators hypothesized theories for vortex stability and breakdown which are based on vorticity distribution and circulation confined within the primary vortex. To date, distinct techniques have been used to study the effect of vorticity on vortex structure which includes references [3, 5, 8, 20, 29]. A brief insight is presented here to establish a basis for future comparison. The distribution of vorticity across the vortex is of prime interest along with the core value and radial derivatives. It is also vital in determination of vortex strength because the maximum vortex strength, given by maximum swirl ratio[1], is strongly dependent on local free stream pressure gradient and therefore restraining the ability of flow to move downstream. This can also be interpreted that "the maximum amount of vorticity or circulation at a given station is limited by the ability of flow to move downstream, which in turn is regulated by pressure gradient" [3]. Moreover the definition of vorticity is equally important for an existence of stable vortices. In regard to this a theory has been presented which considered a balance between streamwise convection of vorticity and the vorticity generation from the boundary layer, imperious for an existence of stable leading-edge vortex. Conversely, the vortex breakdown can also be seen as a disturbance of vorticity balance due to a reduction in axial convection of vorticity [30]. The ratio between the circumferential and axial velocity or swirl angle, is an indication of this balance. The preceding discussion underlines the significance of vorticity in detailing the flow structure and acts as a definitive tool to locate or predict vortex breakdown.

A reflective work on vorticity and circulation on 75° sweep delta wing has been done by Nelson and Visser [5, 8]. There was a substantial difference in the value of axial vorticity even for identical geometries and flow conditions, for which a close analysis revealed the sensitivity of vorticity field on the grid spacing. The highest derived value was reported for the finest grid resolution and vice versa. Furthermore the investigators often used chord and free stream velocity to non-dimensionalize the vorticity, while the study indicated that the scaling of radial circulation distribution and vorticity field by local semi-span resulted in similar distributions in the chordwise direction for pre breakdown flow. They also studied the spatial progression of both negative and positive vorticity by central differencing the velocity field. In order to inspect the effect of local geometry, the vorticity field is non-dimensionalized by local semi-span. The data presented for the slender delta wing at an incidence of 20°revealed the concentration of vorticity in the region immediately around the core of the primary vortex. While a small weak region of opposite sign vorticity is observed near the wing surface, this secondary vortex is usually associated with large velocity and vorticity deficit [21]. Despite the change in geometry and angle of attack, the distribution of vorticity across this secondary vortex showed similar behaviour but it is sensitive to Reynolds number due to its presence in the boundary layer. As discussed in the velocity subsection, distinct criteria exist for the definition of core location. In the case of vorticity, likewise, core location can be determined based on peak of axial vorticity or by locating the peak in axial velocity. Essentially, in theory the core does not necessarily mean the viscous portion of the LEV but a relatively small cylindrical region.

To further scrutinize the vorticity field, Visser and Nelson [5] integrated the respective signs of vorticity over the area of their influence. This reported an increase in magnitude of term linked with primary vortex (positive vorticity) with increasing distance from apex, no change in magnitude is observed for the term associated with secondary vortex (negative

[1] Swirl ratio $v_{\theta max}/U_\infty$

vorticity). This reflected the consistent increase in strength and spread of primary vortex as compared to secondary vortex. The profiles for the no breakdown case (Λ=75°and α=25°) representing the local vorticity density distribution showed the conical behaviour of the flow with comparative peak values for all the profiles along the chordwise direction.

Mitchell and Molton [6] published the vorticity contours around the breakdown location for a 70^{o} delta at an incidence of 27^{o} for Reynolds number of 1.56 million, given in Figure 2.1-3. Prior to the breakdown (x/c=0.64, VBD x/c=0.65) the vorticity contours are organized with concentration in the center and a peak non-dimensional value of > 200 is observed, which subsequently drops to 140-150 after breakdown (x/c=0.74) and lastly a peak of 80 is calculated at a distance of 0.21c downstream of breakdown. Regardless of data acquisition method, intrusive or non-intrusive, an attention must be given to numerical values of vorticity. As discussed above, the vorticity field is sensitive to grid resolution and in the case of non-intrusive methods; correlation-finding algorithms can easily skew the images. In effect, the induction of numerical noise and windowing resolution in a region of high velocity gradients results in an accumulation of errors which eventually magnifies the inherent uncertainty. They further deduced that the dissipation of vorticity in the breakdown process has no implication on the aforementioned stationary substructures and pointed towards the existence of convective instabilities near the leading-edge. The data was collected for 11 different chordwise stations within a length of 0.3c and vorticity field is presented for each location. The absence of velocity information hinders user to make any correlation among the vortex parameters within the vicinity of breakdown whereas the behaviour has been explained. The benefit of LDV measurements made by Mitchell and Molton [6] in detecting the reverse flow revealed that the abrupt deceleration of core flow to a stagnation point is followed by a zone of recirculation with a considerable increase in vortex size. The expected presence of a wake-like core is witnessed in post breakdown region.

The time accurate measurements have their advantage in defining the instantaneous vorticity or velocity fields. Through this effort, one can avoid the temporal averaging of intermittently appearing vortical structures. It can be deduced from velocity vector plots that the primary vortex must be a region of strong axial vorticity. On the contrary no

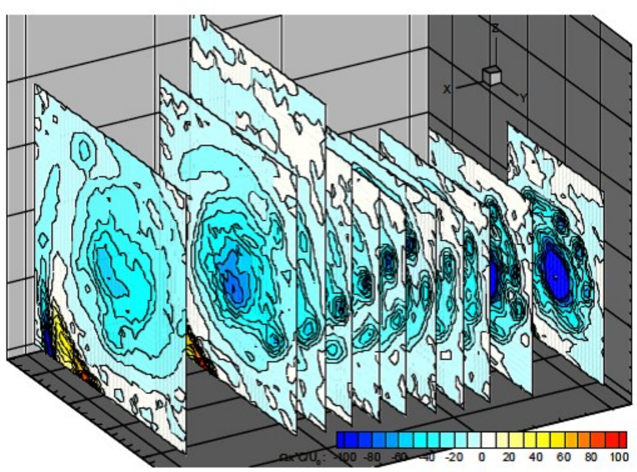

Figure 2.1-3 Streamwise evolution of vorticity for DW70 at α = 27^{o} [7]

information can be extracted from velocity plots for the spread of small vorticity concentrations around the periphery of the main vortex. For non-slender delta wings, the relative size of the main vortex and peak values of vorticity are inferior to those of a slender delta wing main vortex. Additionally it has been shown for non-slender delta wings that at low angle of attacks the core axial velocities are not always jet-like even at locations well upstream of breakdown [28]. Therefore a cautious approach is required for a thorough understanding of the non-slender vortical flow field. Unlike the extensive work already done on slender delta wing vortices, very few studies have focused on the vorticity fields of non-slender delta wings.

Considering the peculiar nature of flow over a non-slender delta wing, instantaneous information is often conducive to capturing the finer details. Ol and Gharib [12] opted to use the SDPIV data and presented the contours of instantaneous vorticity in the vicinity of expected breakdown for a 50° sweep delta wing at low Reynolds number. As the angle of attack was increased from 10° to 20°, a visible dissipation of vorticity was observed in the primary vortex followed by an entirely diffused vortex at 20 degree with no distinct vorticity peak. Furthermore, the results complemented the theory postulated on the balance of vorticity production and convection by showing both signs of vortical substructures in the post breakdown region. This implied that no downstream sinking of vorticity is required to respect the balance owing to the presence of counter rotating structures.

As discussed above, distinct definitions have been adopted to locate the vortex core [5, 7, 12, 21] whereas in the case of non-slender delta wings the wake-like patches and dispersion of vorticity in skewed vortices often makes it difficult to follow those approaches. Especially the spanwise spread of the vorticity creates ambiguity in determining the core region. Therefore another method is employed by drawing the streamlines in planar velocity information which eventually winds around the vortex center [12].

2.1.3 Circulation

Circulation confined by the primary vortex is imperious for vortex strength correlation and in calculation of aerodynamic loads, especially the lift. The spanwise distribution is typically plotted against the non-dimensional radial distance whose origin is at the vortex center. Different schemes of scaling of circulation have been employed in order to establish some sort of correlation among different parameters, i.e. local semi-span, chord, vortex radius, and sine of angle of attack [5]. Circulation is calculated either by computing the line integral of tangential velocity along a closed contour centered about the designated vortex core or by integrating the vorticity over the area under investigation, also known as Stoke's theorem, therefore it can also be seen as vorticity flux.

Likewise the deterioration was witnessed in other vortex characteristics; on breakdown coherent vortices also lose the confined circulation. In the case of slender delta wings in the no breakdown case the circulation is observed to increase with decreasing rate from vortex origin towards the leading-edge. It was further deduced that the widening of viscous core happens over the slender delta wing because at a given location the characteristic radius[1] of the leading-edge vortices increase with increasing angle of attack [12]. Nelson and Visser [8] computed spanwise circulation and reported two peaks in distribution. The secondary peak was attributed to the inclusion of shear layer vorticity. Conversely, chordwise calculations elucidated the dependence of circulation on distance from apex where at a given angle of attack the circulation increases with increasing local semi-span [5, 8, 12]. This strengthening of the vortex in the chordwise direction and self-similar behaviour shown by circulation, tangential velocity and axial vorticity when scaled by local semi-span about the vortex center complements the conical nature and growth of the vortical field over a delta wing.

In addition for the 75° wing the chordwise variation at a given angle of attack resulted in a scatter distribution but despite the fact, the data corresponding to the maximum radius of integration r/s[2] = 0.6 indicated a linear variation beyond the mid-chord. Nelson and Visser [8] related the scatter to probe interference at the lower boundary of integration paths where r/s distances are comparable or greater than z/s location of the vortex axis. Furthermore the proximity of probe to the wing may result in a jet flow beneath the probe and other interferences may corrupt the flow information and thus the derived quantities. Johari and Durgin [31] employed an ultrasonic technique to compute the circulation for a 60° and a 70° wing at a Reynolds number of 190,000. They found that circulation was measured to grow non-linearly in the chordwise direction for which the breakdown occurs aft of the trailing-edge. Conversely, an approximately linear growth is witnessed until the breakdown reached the vicinity of wing apex.

Circulation in the case of non-slender delta wing is not widely studied. The main reason, as discussed, is the strong interaction between the vortical and boundary layer flow corrupts the flow information and hence the derived quantities, i.e. circulation. This in turn limits the penetration of mechanical probes and hence makes it difficult to capture the three dimensional velocity or pressure field. Therefore non-intrusive methods [12, 32] are adopted to acquire the velocity information and to derive the circulation confined within the vortex.

It was observed that at low angle of attacks the circulation distribution plotted against vortex radius shows similar behaviour like in the case of slender wings [12]. The said experiment covered a range of low to moderate angle of attacks, where an increase in angle of attack resulted in diverging behaviour. Generally for low sweep wings the spanwise diffusion of vorticity implies that the peak circulation values are typically attained at a radius comparable to the distance between the vortex center and separated shear layer. They

---

[1] radius at which peak circulation achieves
[2] ratio of radius to local semi span

further mentioned that more accurate predictions can be made by taking the integral over an elliptical path with major axis in the spanwise direction because the leading-edge vortices are skewed and in close proximity of the wing surface. In the post breakdown region it was found that a drop in circulation is witnessed for both slender and non-slender delta wings. However this should be regarded as a local diffusion because the total circulation keeps on increasing even after the breakdown due to the continuous addition of vorticity from the leading-edge.

To summarize, a number of studies have shown that the non-dimensional leading-edge vortex characteristics, i.e. axial and swirl velocities, axial vorticity, core radius, and circulation, remain almost constant prior to the breakdown and in region isolated from apex or trailing-edge disturbances. It must be mentioned that in distinct studies, maximum axial velocity for a 75° delta wing at an incidence of 20° was reported at about $x/c \approx 0.6$, well upstream of breakdown [8, 33]. Meanwhile, as discussed, no direct comparison can be made in the vorticity numerical values, especially the peak value, given the sensitivity associated with the derivative field.

2.2 Vortex Breakdown

The strength of the primary vortex increases with increase in angle of attack until a sudden disorganization terminates this progression. The post breakdown flow can be characterized by massive dilatation of vortex structure, a profound alteration of velocity field along with large scale fluctuations [34]. In this process the primary vortex loses its coherence and rapid exchange of momentum results in large scale turbulence [35]. Moreover the detrimental phenomenon of vortex breakdown is typically characterized by an increase in vortex diameter whereas the non-linear vortex lift is a strong function of vortex size and strength. This intriguing aspect of the vortex breakdown along with its practical implication makes it an active field of research. Vortex breakdown is an outcome of cascade of events which are still unanswerable and different theories were formulated.

The onset of vortex breakdown plays an important role in limiting the high lift, high angle of attack performance of delta wing. Since the observance of LEVs, a substantial amount of research effort has been devoted to thoroughly study the phenomena and mechanisms responsible for the deleterious effect of vortex breakdown on lift generation. Literature survey reveals that the vortex bursting is not solely responsible for the lift deterioration but also incites the detrimental aero elastic effects. In addition, high frequency fluctuations the breakdown location results in asymmetry flow over a wing and may induce undesirable roll moments. The unsteadiness associated with breakdown is well documented and even involves an out of phase oscillation of breakdown points along the vortex axis which results in periodic roll motion, or wing rock [3, 34]. This self-induced oscillation adversely affects the manoeuvring envelope of combat fighter jets and approach angle of attacks of high speed commercial aircrafts.

On the contrary, vortex breakdown can be beneficial under certain circumstances. Firstly, the generation of turbulence in breakdown process expedites the dissipation of rotational kinetic energy which in turn mitigates the adverse effect of trailing vortices. Hence they can play an instrumental role in controlling the wake hazards [36]. Also, on fuel injection, the air-fuel mixing in combustion chamber can be enhanced through breakdown of swirling jet. The importance of vortex breakdown made it an active topic of discussion for the last 50 years. Therefore extensive research efforts have been devoted to understand the physical mechanisms of the flow responsible for vortex breakdown. In view of that an overview is presented here encompassing the types, theories and parameters involved in extent of this subject.

2.2.1 Occurrence & Type

The LEVs are susceptible to break down and hence the tight flow structure cannot be maintained indefinitely. It has been established that vortex breakdown occurs under an influence of adverse pressure gradient. In the case of delta wings an increase in sweep angle decreases the adverse pressure gradient. The effect of slenderness is similar to the aspect ratio of a conventional wing; however the trailing-edge is the source of adverse pressure gradient for the subject under investigation. Therefore upstream propagation of unfavourable effects can be lessened by increasing the sweep angle. As a result, flow deceleration occurs; this subsequently forms a stagnation point along the vortex axis. According to Delery [34] this process is highly dependent on swirl ratio and breakdown occurs when swirl ratio reaches a critical value. The circumstances of breakdown are practically insensitive to Reynolds number and the local turbulent properties but these factors have profound influence on vortex evolution.

Generally, there are two categories of vortex burst; bubble and spiral type, while in reality, as mentioned by Nelson and Pelletier [3], they may represent an extreme in a continuum of breakdown forms. For the former, the dominant feature is sudden axisymmetric expansion of vortex core from about 5% of local semi-span [3] to many times the original size and rapid transition of core axial velocity from jet-like to wake-like within a few core diameters. The tight coherent structure results in a non-coherent, turbulent like wake which entrains turbulent components from free-stream but also sustains, the prior to breakdown stable vortical substructures [6]. From qualitative flow visualization one may observe a

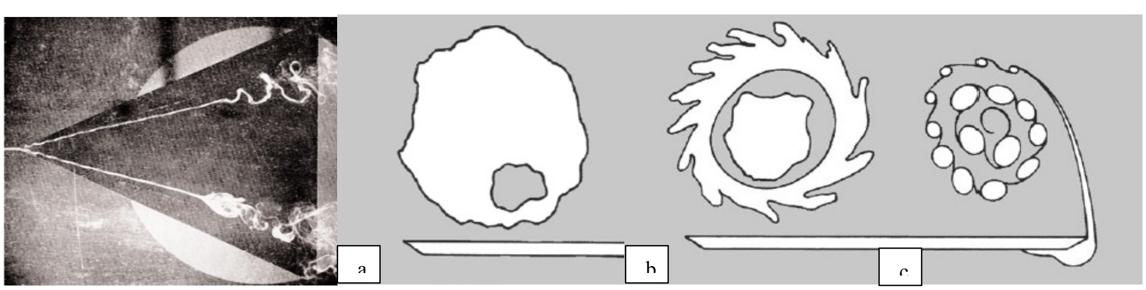

Figure 2.2-1 Vortex breakdown (left) Flow visualization showing both type of breakdown on delta wing (right) schematic of VBD [11], (a) Spiral Type, (b) Bubble Type,(c) Shear Layer [1]

free-stagnation point along the vortex centerline. While in spiral type breakdown, the vortex centerline appears to corkscrew downstream in the same rotational sense as the LEV whereas the ultimate result is same as for the bubble type breakdown.

2.2.2 Dependence

The location and propagation of vortex breakdown can be tempered by various parameters, i.e. angle of attack, wing geometry and Reynolds number. It has been understood that the upstream progression of breakdown is a strong function of angle of attack [37] because the adverse pressure gradient increases along the vortex core with increasing incidence. While on the other hand, increase in sweep angle delays the vortex breakdown [3], courtesy of the fact that increasing sweep strengthens the vortex and hence prolongs its presence against the adverse pressure gradient.

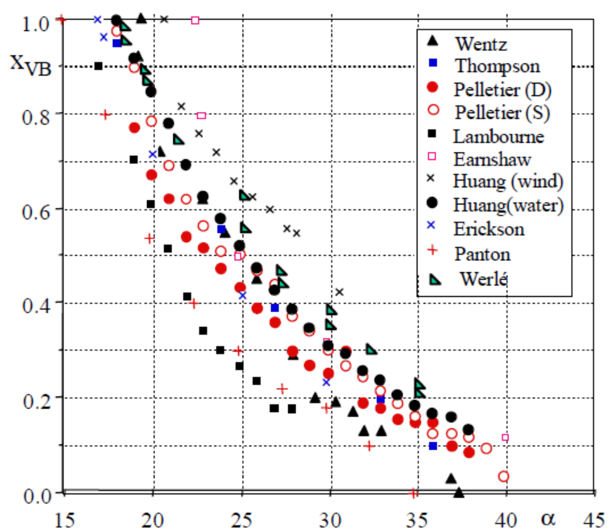

Figure 2.2-2 Vortex breakdown over a slender delta wing

There are many factors which influence the vortex breakdown in relation to wing geometry. Firstly, leading and trailing-edge bevelling, it was found that bevelling delays the vortex breakdown at the given angle of attack [38]. This can also be looked as the leading-edge bluntness, which was widely studied. Moreover the upstream progression of the vortex breakdown is delayed for the round edge leading-edge compared to sharp edge wing [39]. In addition this observation is further supported by the fact that onset of breakdown reaching the trailing-edge is delayed for the rounded edge case. Luckring [40] conducted surface pressure measurements on a 65° delta wing and revealed that unlike the sharp leading-edge, where separation is fixed at apex, blunt edge delayed the shear layer separation to about 30% of the chord. Conversely, it has been proved that the leading-edge radius reduces the size and strength of the vortex [41, 42]. Similar studies have been conducted for non-slender delta wings considering the effect of leading-edge radius. It was observed for large leading-edge radius that the outward bending of the secondary separation line was delayed which is an indicative of delayed vortex core breakdown [41]. Another geometric factor which influences the vortex breakdown is t/c[1] ratio. Observations have been made that wings with higher t/c ratio tends to stall earlier than the thinner wings [43].

It is well known that the flow over slender delta wings is insensitive to Reynolds number as long as the wing leading-edge remains sharp, so does the vortex breakdown. Figure 2.2-2

[1] Thickness to Chord ratio

shows the substantial scatter in vortex breakdown locations over a same sweep delta wing but under different tunnel and flow conditions. Being optimistic, at least the behaviour or trend can be predicted owing to the given flow conditions and geometric parameters. These discrepancies may be attributed to wind tunnel factors, i.e. wall effects and buoyancy, or different flow visualization techniques, support interference, model deformation (built-in yaw and roll), and the unsteady nature of breakdown location [43]. Among these, considerable research effort has been devoted to investigate the wind tunnel wall and blockage effects. The latter presumably induces an effective positive camber which delays the breakdown [44]. A data collection presented by Jobe [38] on 65 degree delta wing tells the sensitivity of breakdown locations to different parameters. It was evident that t/c ratio, visualization technique and flow medium have profound effect on vortex breakdown location. The unsteady nature of vortex characteristics was validated by Gursul [45]. The data has been acquired for a range of sweep angles (60^o-80^o) for Reynolds number of 25000 – 100,000. The acquired data showed large amplitude velocity fluctuations, along with variations in breakdown locations. A fluctuation of about 10% of chord length was reported in the case of slender delta wings.

Lowson and Riley [43] examined the reasons for this variation in vortex breakdown location from different investigations on delta wings of equivalent sweep, by reproducing the similar model and flow condition. It was evident from the recorded data that vortex breakdown is promoted in water tunnel compared to wind tunnel experiments. They inferred that support interference, wind tunnel factors, differing flow visualization methods and Reynold number effects have some influence on vortex breakdown location whereas effects due to geometry variation far outweighs the interference induced by aforementioned factors. Therefore, neither there is an agreed location of vortex breakdown nor any evitable dependence on wing sweep or angle of attack.

2.2.3 Location

Vortex breakdown location information along the wing is important for a complete dissection of the said phenomenon. The most common method to record breakdown locations is via flow visualization, where the information is more qualitative then quantitative. Therefore it was often used in tandem with some instrumentation for two or three dimensional velocity acquisition.

As already stated, many different parameters and mechanisms are responsible for vortex instability which leads to massive diffusion. Therefore drastic changes in flow structure were witnessed in post breakdown region. Among them it was observed that maximum axial velocity is vital in determination of vortex breakdown location. One of the validations is based on a abrupt drop in predominantly jet-like axial core to a wake-like core. In other circumstances, depending on the type of breakdown, the flow can even reverse its direction along the designated vortex core axis [22]. Whereas differentiating the lateral velocity field reveals that a sudden diffusion in vorticity is a parallel phenomenon which characterizes the vortex breakdown. However, in the case of slender delta wings, the prominent existence of secondary vortex of opposite vorticity could play a role in the prediction of vortex breakdown. The secondary vortex outboard of the primary vortex is often characterized by a wake-like axial flow where on increasing angle of attack, pockets of reverse flow start appearing [12, 28]. This implies that breakdown of secondary vortex precedes the main vortex and can be used as a predictive criterion for onset of primary vortex breakdown.

As discussed, axial deceleration is a sign of vortex breakdown over a slender delta wing which even results in patches of reverse flow. On the contrary, vortices over non-slender wings are away from the symmetry line and closer to the wing surface. This results in less interaction among the pair of vortices and intensified interaction among the vortical and boundary flow often resulted in a wake-like core. This completely alters the breakdown mechanism over a non-slender planform.

As stated earlier, vortex breakdown information is of profound interest because of its detrimental effect on the lift producing capability of delta wings. The literature on vortex breakdown for a low sweep delta wing is limited as there are many parameters involved and each of them has a degree or level of influence on vortical fluid mechanics. Recall that the low proximity of leading-edge vortex anticipated the interaction between the secondary separation of the boundary layer and separated shear layer which resulted in vortices susceptible to flow and model support condition. As a consequence, limited information is available on breakdown of non-slender delta wing vortices and all the published efforts are qualitative information extracted from the flow visualization [46] and are often limited to the near apex regions [37]. Early work in the field [24] disregarded the low sweep delta wings for vortex breakdown study reporting that vortex core is highly unsteady. Later on observations made in the near apex region of 50 degree delta revealed that vortex breakdown already reached 15% of the chord at an incidence of 16° [37] while in the case of slender 65° wing it is beyond the trailing-edge [43]. However, at low Reynolds number large fluctuations of breakdown location of the order of 50% of the chord was observed [11] compared to 10% for more slender planforms. This suggested that flow over non-slender wings is significantly unsteady with a number of parameters interacting, resulting in complex flow phenomena. Pelletier and Nelson [46] provided the only full span progression of the breakdown over a 50° delta wing where, measuring from apex, breakdown already traversed the 80% of the chord at an angle of attack as low as 8 degree and reached the apex at around 20°.

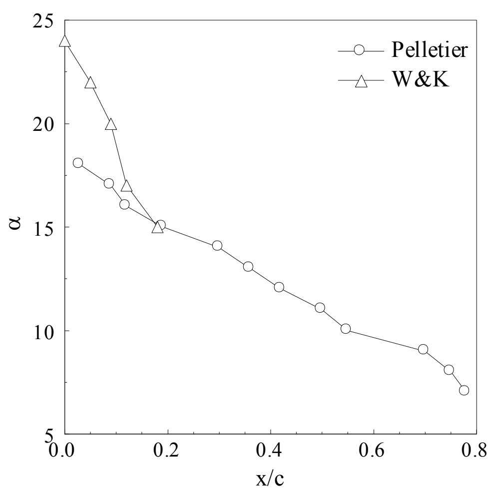

Figure 2.2-3 Vortex breakdown over DW50 from [51]

Despite the extensive research effort dedicated to the understanding of vortex breakdown, information on various aspects is still fragmentary especially the inert unsteadiness of the process is not yet entirely elucidated. It has been established that future research efforts shall question unsteady phenomenon related to breakdown [34]. Firstly, the effect of disturbances, geometry or flow, how they propagate and amplify instability which eventually leads to breakdown under certain circumstances. Secondly, the generation of turbulence and related modelling to assist computational analyses and lastly the fluctuations related to breakdown location and in particular the large out of phase oscillations of respective breakdown points.

2.3 Aerodynamic Characteristics

Research into aerodynamic characteristics of delta wings is quite extensive. This includes experimental, theoretical and numerical investigations. In last 30 years the most prominent contributions were made by NASA, encompassing basic planform studies to complex parametric studies. The motivation behind delta wing is stable high lift condition where the lift enhancement and stall delay are solely due to additional velocities induced on the suction side by the strong leading-edge vortices. Unlike the classical potential lift, vortex lift is a non-linear phenomenon and often accompanied by high frequency of unsteadiness. After the vortex breakdown this non-linear vortex lift diminishes and leads to the wing stall conditions. Soltani and Bragg [47] inferred that nonlinear vortex lift and the movement of the burst point on the wing, due to the flow unsteadiness [48], are related to changes in measured lift-curve slope. Likewise, increasing the sweep angle decreases the lift curve slope because for the given angle of attack the circulation decreases with increasing sweep angle [3].

2.3.1 Lift Prediction

2.3.1.1 Direct measurement

Direct force balance methods are always of profound importance in determination of aerodynamic characteristics. Figure 2.3-1 presented the lift curve for various delta wings of different sweep angles. It was observable at low angle of attack that regardless of sweep angle the lift curves are linear whereas on increasing the angle of attack, the contribution of the non-linear vortex-lift increases and so do the non-linearity in the lift curve. These recordings were made by Wentz & Kohlman [37] using a strain gauge force balance at Reynolds number 1,000,000.

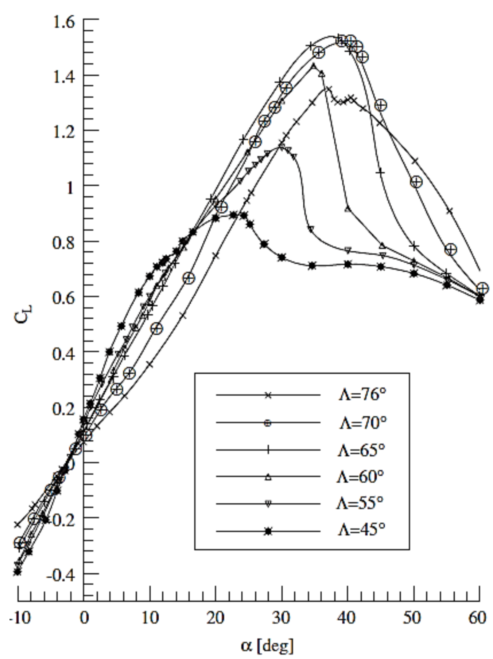

Figure 2.3-1 Lift characteristics of delta wings of various sweep angles

They also reported the vortex breakdown by virtue of flow visualization and correlated the lift, drag and moment information. It has been observed that the presence of breakdown on the wing prompted a reduction in lift curve slope but the lift continued to increase until the maximum lift coefficient is achieved and the wing stalls. It is to be noted that this phenomenon is limited to wings with low and moderate sweep angle ($\Lambda < 70^o$). In addition they also studied the effect of aspect ratio on aerodynamic loads and found out that at given angle of attack the strength of leading-edge vortices increases with decreasing sweep angle. Consequently, higher normal force coefficient is witnessed for the higher aspect ratio delta wings.

A number of difficulties are associated with the investigation of non-slender delta wing and hence deters the progress made in this regard. The resultant aerodynamic loads, non-slender wings have lower C_{Lmax} and lower stall angle compared to their slender counterparts whereas the slope of the lift curve increases with decreasing sweep angle considering that for a given angle of attack, circulation at specific location increases with decreasing sweep angle [3]. Figure 2.3-1 shows the lift behaviour of delta wings for various sweep angles, highlighting the increasing slope and decreasing maximum lift coefficient.

2.3.1.2 Indirect measurements

Many studies have been carried forward to accurately estimate the lift from flow field information, but the established knowledge is centred on derived quantities. Hence for every additional step the accumulation of uncertainty ends up with an approximate numerical value. Quantitative wake surveys have profound importance in understanding drag mechanisms, since they isolate drags from different physical origins, i.e. profile, induced and wave drag. Alongside, a wide recognition is the ability to solve sectional values, which found importance in lift distribution for complex high lift systems. Kusunose [49] documented the universal wake data analysis code based on the theories of Maskell and Brune [50, 51]. They determined lift by either summation of spanwise circulation or by applying control volume approach, along with planar wake assumption. The said notion does not represent the true wing span; in fact the rolling up of the vortex induces an error in tip region. In the case of delta wings, the energetic LEVs further magnify the induced error due to highly three-dimensional flow over the wing. Therefore for high aspect-ratio wings, minimal error is induced by planar wake assumption.

Recently in 2007, Kaplan et al [32] addressed the issues associated with low aspect-ratio wings. They applied the modified Kutta-Joukowsky theorem based on vortex span, also referred to as effective span, twice the distance between vortex core and wing center line. They utilized the peak circulation value calculated from near wake scan data in cross-flow planes by using DPIV. The computed lift coefficients were in compliance with lift values found in literature.

2.3.1.3 Theoretical Approximation

Before 1970, theoretical lift prediction theories are entirely based on attached flow assumption which subsequently fails for delta wing planform. Then responding to the need, Polhamus [52, 53] estimated the vortex-lift based on leading-edge suction analogy and calculated total lift by augmenting the potential and vortex lift component. The correlation he presented only applies to thin wing sections with no camber and twist. Moreover there would be no leading-edge suction or the leading-edge should be sufficiently sharp to fix the shear layer separation point. Given these assumptions, the total lift can approximated as:

$$C_L = K_P \sin\alpha \; cos^2\alpha + K_V \; sin^2\alpha \cos\alpha$$

Here K_P and K_V are constants, their numerical value depend on wing geometry. Considering the incompressible flow (M < 0.3), with increasing aspect ratio (decreasing sweep angle), a slight increase in value of K_V asymptotically levels at π. On the other hand K_P increases rapidly with wing aspect ratio because it is the lift-curve slope at zero lift. Polhamus theoretical approximations were in total agreement with experimental results only before the breakdown reaches the trailing-edge. Since the analogy is based on potential flow leading-edge suction analogy which expects flow re-attachment inboard of the vortex, therefore the deviance from experimental values was observed for higher angle of attacks. He also cautioned that the lift prediction method has tendency to over-predict the vortex lift for moderate and low sweep wings because the vortices over such wings cannot provide full suction courtesy of their orientation with respect to the trailing-edge. Therefore the Polhamus theory is in full agreement with experimental results acquired for high sweep delta wings because lesser area is required for full vortex lift.

2.3.2 Drag Prediction

Drag force acting on an aircraft can be scrutinized in distinct manner, either by studying the physical origins or by correlating the lift force. Figure 2.3-2 presents a broad-brush categorization of drag. This decomposition helps providing an insight into the wing design process where high induced drag incites the examination of lift distribution and excessive profile drag points to boundary layer separation.

Accurate drag prediction is an important factor in defining the planform aerodynamic characteristics therefore tremendous effort has been made over the decades to archive the drag values. Wentz and Kohlman [54] used a six-axis pyramidal strain balance and recorded the lift, drag and pitching moment values for a range of sweep angles. All the experiments were conducted at Reynolds number of 1 million provided that prior to the experiment the insensitiveness of breakdown is proved by varying the tunnel dynamic pressure. A higher drag value is reported for a lower sweep angle wing against given lift coefficient. It is to mention that drag values are sensitive to model holding mechanisms hence the discrepancies in values are found in literature. Al- Gharni et al [55] were among the few who reported the drag polar for a 65° delta wing. It is to note that the inception of delta wing is for optimizing high lift conditions at high angle of attack therefore limited literature is available on drag coefficient.

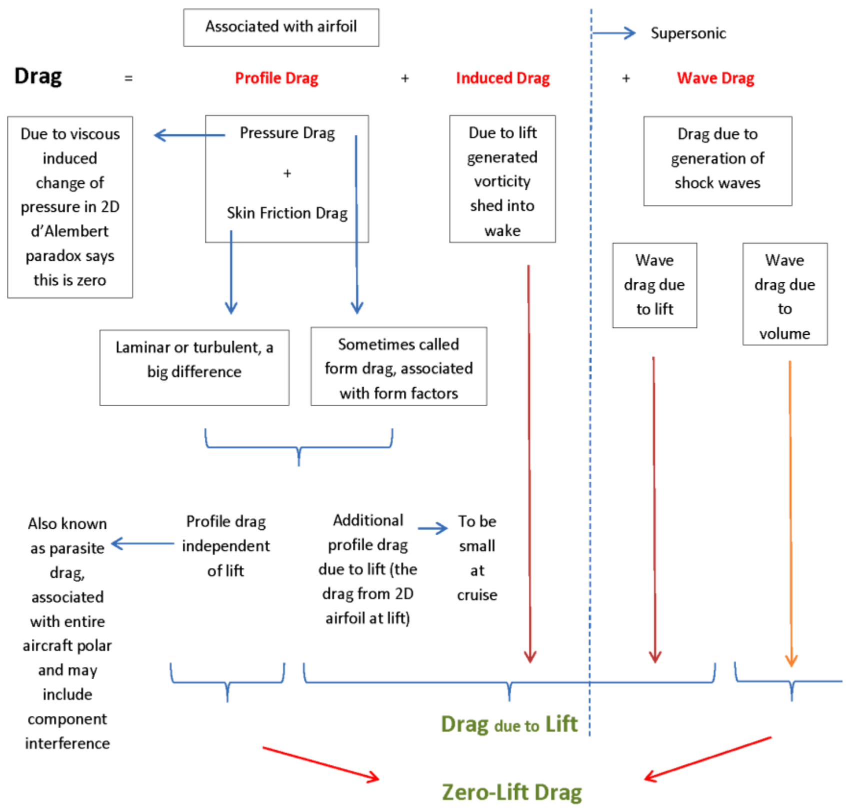

Figure 2.3-2 A broad-brush characterization of Drag

2.3.3 *Induced Drag*

In the case of delta wing aerodynamics considerable lift augmentation is provided by primary vortex suction which yielded large crossflow velocities and therefore the lift induced drag. Keeping in view the penultimate goal of high lift and high incidence objective of delta planform, insight on drag due to lift is imperative in comparative studies. Over the years considerable effort has been placed in in controlling the adversities associated with induced drag. The drag breakdown of a typical civil aircraft revealed that skin friction and induced drag accounts for 80% of the total drag [56] and thus tenders the highest potential of drag reduction.

Literature survey reveals that various methods have been adopted to decompose the drag components on basis of their physical origins. It has been established that two distinct mechanisms are responsible for the vorticity contained in wake of body translating through a viscous flow [57]. Under the inviscid flow assumption the absence of vorticity associated with boundary layer velocity deficit enlighten the viscosity independent aspect of the mechanisms involved. The inviscid flow exhibits the physics attributed to induced drag which resulted from the vorticity shed in the wake through distribution of circulation carried by the wing. It was shown that induced drag is independent of viscosity and can be resolved analytically through potential flow solutions about a body; Modern panel methods [58]. In this context the total drag is considered to be induced drag in absence of viscosity and for subsonic flow the mathematical model is based on elliptical PDEs and thereby numerical iterative methods are adopted to solve the equations hence no unique solution exists. Moreover the conformity of solution is sensitive to the specification of critical lines[1]. These inviscid solutions cannot handle all sorts of geometries and often terminates in accumulation of numerical errors. Experimentally, the induced drag can be calculated by subtracting the profile drag from the total drag. The real challenge lies in accurate prediction of profile drag, especially in the case of low aspect ratio wings. The initial step requires the body to be divided into infinitesimal strips and then 2D approximations are applied to predict the section profile drag. This, ideally, requires flow to be two-dimensional whereas in the case of delta wings or low aspect ratio wings the flow is predominantly three dimensional.

Recent research efforts have been utilized to compute the induced drag directly from flow field information. It eliminates the need of critical flow lines and roll-up models for trailing vortices but at the same association of viscosity with induced drag intricate the quantification of distinct components. In wake survey analysis, the Maskell formulation [51] is used to estimate the lift induced drag using the time averaged three-dimensional velocity measurements. Detailed insight into wake survey analysis can be found in Appendix.

Literature survey enlightens the fact that conventional wings have been extensively studied for induced drag reduction whereas no experimental evidence is presented for delta wings although analytical and empirical formulations are available but can only be used as reference [52]. It is to note that the theoretical approximation overestimates the drag as it assumes sharp leading-edge with zero leading-edge thrust.

[1] Lines along which the streamlines depart the surface of body

Chapter 3

3 Experimental Method and Apparatus

3.1 Flow Facility

The experiments were conducted in the *Joseph Armand Bombardier* wind tunnel located in the Aerodynamics Laboratory of McGill University Department of Mechanical Engineering. The open-loop facility is a Basic Aerodynamics Research Tunnel (BART) ideally suited to study the fundamental characteristics of complex flow fields. A 16 blades, 2.5m diameter isolated fan driven by a variable speed AC motor provided the desired suction. The high tone noise levels were extenuated through a specially designed acoustic silencer installed at the fan exit. The wind tunnel has a total length of 19 meters summed up by a 3.3m of contraction then a 2.7m of test section which is isolated from the downstream fan by a 9.1m 2-stage diffuser. It has a contraction ratio of 10:1 and test section that measures 0.9m x 1.2m x 2.7m in the vertical (y), horizontal/spanwise (z) and streamwise (x) directions. The schematic of wind tunnel is shown in Figure 3.1-1.

a)

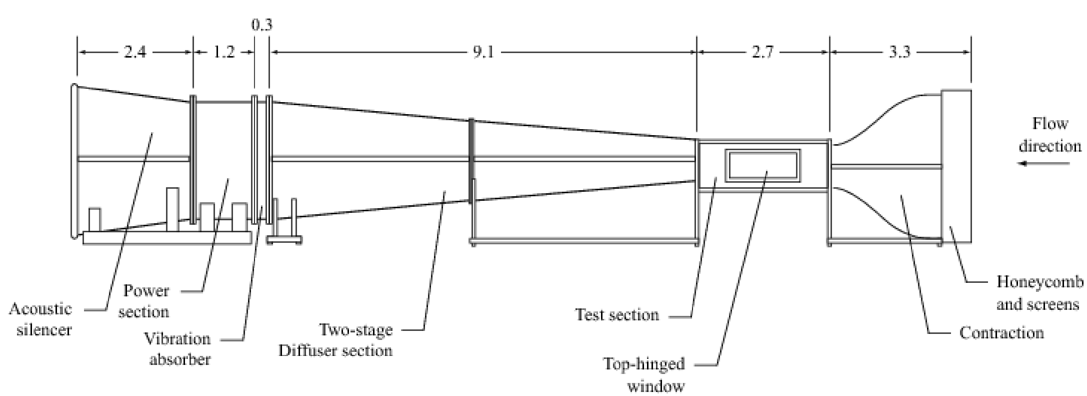

Figure 3.1-1 J.A. Bombardier wind tunnel schematic diagram

A combination of 10mm honeycomb and three anti-turbulence 2mm screens are responsible for the inlet flow conditioning along with providing a turbulence intensity of 0.05% at a free stream of 35 m/s. The flow speed was determined from a miniature pitot-tube installed at the start of the test section, connected to a Honeywell DRAL 501-DN differential transducer with a maximum water head of 50 mm where it was also calibrated against the fan speed and was precisely regulated by a digital controller.

Figure 3.1-1 Clockwise from top left a) Tunnel Inlet, b) Tunnel Outlet, c) Test Section, d) Fan and Acoustic silencer

3.2 Instrumentation and Data Processing

There are numerous flow conditions and critical points to be studied about a vortical flow field over a delta wing, which may include: a) the evolution in the apex region, b) formation and growth of leading-edge and secondary vortices, c) instability associated with separated shear layer, d) leading-edge sheet and vorticity feed, e) onset and location of vortex breakdown, f) aerodynamic characteristics and many more. Ironically, every single experimental technique possesses limitations and drawbacks hence selection of instrumentation was purposely based on the practicality and on the motivation behind the experiment. For example, flow visualization techniques are usually employed to capture the vortex breakdown over a delta wing where the information is primarily qualitative than quantitative but highly invaluable tool which provides a description of flow characteristics. Despite the apparent benefit, the underlying physics may even corrupt the qualitative details. In common practice, the diffusion coefficient of dye or smoke is rationally higher than the diffusion coefficient of vorticity, for this reason a discrepancy may exist in mass and momentum interface of vorticity and dye or smoke.

In practice, there is an intrusive and a non-intrusive way to investigate the vortical flow over a delta wing. Hence a brief description of available techniques is to precede the instrumentation used in the current study. It has been learnt that the vortical flow over a delta wing nurtures a suction region, which can be captured by employing the surface pressure taps. The resulting information can be integrated over the wing section to obtain the aerodynamic loadings. However, a considerably large number of pressure orifices are necessary to capture ample information which therefore results in oversize models and tedious to handle flexible tubings. Other intrusive way of obtaining invaluable information is hot wire anemometry where sensor response accurately follows the flow behaviour while offering high frequency response. The resulting time accurate measurements are conducive and can be studied for shear stress and turbulence investigations. But despite the benefits, the large probe size limits the allowable inlet flow angle and also the inability of probe to detect flow reversals. Among the non-intrusive ways, Laser Doppler Velocimetry is a pointwise technique which is relatively expensive and often the data rate is limited in vicinity of a surface with poor signal-to-noise ratio. Lastly there is Particle Image Velocimetry (PIV) which encompasses global flow field information but near-to-surface application arise some complications.

3.2.1 Seven-hole pressure probe

In present study, to quantify the evolution and development of vortical flow field over the delta wing models, time averaged measurements were obtained using the seven-hole pressure probe system which is an improved version of conventional five-hole probe. The addition of two more holes is to extend the probe acceptance angle up to 70^{o} and also significantly reduces the ineffective probe area due to flow separation which compromises the probe sensitivity. In practice, a basis of four-hole is required to accurately compute the velocity vector therefore the only significant disadvantage over the five-hole probe is the recording of additional two pressures at each grid station. The three-dimensional velocity field was then computed by differential of pressure information at the location of the probe tip. It is to note that hot wire anemometry can also provide three-dimensional time-averaged velocity information, but in comparison it has a larger probe tip which comprises the resolution and moreover it cannot provide the all-important pressure information. The present seven-hole probe system is comprised of three basic components, a pressure probe, the transducer array and the signal conditioner.

The brass tip constitutes of seven pressure taps in a conical frustum shape with one located in the center and the remaining six around periphery of the 30^{o} cone. The outer diameter of the probe tip is ~2.7 mm whereas each individual hole is of ~0.5 mm diameter held by a 130 mm probe shaft which was further extended, to distance the downstream traverse from upstream wing model, by a 400 mm aluminum sting. Each tap was connected to the transducer array via 1.6 mm diameter and 550 mm long tygon tubes.

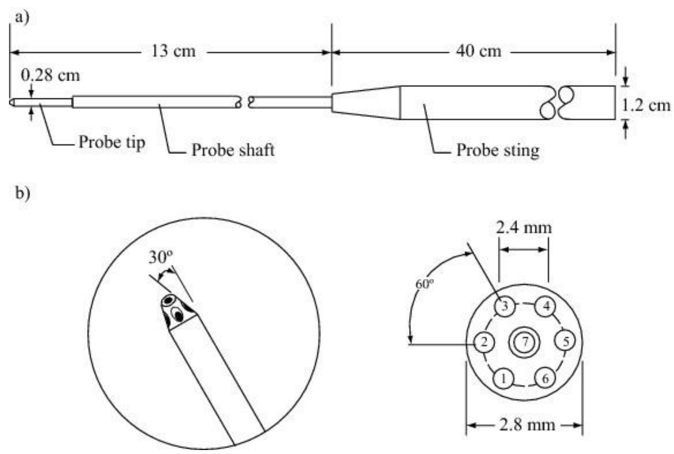

Figure 3.2-2 Seven-hole probe geometry, a) probe and sting assembly, b) details of probe tip

The pressure transducer array is a series of seven Honeywell DC005NDR5 differential transducers with a maximum water head of ~127 mm (5 in). It was attached to the traversing mechanism while atmospheric pressure from inside a covered damping unit was provided as a common reference pressure to all the transducers.

The signal conditioning is a custom-built system consists of seven-channel analogue signal differential amplifier with an external DC Offset of 3.5 Volts and provides a fixed gain of 5:1. Over the calibration range, the transducers are highly linear with in ~2% and approximately have a resolution of 125 Pascal/Volt. Since the time-averaged measurements made by seven-hole probe were steady therefore mitigates the need of analogue or digital filtering. Furthermore the tygon tubings were long enough to hydraulically damp any noise greater than 5Hz. The output from signal conditioning unit was then fed to a data acquisition system programmed by LabVIEW and signals were monitored using the oscilloscope. The calibration was done in situ by using a purpose-built calibration stand, following the procedures described by Birch [59] based on Wenger and Devenport [60].

Finally, the seven-hole pressure probe was held through a 2-axis autonomous traversing mechanism equipped with Sanyo Denki model 103-718-0140 stepper motors for the y-direction and a Biodine model 2013MK2031 stepper for the z-direction. The system was made functional by a NI PCI-7344 4-axis motion controller operated through LabVIEW. This enables data information to be gathered against a desired grid file. The spatial resolution of the traversing mechanism is ~ 20 μm and ~60 μm for translation in y and z direction respectively. An extended probe holder was employed to curtail the blockage - effects on the upstream wing models.

Over the years, pressure probes have facilitated considerable research effort vis-à-vis delta wings hence the implication of intrusive nature was also studied. Payne et al. [22] examined the question posed by probe interference and their explanation was case dependent. His intrusive method involved a 2.8 mm seven-hole probe while LDA measurements were carried for non-intrusive data acquisition. It was inferred that probe interference is dependent on state of the vortex. They further concluded that seven-hole probe is more accurate when predicting the flow over the wing while the breakdown is aft of trailing-edge and in the post breakdown region. In contrast, LDA is more reliable when the breakdown is in vicinity of the wing. In addition, series of experiments were also conducted across the breakdown which showed the inability of seven-hole probe to detect the reverse flow while LDA sensed the recirculation zone.

The foremost challenge lies in the calibration of pressure probe because various techniques were devised over the decades and each technique has its own way of handling the information. The undertaken calibration technique is adopted from Zilliac [61, 62] which require grid information against a known dynamic pressure. Unlike the frequent rectangular planar grid, the data is acquired over a hemispherical surface against a matrix of known pitch and yaw angles. Then the probe is placed in an unknown stream then interpolation over the calibration information yields total and static pressures along with three-dimensional velocity information. The uncertainty in data acquisition is under the combined effect of probe geometry, traversing mechanism, transducer sensitivity, and free stream dynamic pressure. The calibration returns empirical relations linking the flow angles with local pressure coefficients for each of the individual hole. The computational efficiency of these numerical relations plays a vital role in data processing. As we know, there exist various methods, both mechanical and numerical, to extract pressure and velocity information from the flow. Each one of them incorporates distinct data reduction techniques to resolve for detail flow variables. The time required to transform the pressure transducer data into usable flow information plays a decisive role in structuring the reduction algorithm. For example if a grid comprises of 5000 points is to be resolved and a delay of half a second at each point will eventually cost ~40 minutes of computational time.

3.2.2 2-axis Force Balance

Unlike the one-piece external balances where single piece of material equipped with strain

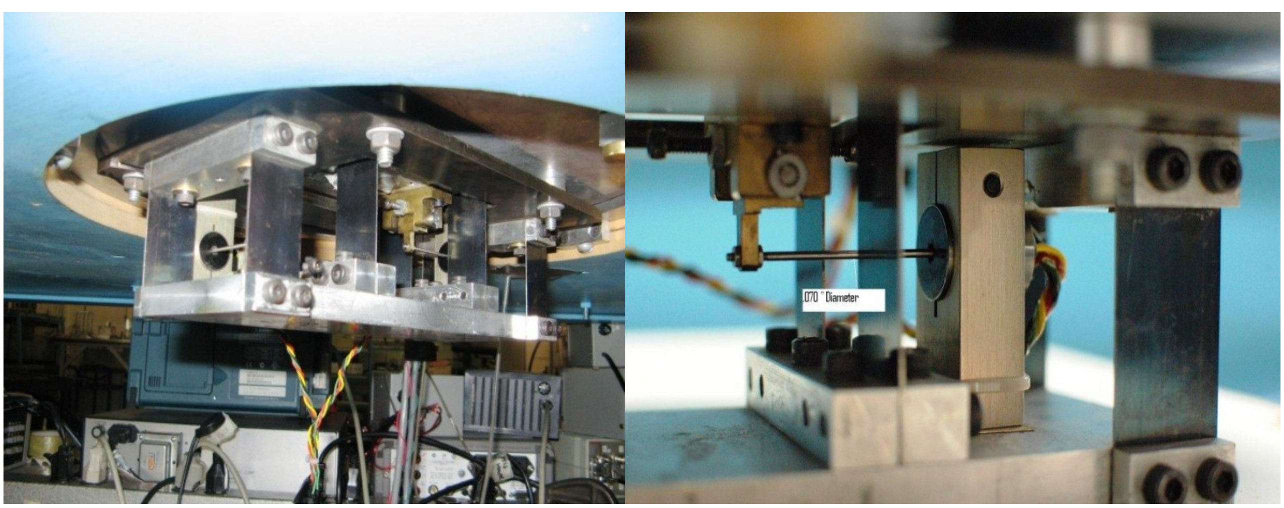

Figure 3.2-3 Left) High quality flexural platform consist of two plates with two sets of two parallel reeds or flexures, Right) Drag LVDT sensing the platform cantilever displacement

gauges sense the aerodynamic loads, an external type made up of force transducers connected through a framework is used for the load sensing. The balance is optimally designed for decoupling of load interactions and was theoretical based on two high quality flexural platforms each consisted of two plates with two sets of parallel flexures, shown in Figure 3.2-3**.** This arrangement augments the sensitivity in one-direction while making it extremely stiffer in right angles to it. The spring steel flexures allow each platform a maximum cantilever deflection of 5mm which were independently measured using two Sanborn 7DCDT-1000 linear variable differential transformers (LVDT). The force balance was calibrated in situ over a range of force increments encompassing the expected experimental loadings. It is to mention that over the calibration range the response of individual LVDT was linear within a range of ~1%.

3.3 Test Models and Parameters

3.3.1 Wing Models and Support Mechanisms

The experimental investigation was carried over two different delta wing models, DW65 and DW50 shown in Figure 3.3-1. As the topic suggests, vortex flow and aerodynamic characteristics were studied for the slender (DW65) and non-slender (DW50) delta wing. Both the wing models were fabricated from an aluminum plate of 0.25” thickness and windward leading-edge and trailing-edge bevelling was done to sharp the edges. The dimensional tolerances on the model were 250 µm on the chord, span and model thickness. The key features of the two wings are summarized in Table 3-1**.**

Table 3-1 Key features of the two delta wings

			DW65	DW50
Wing span	b	in	15.5	20
Root chord	c	in	16.5	12
Aspect ratio	AR		1.87	3.33
Wing area	S	in^2	128	144
Sweep	Λ	deg	65	50
Bevel	σ	deg	15	15
Thickness	t	in	0.25	0.25
Thickness/Chord	t/c	%	1.5	2

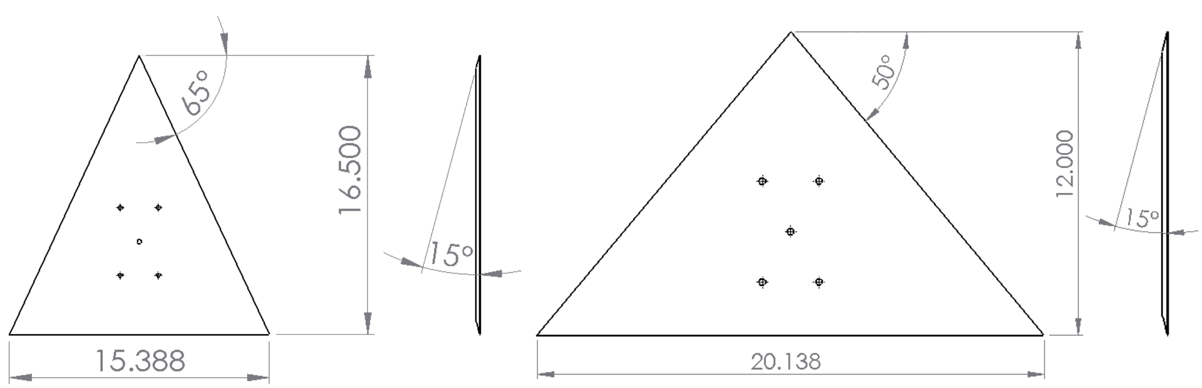

Figure 3.3-1 Sketch of DW65 and DW50

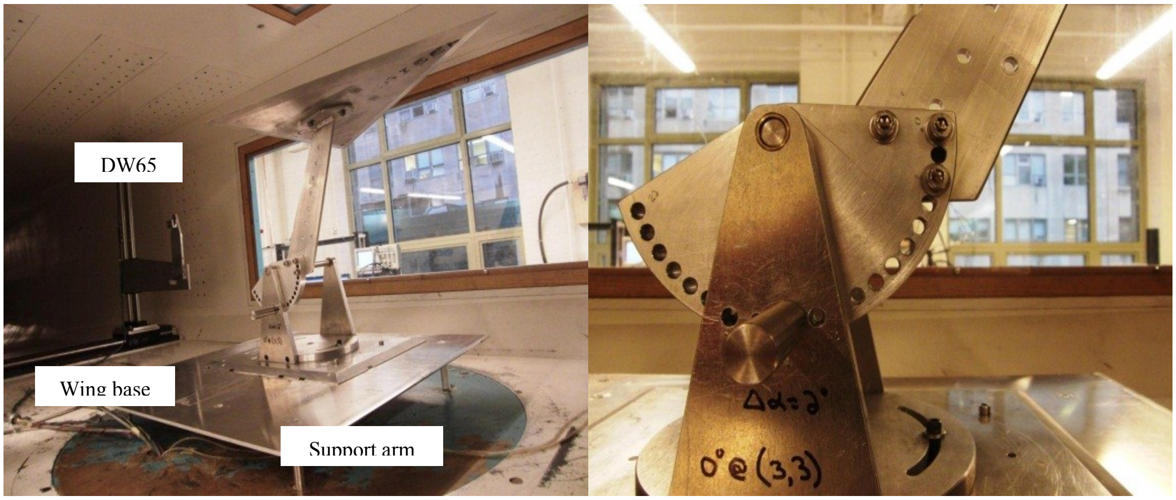

Figure 3.3-2 Left) Wing, holding arm and base arrangement Right) Static pitching mechanism

In order to properly secure the delta wings, two separate arrangements were devised for static flow field and direct force-balance measurements. In the former the wing was securely fastened to a mechanical pitching mechanism shown in Figure 3.3-2. The crank-like base allows a minimum increment of 2^{o} and defines a range of angles through different combination of holes. To isolate the base effects while ensuring minimum aerodynamic resistance and model sleekness, two identical holding arms were machined for each delta wing from a 1/4" aluminum plate. The idea behind the design is to mitigate the effects of flow disturbance on the delta wing while respecting the model rigidity. It has been understood that trailing-edge is a primary contributor towards the adverse streamwise pressure gradient therefore the positioning of wing attachment significantly affects the quality of flow over the wing. In present design the wing-arm attachment was located at x/c = ~0.75.

For the latter, direct aerodynamic measurements, the support mechanism was designed to use the same wings. The arrangement shown in Figure 3.3-3 was made to place the wing vertically with the tunnel floor so as to align the two axes of the force balance with the wing normal and tangential axes. The delta wing models were mounted vertically above the 0.25 in x 24 in x 24 in aluminum plate with sharp leading-edge to mitigate the effects of flow separation at wing tip region. An optical post was used to transfer the wing loadings to force balance sensing platform using the same support arm employed for the vortical flow analyses. Beneath the aluminum plate with tunnel floor an aerodynamic fairing is placed around the shaft to isolate the effects of oncoming wind tunnel flow which will otherwise corrupt the force measurements. The force balance system was mounted beneath the wing model on a turntable installed on tunnel floor provided that the whole sensing arrangements were placed outside the wing test section.

3.3.2 Experimental method and Parameters

The primary objective behind the experimental investigation was to document the flow behaviour and critical flow parameters with change in incidence and chordwise distance. A comparison of direct and indirect aerodynamic measurement is also a part of current investigation. Figure 3.3-5 summarizes the different aspect of current experimental investigation. Note that seven-hole experiments were run at 15 m/s and few high angles of attack cases for DW65 at 12.5 m/s. The origin of the Cartesian coordinate system was measured from wing apex with x, y, z aligned with streamwise, vertical and horizontal

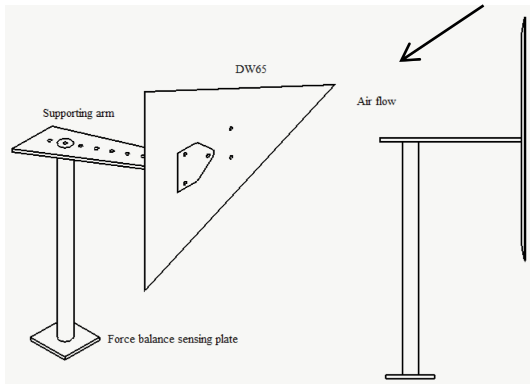

Figure 3.3-3 Arrangement for direct force measurements

directions, respectively. Moreover, the measurement planes were placed normal to the tunnel floor where the wing was installed in line with the tunnel floor, i.e. spanwise is the horizontal direction. The ranges of angle of attack and chordwise station were chosen to encompass the conditions of coherent vortical flow (pre-stall). The upstream proliferation into the vortical flow field was limited by the data resolution, i.e. probe size, therefore closest possible measurements from wing apex were made at x/c = 0.3. Moreover the support mechanism allowed a minimum increment of 2° and 0.5° of angle of attack for seven-hole probe and force balance experiments, respectively. In streamwise direction the measurement planes were separated by 0.1c and under certain circumstances it was dropped down to 0.01c to locate the vortex breakdown.

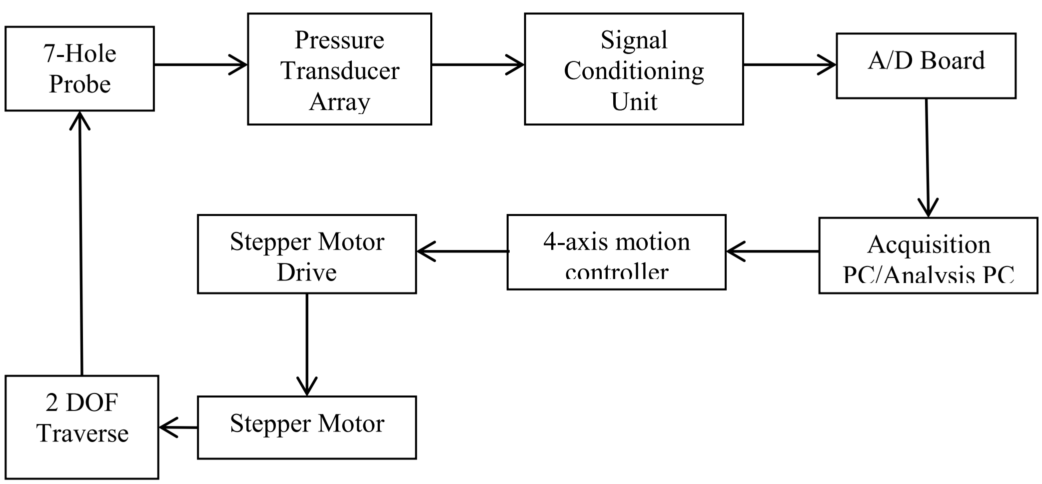

Figure 3.3-4 Flow chart for the seven-hole probe equipment setup

3.3.3 Data Acquisition and Reduction

The signal data was acquired by using a 16-channel, 16 bit NI-6259 A/D board powered by a Dell Dimension E100 PC and a NI BNC-2110 connector box accepts the transducer outputs. Note that under steady time-averaged scenarios the sampling frequency has a direct implication on data quality and cleanliness; it can impede or expedite the data

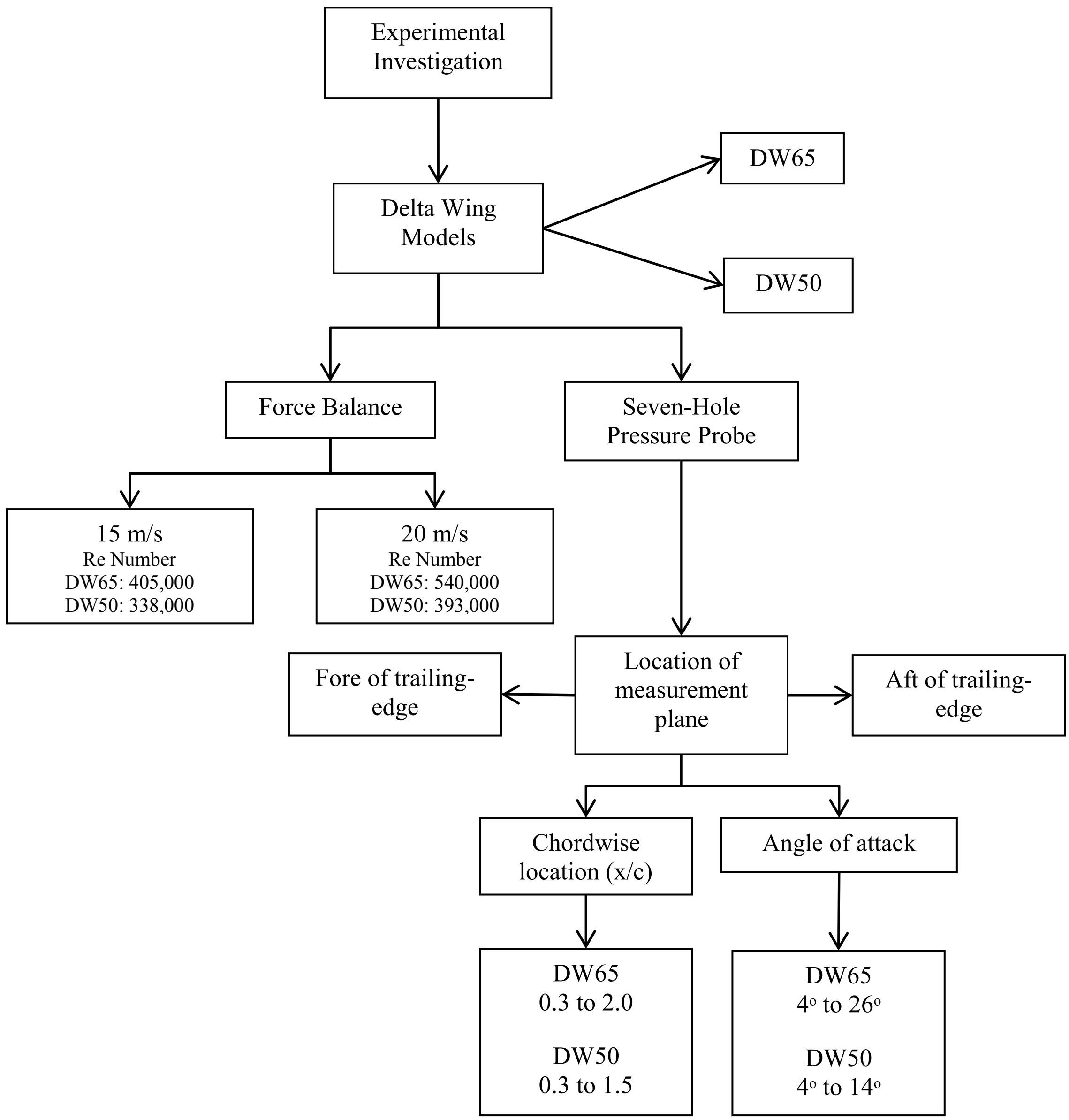

Figure 3.3-5 an overview of experiment plan

acquisition process. Not only sampling at low frequency will escalate the chance of missing tangible flow information but the quality can also be compromised by sampling at higher than required frequency therefore increasing the chance of data corruption by recording the undesirable high tone noises. Therefore different sampling frequencies were tested to ensure convergence but, as discussed, the hydraulic damping of the tygon tubing and their corresponding size did the desired extenuation of noise levels. In the case of seven-hole probe, the sampling rate of 500 Hz was selected for total of 5000 samples. Figure 3.3-4 highlights each station from probe tip to useable digitized output[1].

The scan grid was placed perpendicular to the tunnel floor where the size and boundaries were case-dependent. The grid points were varied from 500 - 5000 in order to accommodate the growth and trajectory of the vortical flow over and off the wing. Note that the scan grid can be as dense and as large as possible but it considerably increases the scan time and such long hours can prove detrimental for proper functioning of the equipment. Therefore ensuring the capture of minor details while respecting the scan time, an adaptive grid was adopted as shown in Figure 3.3-6**.** In the case of DW65 and DW50 the grid spacing was varied from $\Delta y = \Delta z = 1.6$ cm (1/16") to 6.4 cm (1/4") and from $\Delta y = \Delta z = 1.6$ cm (1/16") to 3.2 cm (1/8") depending on the point location, respectively. Similarly,

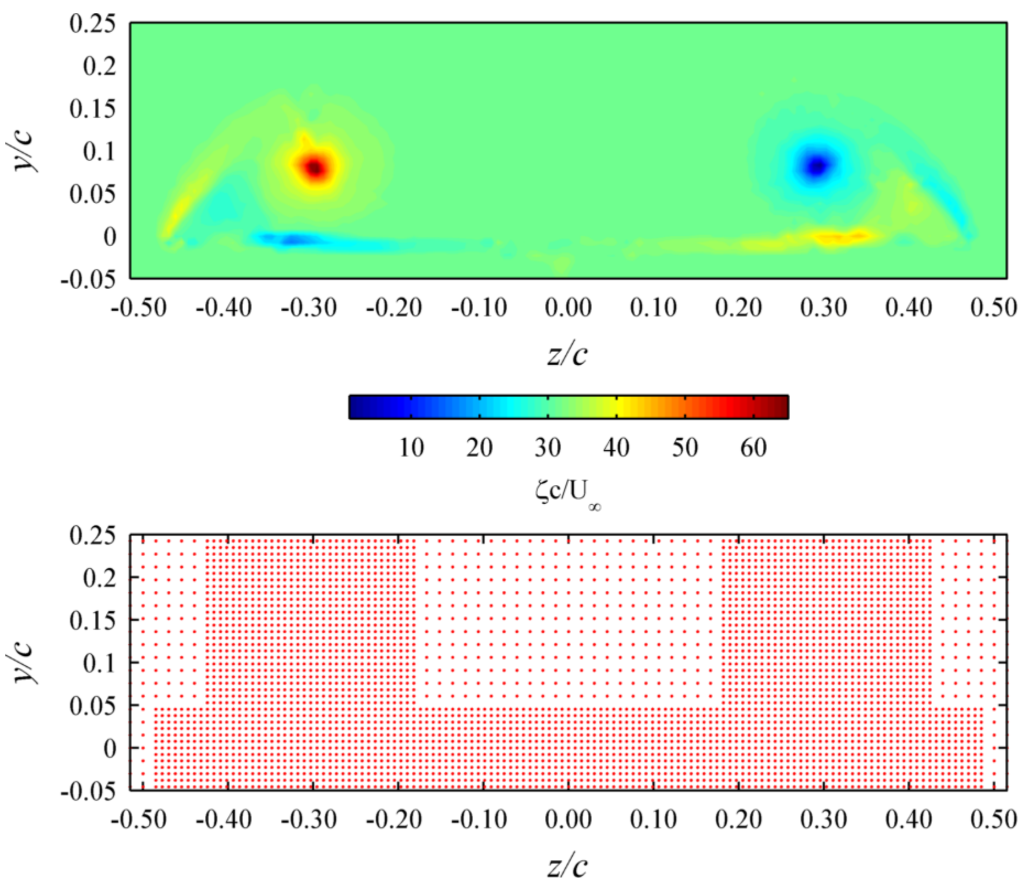

Figure 3.3-6 Top) DW65_a14_x1.02 axial vorticity filled contours, b) Adaptive grid

the resulting scan resolution was thereby varied from 0.35 to 1.5 of $\Delta z/c$ and from 0.50 to 1 of $\Delta z/c$. The final data was presented based on the highest resolution hence the coarser grids were interpolated to the finest grid resolution. This was accomplished by first

[1] Data file with voltage outputs of seven holes against each grid point

translating the raw data and then interpolating the region with low resolution and replacing the interpolated points with actual data points.

The data was presented just aft of trailing-edge (x/c = 1.02) in wake of DW65 at an incidence of 14°. The grid has 4290 points which approximately equates to 9 hours of scan time. The three-dimensional velocity information was then manipulated for the determination of various vortical flow quantities, i.e. vorticity, circulation, tangential velocity, and critical vortex parameters. An overview of mathematical operations undertaken for aforementioned quantities was given below.

The axial vorticity was calculated from planar two-dimensional velocity data (v and w) by applying second order difference scheme. However given the grid location of each point, three different methods were used; central, forwards and backward difference. The following equation summarizes the numerical procedure.

$$\zeta_{i,j} = \left(\frac{\partial v}{\partial z} - \frac{\partial w}{\partial y}\right) \approx -\left(\frac{\partial v_{j+1,i} - \partial v_{j-1,i}}{2\Delta z} - \frac{w_{j,i+1} - w_{j,i-1}}{2\Delta y}\right)$$

Note that the absolute value of the vorticity is highly dependent on indexing in other words the minimum distance between two data point. For this reason, grid resolution is a prime contributor towards the numerical sensitivity of absolute vorticity values.

The circulation can be calculated by integrating the tangential velocity around a closed contour or by integrating the product of vorticity and area or Stoke's theorem. The following mathematical relations elucidate the aforementioned methods:

$$\Gamma_o = \sum\sum \zeta_{i,j} \times \Delta y \Delta z \qquad r_{i,j} < r_o{}^1$$

$$\Gamma_c = \sum\sum \zeta_{i,j} \times \Delta y \Delta z \qquad r_{i,j} < r_c{}^2$$

$$\Gamma_o = \sum\sum v_{\theta i,j} \times r_i \qquad r_{i,j} < r_o \, \Gamma_c = \sum\sum v_{\theta i,j} \times r_i \qquad r_{i,j} < r_c$$

Where:

$$r_{i,j} = \left(z_j - z_c\right)^2 + (y_i - y_c)^2 r_o = r\left(\zeta = 0.01\zeta_{i,j\,max}\right)$$

$$v_{\theta i,j} = \left(v_{i,j} - v_c\right)\sin\theta - \left(w_{i,j} - w_c\right)\cos\theta$$

[1] Origin of polar coordinate: Vortex center (z_c , y_c)

[2] Defined by Hoffman and Joubert, radius at which the tangential velocity is maximum

Chapter 4

4 Result & Discussion

This chapter presents and discusses the experimental results obtained for 65° and 50° delta wing employing the aforementioned experimental techniques, namely seven-hole pressure probe, force balance and wake survey analyses. It is divided into two main sections; one characterizes the vortical flow while the other covers the aerodynamic aspects of the wing models. In section 4.1 and 4.2, the variations of vortical flow will be studied vis-à-vis chord distance and angle of attack, respectively, paying particular attention to the cases with breakdown downstream of trailing-edge. The variation shall be scrutinized by presenting the general behaviour of the vortex and detail vortical flow parameters, i.e. axial velocity, swirl velocity, vorticity and circulation. However in section 4.3 wake vortex evolution will be discussed, especially for the cases when breakdown reaches the trailing-edge. It elucidates the detrimental interaction between the regions of opposite sign vorticity in absence of vorticity feed. Finally, section 4.4, will conclude the discussion on vortex flow characteristics by explaining the behaviour of critical flow quantities in vicinity of vortex breakdown. The last two sections 4.5 and 4.6 concentrates on the estimation of aerodynamic loading, i.e. lift and drag, respectively. It includes a comparison of direct and indirect computation of aerodynamic coefficients while a comparison of indirect lift computation models will also be presented. In addition, significant research effort will be devoted towards the drag characterization especially the calculation of induced drag. Lastly, the sectional distribution of aerodynamic loads will also be discussed in relation to vortex location.

It is to mention that constraints offered by the instrumentation and flow structure demanded the experiments to be conducted under dissimilar conditions for the slender and non-slender delta wings. Table 4-1 summarizes the flow conditions for a range of angle of attacks. Unless otherwise mentioned, the free stream velocity respected the given table and the said selections were made to ensure the smooth running of the system while achieving the maximum possible Reynolds number

Table 4-1 Flow conditions for different model and angle of attack

Wing	Angle of Attack	Reynolds Number	Free Stream
	(degree)	(chord)	(m/s)
DW 65	4 to 18	405,000	15
	18 onwards	338,000	12.5
DW 50	4 - 14	290,000	15

In order to check the conformity of delta wing models, a detailed characterization of the vortical flow was carried out to serve as a reference. Measurements were made over and beyond the wings at different chordwise locations at various angles of attack. The first set of data provided the basis for further investigation and complemented previous works. The following subsections discuss the variation in vortex characteristics over the wing. Particular attention is given to the evolution of flow fields, vorticity distributions, critical vortex quantities and confined circulation with increasing incidence and downstream distance.

4.1 Variation of vortex characteristics with streamwise location

The evolution and streamwise development of leading-edge vortices is discussed in this section. An insight on development of vortex along the span can be elucidated by defining the vortex characteristics at progressive chordwise stations.

A qualitative representation of chordwise progression of leading-edge vortex over the DW65 at $\alpha = 16^o$ and Reynolds number of 409,000 is presented in Figure 4.1-1 (Top, a, b). It is to note that at the selected incidence the vortex breakdown is in vicinity but downstream of trailing-edge. It was deduced from the iso-contours of axial velocity given in Figure 4.1-1 (Top, a) that as the vortex developed over the wing, it was characterized by islands of axial velocity excess and deficit. The correlation between these flows is often important in predicting the near-future state of the primary vortex. It can be visualized that near-to-the-surface secondary vortex increases in strength with primary vortex for few fractions of chord length then it suffered a drop in strength and so do the associated drop in wake-like axial velocity due to the much anticipated boundary layer and vortex flow interaction. Figure 4.1-1 (Top, b) presents the streamwise evolution of normalized axial vorticity scaled by local semi-span. The vorticity concentration increases with downstream distance whereas there witnessed a gradual drop in trailing-edge region, which is due to the upstream propagation of free-end effects, i.e. adverse axial gradient. This tempering of flow field was complemented by a gradual drop in maximum axial and core velocity u/U_∞ and u_{core}/U_∞ respectively given in Figure 4.1-3 (c, d). The implication of trailing-edge in the case of a delta wing is similar to that of tip region in the case of a conventional wing where distancing the free end helps lessening the related adverse effects.

In order to understand the overall behaviour of leading-edge vortex the variation of axial vorticity ($\zeta s/U_\infty$), axial velocity (u/U_∞) and tangential velocity (v_θ/U_∞) with radial distance along a horizontal line passing through the vortex center is plotted in Figure 4.1-2**.** Firstly, the self-similar behaviour of the vortex flow quantities, for both cases, $\alpha = 10^o$ and 16^o, when non-dimensionalized by local semi-span confirms the conical nature of the flow. It is observed that vorticity decayed rapidly with distance from the vortex center while a secondary peak is witnessed towards the leading-edge side, indicative of feeding vorticity confined by the separated shear layer. Similarly, the axial velocity is plotted across the

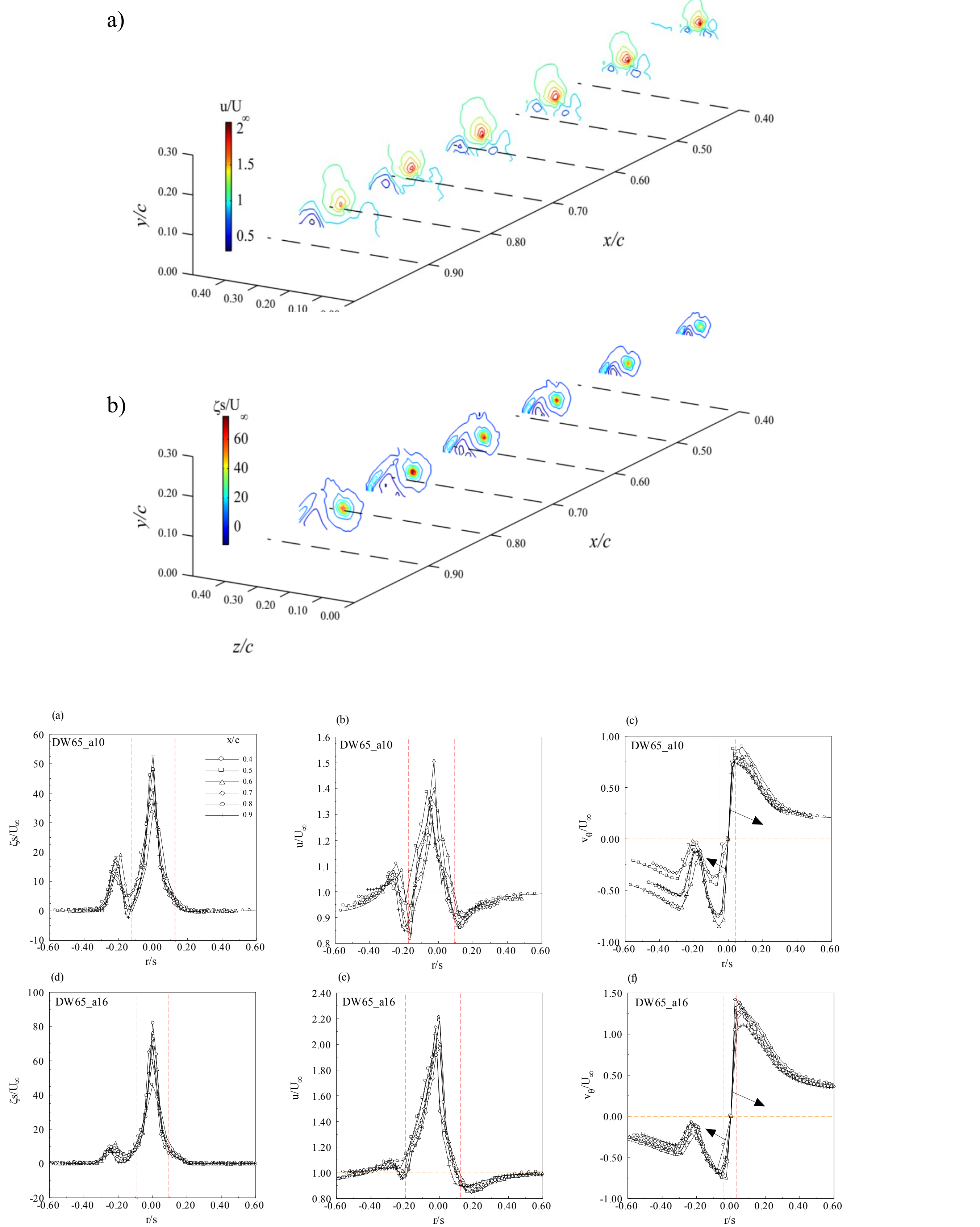

Figure 4.1-1 (Top) Streamwise evolution of mean axial velocity a) u/U_∞ and b) $\zeta s/U_\infty$ over DW65 at an incidence of 16^o, (Bottom) Vortex flow quantities measured across the static vortex center, (a-c) DW65 at α=10° and (d-f) DW65 at α=16°

vortex center in Figure 4.1-1 (Bottom, b, e). At all streamwise stations the size of axial core is larger than the vorticity core which typifies the strong entrainment of flow in axial direction along with the wide spread of favourable gradient. The extent of axial and vorticity core is approximately 40% and 20% of the wing semi-span respectively. The

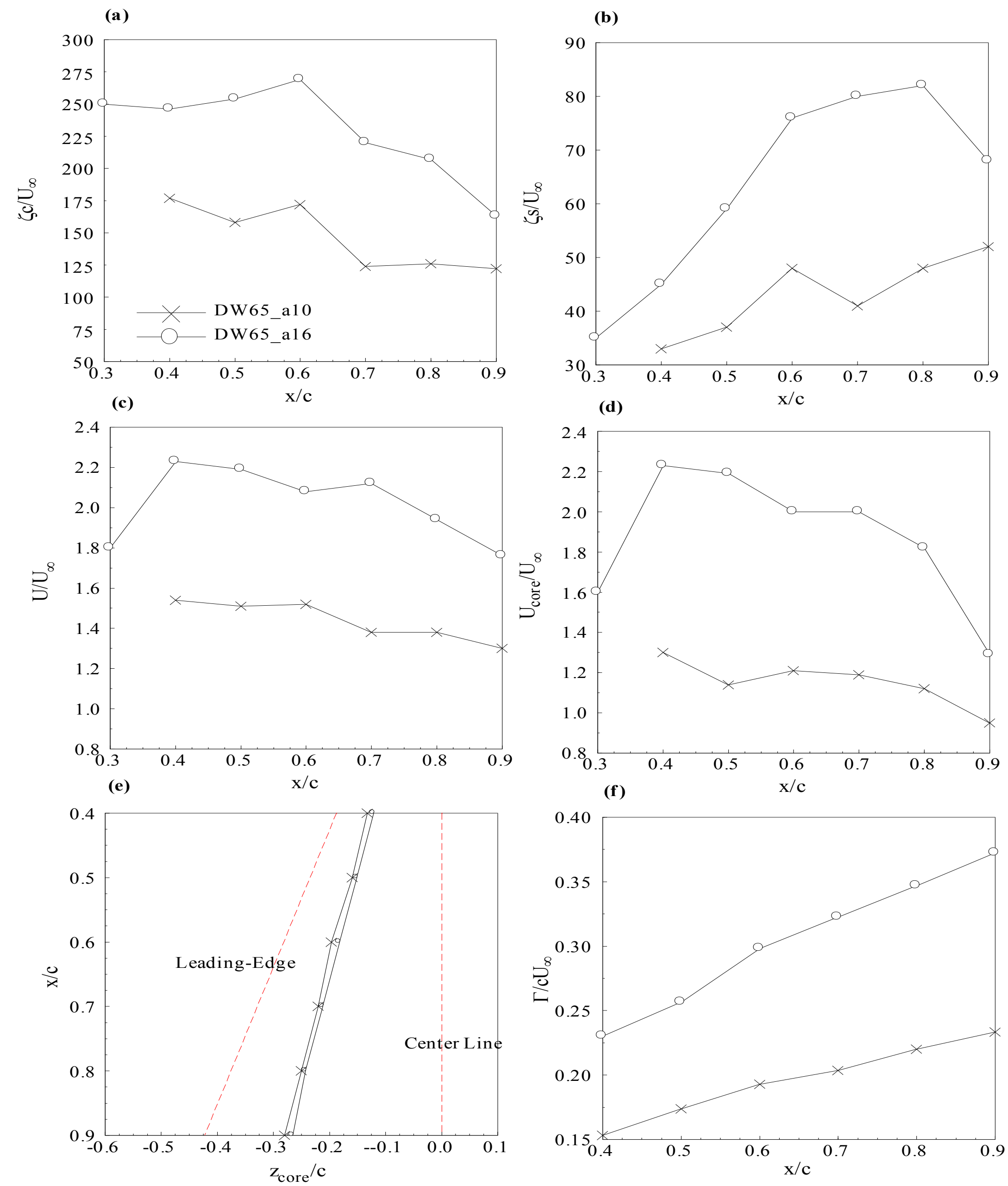

Figure 4.1-2 Variation of critical vortex quantities with x/c for α = 10° and 16°, (a) peak axial vorticity w.r.t chord; (b) peak axial vorticity w.r.t local semi-span; (c) maximum axial velocity, (d) core axial velocity; (e) vortex spanwise trajectory; (f) total circulation

wake-like core flow characteristic of secondary vortex is observable towards the leading-edge side of the primary vortex. Figure 4.1-1 (Bottom, c, f) illustrates the development of tangential velocity about the vortex center where it display strong gradient rather confined within >10% of the local semi-span. This supplemented the tight confinement of vorticity within the vortex core. As the distance from the vortex center increases, the intensity of swirl in the flow asymptotically vanishes. The differential in absolute peaks showed that tangential velocity is higher towards the wing centerline because the shear layers are rolling up in clockwise direction hence intensifies the flow in outer half of the primary vortex where in some cases the maximum tangential velocity even exceeded the free stream velocity.

Further insight on variation of vortex flow over a DW65 is developed by investigating the streamwise evolution of critical vortex quantities with increasing distance from the wing apex, illustrated in Figure 4.1-2. Over the wing, the separated shear layer kept on feeding the leading-edge vortices resulting in substantial increase in normalized vortex strength. From x/c = 0.3 to 0.8, there was a progressive increase in normalized vorticity $\zeta s/U_\infty$ and linear increase in normalized peak spanwise circulation Γ/cU_∞ as the free shear layer/leading-edge sheet continually feeds the vortical flow over the wing. Moreover, it appeared that streamwise value of vorticity decreases when scaled by root wing chord given that no breakdown existed over the wing.

The normalized peak tangential velocity[1] at each chordwise station is given in Figure 4.1-3. In the case of DW65 at $\alpha = 16^o$ the tangential velocity increases with chordwise distance up to x/c = 0.7 then suffered a sudden drop. This opposing trend can be attributed to the diffusion induced by aforementioned trailing-edge effect. Figure 4.1-2 (c, d) revealed that, for $\alpha = 16^o$, the maximum core axial velocity almost remained constant up to x/c = 0.7. Keeping in view that with downstream distance, despite the increase in vortex size and corresponding decrease in vorticity feed, vortex managed to stabilize the high core axial velocity (~2.2 times the free stream). Therefore the aforementioned axial gradient is utilized to accelerate the ever increasing core until the trailing-edge effects alters the flow condition (x/c > 0.7). It is also interesting to note that for $\alpha = 16^o$, the numerical value of v_θ is always higher than the free stream velocity.

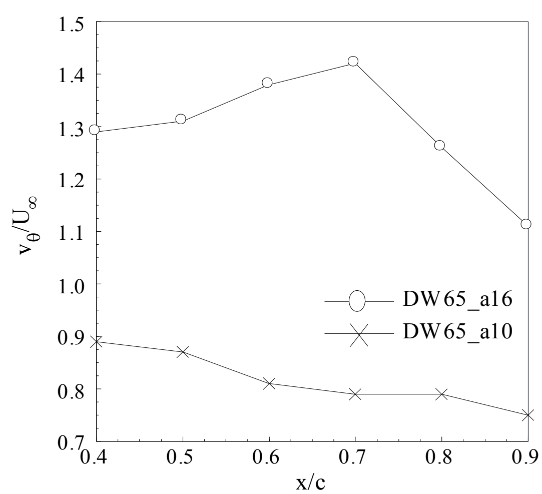

Figure 4.1-3 Variation of peak tangential velocity with chordwise distance for DW65

The values given in Figure 4.1-2 (a, b) are the maximum numerical values of vorticity computed against a single grid location. Moreover, the vorticity field was calculated by differentiating the discrete velocity data and the corresponding details of the velocity

[1] Presented values are for the side with higher tangential velocity, towards the wing centerline

gradient are highly sensitive to grid resolution. Therefore this numerical procedure often resulted in an amalgamation of errors. This may be overlaid by investigating the circulation about the vortex center[1] which also plays a pivotal role in determination of aerodynamic characteristics, especially the lift.

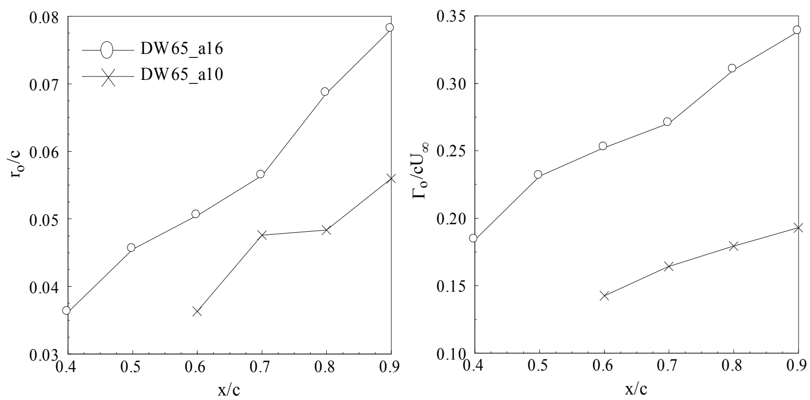

Figure 4.1-4 Variation of (left) normalized outer radius and (right) normalized outer circulation for DW65_a16

Vortex outer radius[2] and circulation are given in Figure 4.1-4. Unlike the trailing tip vortices, leading-edge vortices are in vicinity of wing surface and, as mentioned, are constantly fed by leading-edge sheet therefore distinct definitions can be adopted to define the vortex outer limits. The streamwise growth of the leading-edge vortex, both in size and strength, is observable. From x/c = 0.4 to 0.9, vortex witnessed respective growth of ~115% and ~83% in size and circulation at an incidence of 16°. This can be interpreted as, in streamwise direction prior to the breakdown; the relative increase in vortex size is higher than the relative increase in circulation about the vortex center which is an indicative of a slackening of the spiralling shear layer in the later stages of vortex development.

Figure 4.1-5 presented the planar representation of axial velocity and vorticity field for DW65 at an incidence of 10°.

[1] Grid location corresponding to maximum vorticity is regarded as vortex center

[2] Normalized distance between vortex center and radial location where vorticity reaches 1% of the maximum vorticity

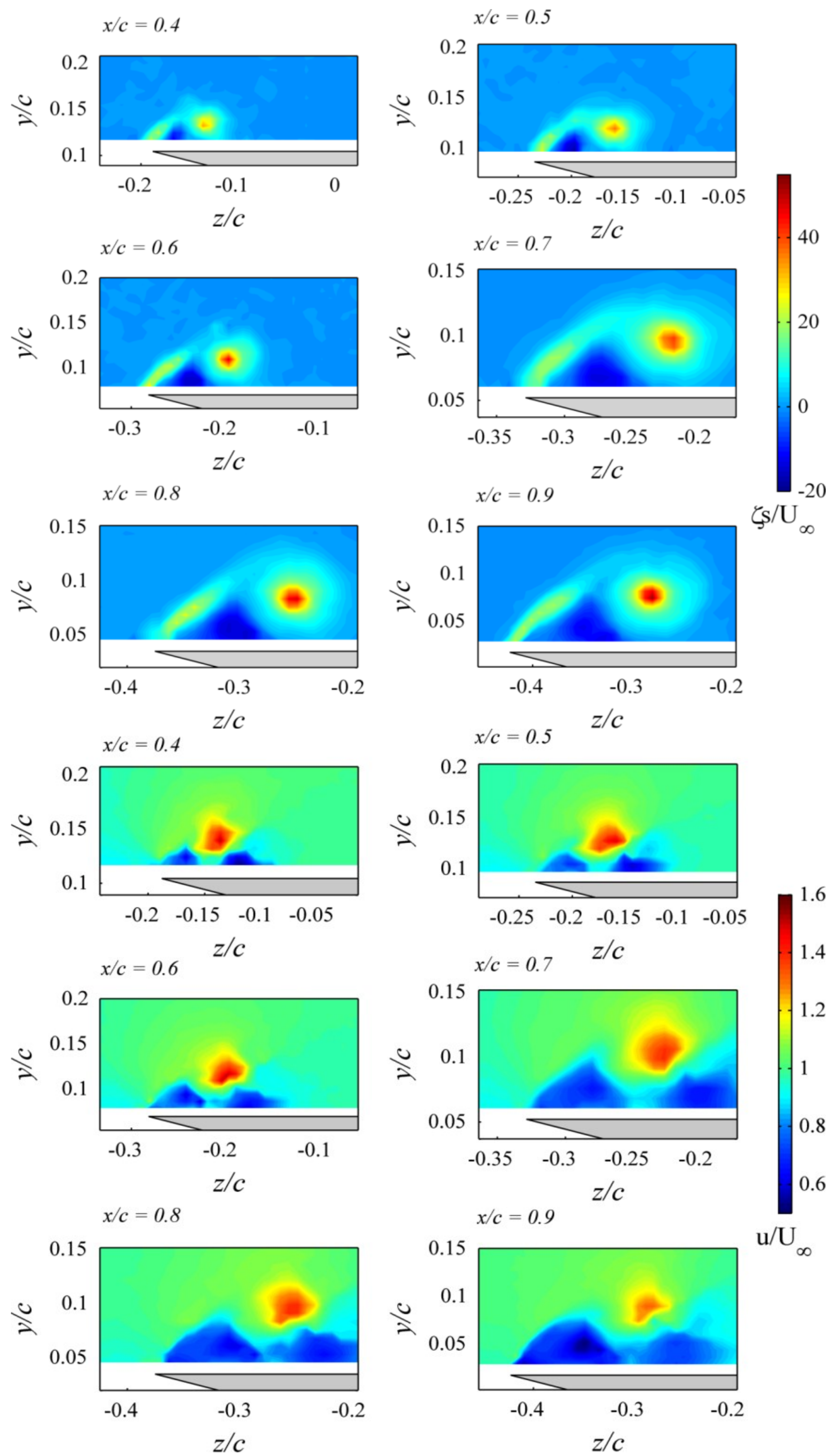

Figure 4.1-5 Variation of normalized axial vorticity and axial velocity fields, DW65 at α = 10°

In the case of DW50, the acquired information is more qualitative than being quantitative. Firstly, the formation of leading-edge vortex is much closer to the wing surface which complicates the probe placement and resulted in detrimental probe interference. In addition, the vortex is relatively weak and characterized by wake-like core axial flow. The accurate capture of vortical flow field is further dented by the early breakdown over the wing at low angles of attack. Recall that, from literature survey it has been understood that for DW50, the vortex breakdown crosses the trailing-edge in vicinity of $\alpha = 5^{o}$, keeping in view the instability and disorganization induced by vortex breakdown, it was preferred to acquire data only for low angles of attack. In coming sections it has been concluded that the subsequent detrimental effect of vortex breakdown was observable in computation of

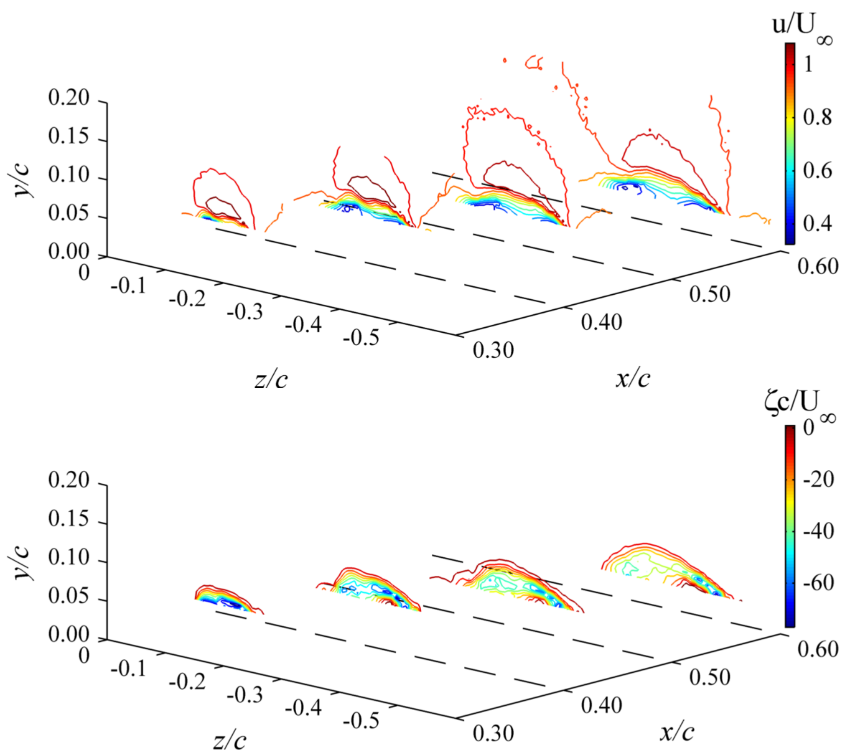

Figure 4.1-6 Streamwise variation of normalized axial velocity and vorticity iso-contours for DW50 at $\alpha = 6^{o}$

aerodynamic characteristics of the non-slender delta wing, when at high angles of attack the indirect measurement of C_L departed from the direct force balance measurements. Therefore it is not only challenging to quantify the vortex flow properties but even, at lower angles of attack, the definition of vortex center is an ambiguous task.

Figure 4.1-6 presents the contours of $\zeta c/U_\infty$ and u/U_∞ for DW50 at $\alpha = 6^{o}$. It is to note that at the given angle of attack, breakdown already crossed the trailing-edge therefore only the upstream half of the wing is presented. It is observable that the axial vorticity contours, unlike the slender delta wing, are noticeably weaker and diffused over a larger span area. In addition, the primary vortex is accompanied by the wake-like axial flow because the close proximity of the vortex to wing surface anticipated the boundary layer and vortical flow

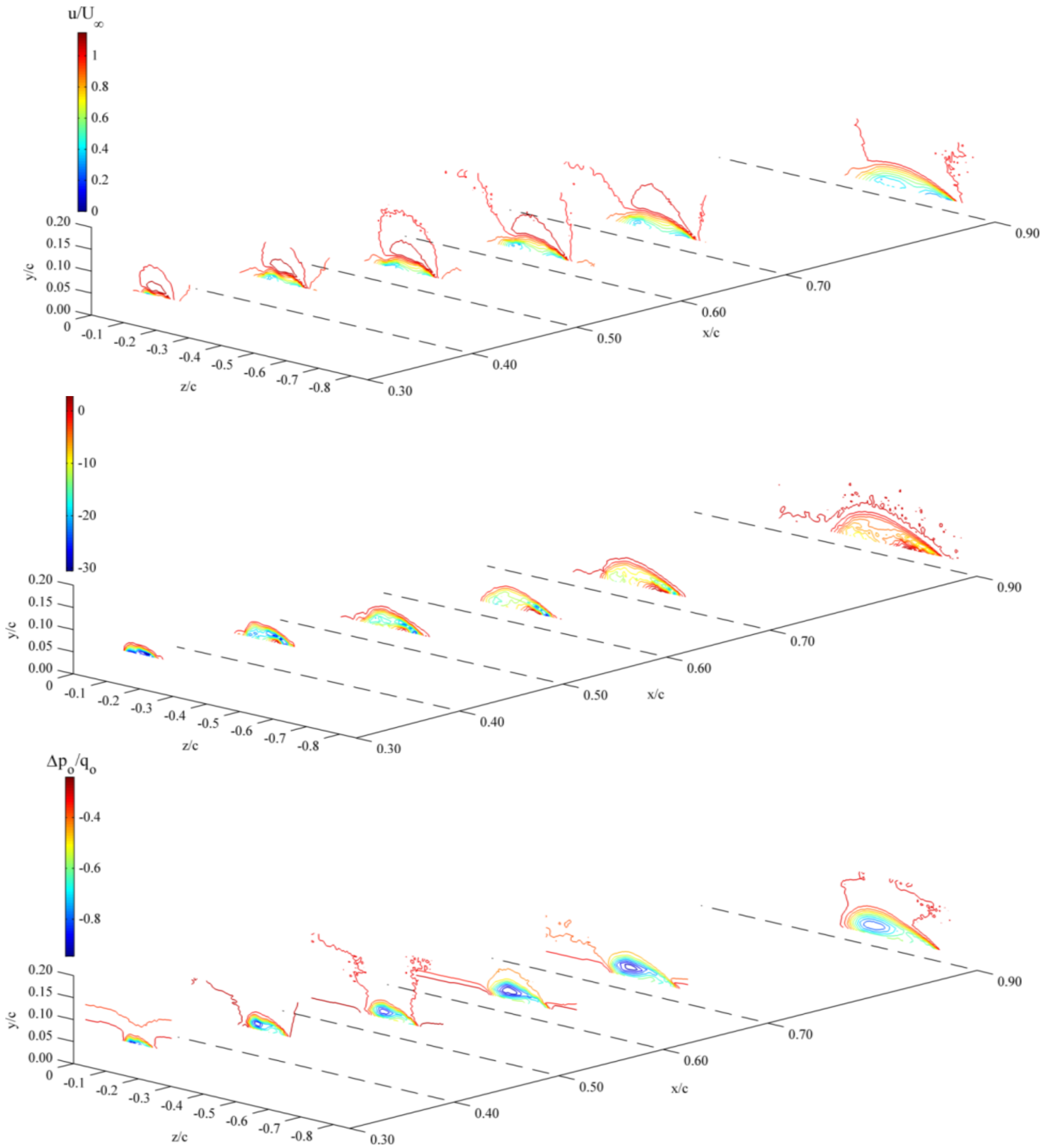

Figure 4.1-7 Streamwise variation of normalized axial vorticity, velocity and total pressure loss for DW65 at α = 6°

interaction which decapitated the core axial flow momentum. It is interesting to note that the presence of the jet-like flow is at the vortex outer limits where the desired acceleration is provided by the streamwise spiralling of the leading-edge vortex sheet. The streamwise evolution of the $\zeta c/U_\infty$, $u/U\infty$ and $\Delta p_o/q_o$ over the wing from (x/c 0.3 to 0.9) is shown in Figure 4.1-7. The haphazardness in flow is obvious at x/c = 0.9 due to the vortex breakdown. Unlike the slender counterpart, DW65, no viable information can be extracted from the present data whereas the pressure information is quantifiable. It shows that with downstream distance the spanwise expanse of the loss increases while the maximum core pressure loss remains constant, a similitude between the slender and non-slender delta wing. Figure 4.1-9 elucidates the variation of pressure loss across the pressure core in horizontal direction. It complements the aforementioned observation that the maximum pressure loss within the core remains constant. In addition, the pressure loss showed self-similar behaviour when plotted against the radial distribution scaled by local semi-span and the core width increases with downstream distance when plotted against the radial distribution scaled by wing chord.

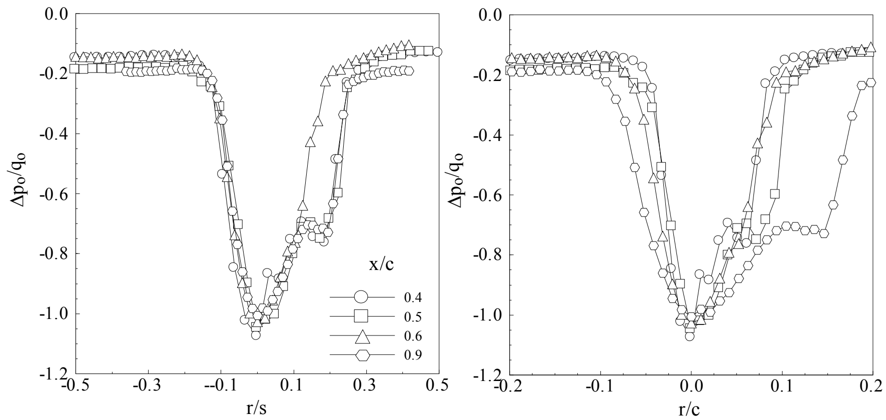

Figure 4.1-9 Streamwise variation of normalized total pressure loss about the pressure core for DW50 at α = 6°

The details of the vortex flow properties at upstream locations (x/c 0.3 to 0.6) for DW50 at an incidence of α = 6°, including the normalized axial velocity, axial vorticity and tangential velocity about the center, are shown in Figure 4.1-8. The abscissa is radial distance scaled by local semi-span. It was observed that the axial velocity gradually decreases with downstream distance and similar trend is followed by the local axial vorticity. From the present data it was inferred that the primary vortex does not show axisymmetric behaviour therefore the information is presented against the axial velocity core. Also it is to mention that, the identification of the vortex center based on the peak axial vorticity is impractical; firstly, as explained, the vortex is not well organized so no

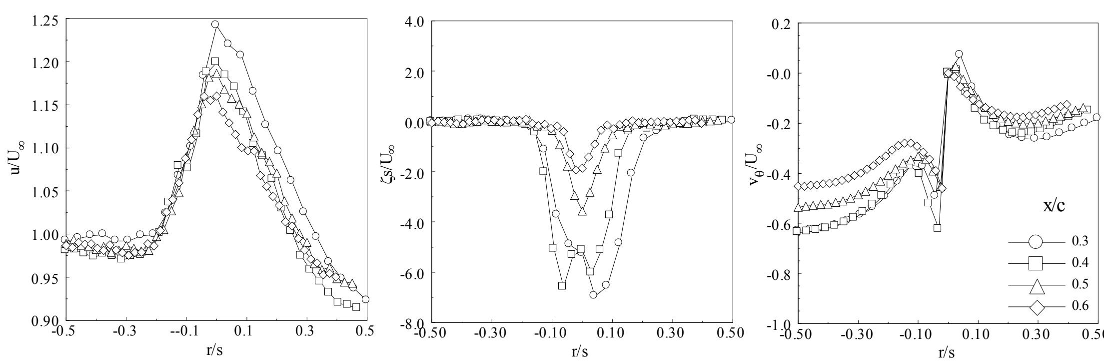

Figure 4.1-8 Streamwise variation of vortex flow quantities across the axial core, (from left) normalized maximum axial velocity, axial vorticity and tangential velocity

axisymmetry can be established and secondly, the derivative of cross flow velocities often result in multiple peaks of axial vorticity.

It has been known from flow visualization studies that a distinctive feature of DW50 is the dual vortex structure but their existence is limited to lower angles of attack and mostly confined to the upstream half of the wing because the energy content in outboard vortex is usually not enough to sustain the adverse gradient therefore it suffers early breakdown. Based on the PIV observation made by Taylor et al. [11], the existence of dual vortex is usually separated by a small layer of opposite sign vorticity and is highly sensitive to flow conditions. Figure 4.1-1 presents the vorticity contours for DW50 at x/c = 0.4 for $\alpha = 6^o$ and 8^o. It can be interpreted from the axial distribution that two comparable peaks existed in close proximity to each other whereas a small region of opposite sign vorticity also appeared at $\alpha = 8^o$. In present investigation the use of mechanical probe certainly incites the upstream conditions for even earlier breakdown. This distribution is also evident in Figure 4.1-8, where vorticity distribution at x/c = 0.4 showed multiple peaks close to each other. In addition the observation is only limited to small fraction of chord length as compared to one reported by Taylor et al [11].

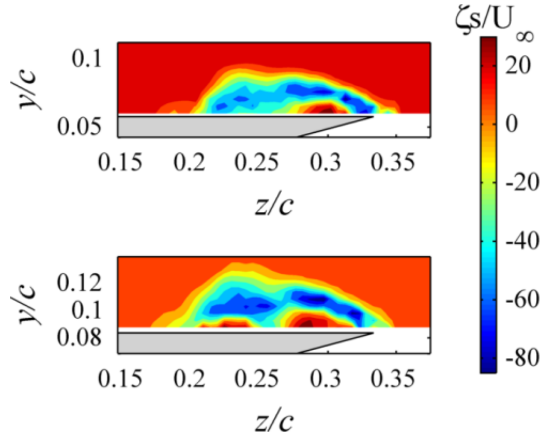

Figure 4.1-10 Existence of multiple peaks in normalized axial vorticity field over DW50 at x/c = 0.4 and $\alpha = 6^o$ & 8^o

4.2 Variation of vortex characteristics with angle of attack

Figure 4.2-3 illustrates the growth of leading-edge vortex over DW65 at chordwise station x/c = 0.4. Alongside the contours the corresponding maximum value is also presented. It shows that vortex continuously grew in strength with increasing angle of attack where the vorticity is scaled with respect to root wing chord. For $\alpha = 10^o$ to 22^o, the magnitude of $\zeta c/U_\infty$ increased and iso-contours became more closely spaced as feeding from leading-edge vortex sheet increases with increasing incidence. In contrary there is a minimal change in vorticity of secondary vortex. The composite plot of normalized axial flow contours for $\alpha = 10^o$ to 22^o is given in Figure 4.2-3. A gradual increase in peak axial velocity from $1.5U_\infty$ to $2.6U_\infty$ is witnessed with increase in angle of attack. The correpsonding increase in axial core is also observable. Further insight on variation in vortical flow can be developed by studying the behaviour of critical flow parameters.

The changes in flow structure with increasing wing incidence is illustrated in Figure 4.2-4, which shows, $\zeta c/U_\infty$, u/U_∞ and v_θ/U_∞ plotted against radial distance along a horizontal line through the vortex center at x/c = 0.4. The distribution of axial vorticity increases with increasing incidence whereas the spanwise extent of the core remained fairly insensitive to

α, indicative of vortex tightening. However the axial core expanded in size and the peak values are well above the free stream and reaching a maximum of $2.6U_\infty$ at $\alpha = 22^o$. Note that the secondary peak in vorticity distribution, indicative of vorticity confined by the shear layer, decreases with increasing incidence. This may be interpreted as decrease in vorticity feed or largely the slackening of balance created by generation and downstream convection of the vorticity. The asymmetric tangential velocity distribution showed high gradients about the vortex center and the discrepancy about the centerline and leading-edge side became significant with angle of attack. It is to note that regardless the size of vorticity and axial velocity core, the peak-to-peak tangential velocity is confined within ~3% of r/c or ~4% of the local semi-span. A minimal reduction in size is witnessed over the range of angles of attack which reflects that; on increasing the incidence the corresponding increase in vortex strength is accompanied by tightening of consecutive shear layers within the vortex core.

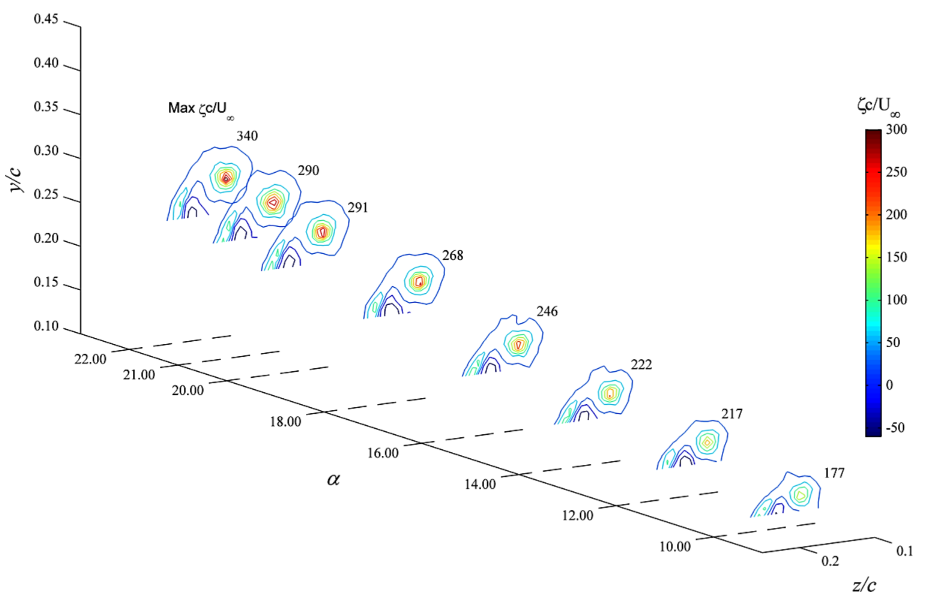

Figure 4.2-2 Variation of normalized axial vorticity iso-contours with angle of attack for DW65 at x/c = 0.4

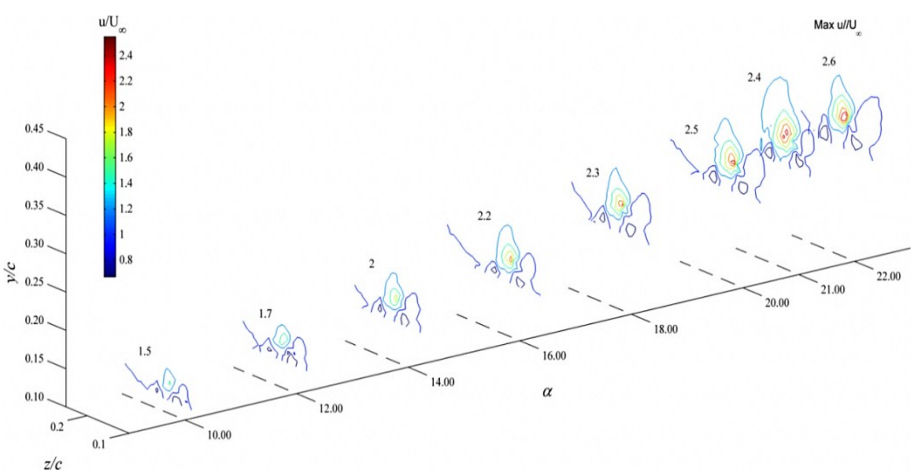

Figure 4.2-2 Variation of normalized axial velocity iso-contours with angle of attack for DW65 at x/c = 0.4

Figure 4.2-5 presents an overview of the variation of critical vortex flow parameters with angle of attack for DW65 at x/c = 0.4. From $\alpha = 10^o$ to 22^o the magnitude of axial vorticity, tangential velocity and maximum and core axial velocities increased linearly whereas a drop in core axial velocity and tangential velocity is reported for $\alpha = 22^o$, prior to the

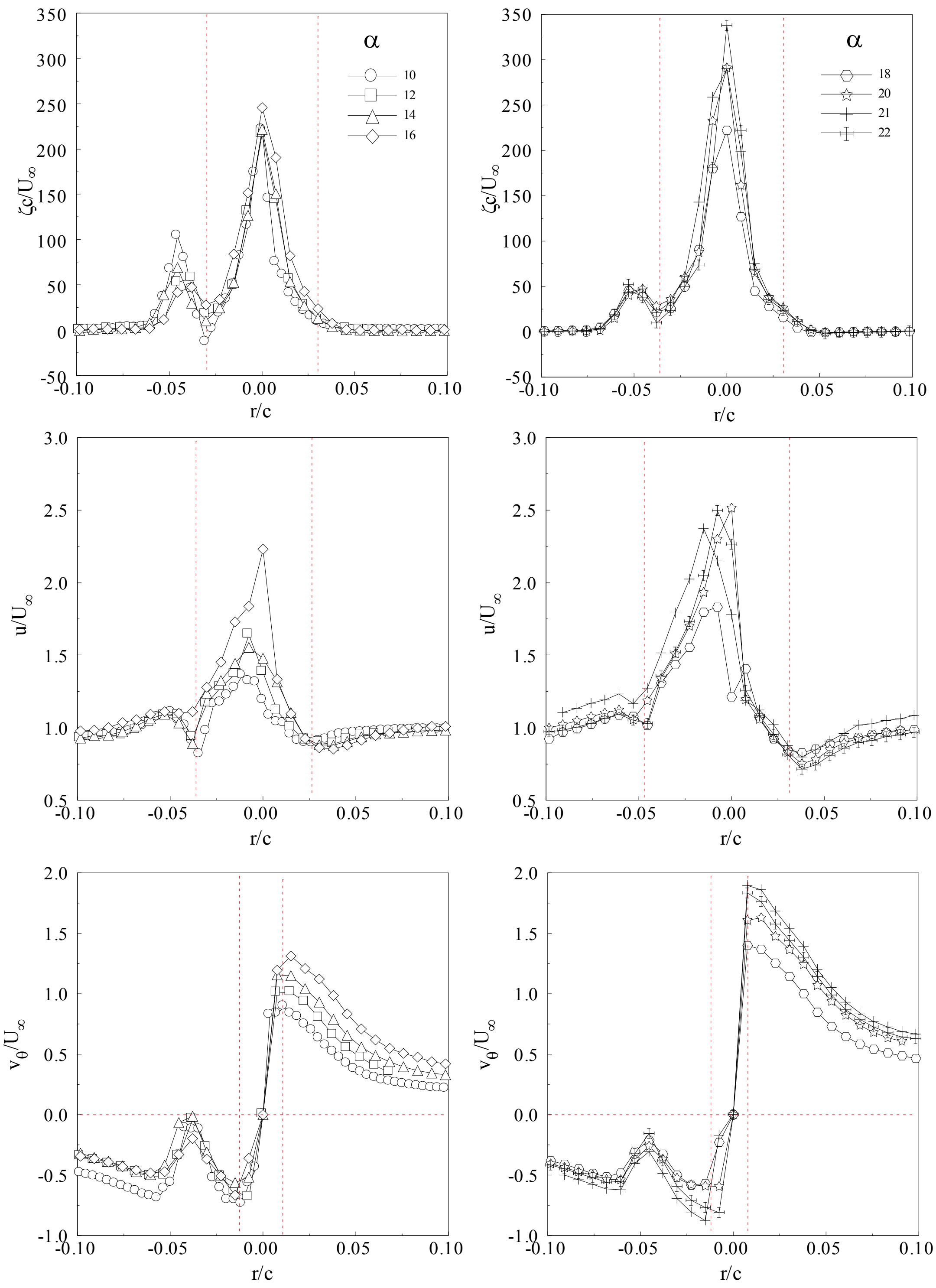

Figure 4.2-3 Variation of vortex flow quantities with angle of attack for DW65 at x/c = 0.4

breakdown reaching the measurement plane. This hints the instability and upstream proliferation of disturbance caused by the downstream presence of vortex breakdown. It is observable that for the intermediate angles of attack the location of vortex core[1] coincides with axial velocity core and resulted in axisymmetric vortex behaviour while a mismatch is

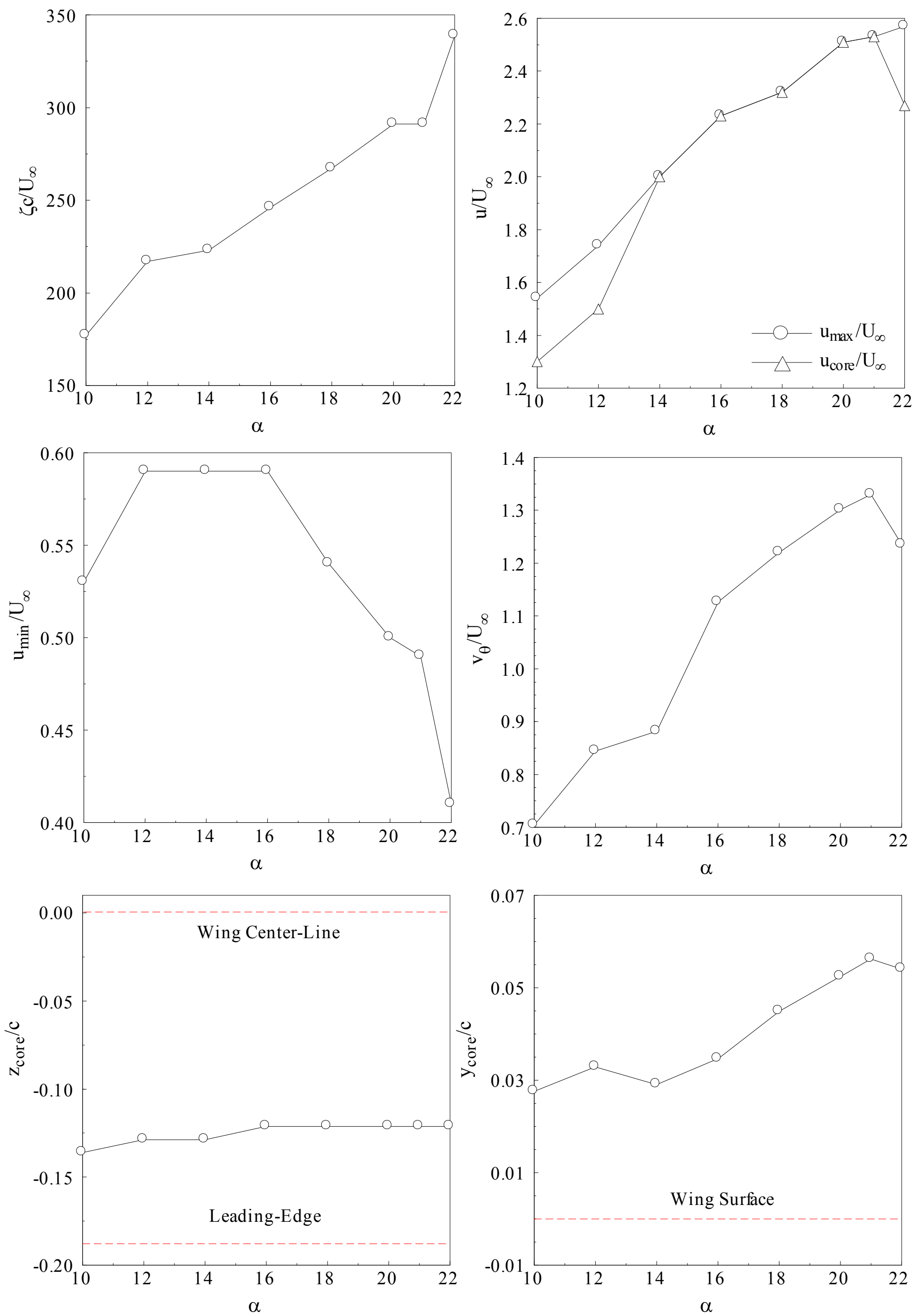

Figure 4.2-4 Variation of critical vortex flow parameters with angle of attack for DW65 at x/c 0.4

[1] Location of maximum vorticity, i.e. also the location of core axial velocity

observed at low and high angles of attack. The u_{min}/U_∞ remained fairly constant for $\alpha = 10^o$ to 16^o, beyond that it continuously decreases from $0.60U_\infty$ to $0.40U_\infty$. As discussed, the secondary vortex is characterized by the wake-like core axial flow which in present study remained constant up to $\alpha = 16^o$. The drop in magnitude of wake-like core axial velocity may reflect the breakdown of the secondary vortex which usually precedes the breaking down of primary vortex.

Lastly, the normalized vortex trajectory along the spanwise (z/c) and traverse axis (y/c) is also presented in Figure 4.2-5**.** Prior to the core axial velocity reaching twice the free

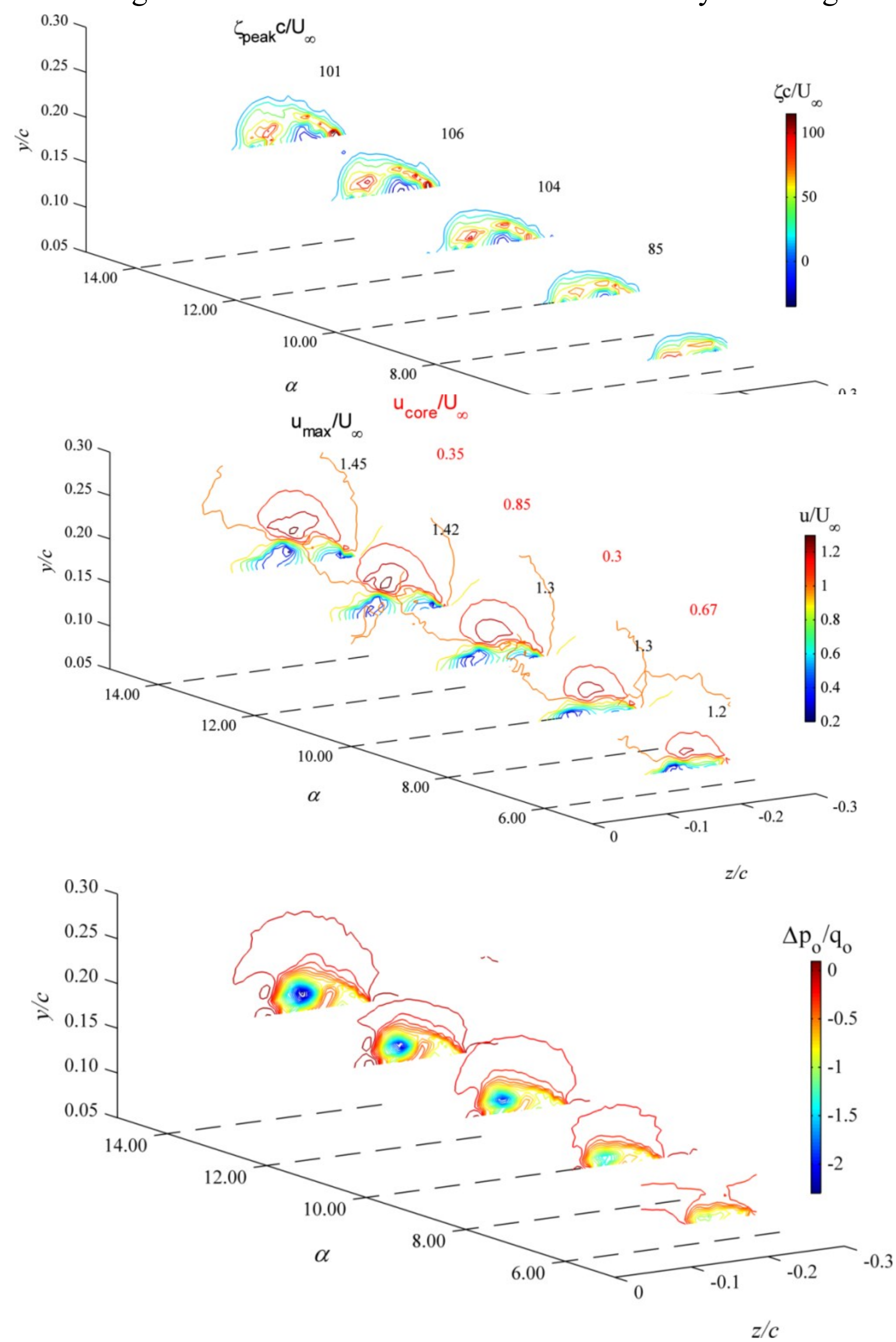

Figure 4.2-5 Variation of normalized axial vorticity, axial velocity and total pressure loss iso-contours with angle of attack for DW50 at x/c = 0.3

stream velocity, the vortex moved towards the wing centerline or away from the leading-edge. Afterwards, the distance of vortex center almost remained constant from the wing leading-edge until it suffered the ultimate fate of bursting. Conversely, after some initial fluctuations, at low angles of attack the vortex in traverse plane gradually moves away from the wing surface till it reached the incidence of 21°, from there onward it tended to maintain the same location up to the anticipated vortex breakdown around $\alpha = 23^o$.

In contrast to DW65, the flow structure over DW50 is not well organized especially at low angles of attack. The contours of constant axial vorticity, axial velocity, and constant total pressure loss are given in Figure 4.2-5 for x/c = 0.3 It is evident from the composite plot that at low angles of attack, especially for $\alpha = 6^o$ case, the vorticity in the flow is not enough for a distinctive leading-edge vortex and is confined within few probe distance from the wing surface whereas the peak axial velocity is close to 1.2U. On increasing incidence, at $\alpha = 8^o$, the flow started showing an observable concentration of vorticity with a secondary separation resulting in secondary vortex. Thereafter at high angles of attack the vortical flow resembles the flow over a slender delta wing due to increased distance from the wing surface but only in qualitative sense because among many difference one is the presence of wake-like axial velocity within the vortex centre. At $\alpha = 10^o$ and beyond, there existed a region of high vorticity concentration just inboard of secondary vortex which increases in strength and size with increasing incidence. Similarly, the secondary vortex also tended to follow the same pattern. It is to note that the organization of the flow is disturbed at $\alpha = 14^o$, indicative of onset or in close proximity of vortex breakdown. Noticeably the core velocities are always wake-like and never exceeded the free stream for the given angles of attack. Although the axial flow even reached a maximum of $1.45U_\infty$ at $\alpha = 14^o$ but away from the wing surface and vortex center. Interestingly, the contours of constant pressure loss revealed that; despite the asymmetry in axial velocity distribution the pressure loss across the vortical flow is symmetric and increases with increasing angle of attack. Since the total pressure is the combination of static pressure plus the dynamic component from all three velocity vectors therefore regardless of the flow structure the absolute velocity breakdown strictly respects the symmetry of pressure distribution.

Figure 4.2-7 illustrates the variations of vortex quantities with radial distance along a horizontal line passing through vortex center. Note that, as already discussed, the vortical flow is highly asymmetric over DW50 and neither the axial velocity nor the total pressure loss core centers coincide with the vortex core center. It is apparent that for higher angles of attack the multiple peaks are markedly separated by a region of zero vorticity while in the case of $\alpha = 8^o$, the $\zeta c/U_\infty$ is distributed over the span, indicating the absence of any distinctive vortex and was only a spread of shear layer vorticity. Moreover, the corresponding peak outboard of the primary vorticity peak is associated with the vorticity confined by the feeding leading-edge sheet. Once developed, the $\zeta_{peak}c/U_\infty$ remained fairly constant over the range of angles of attack and so do the extent of vortex core. Similar to

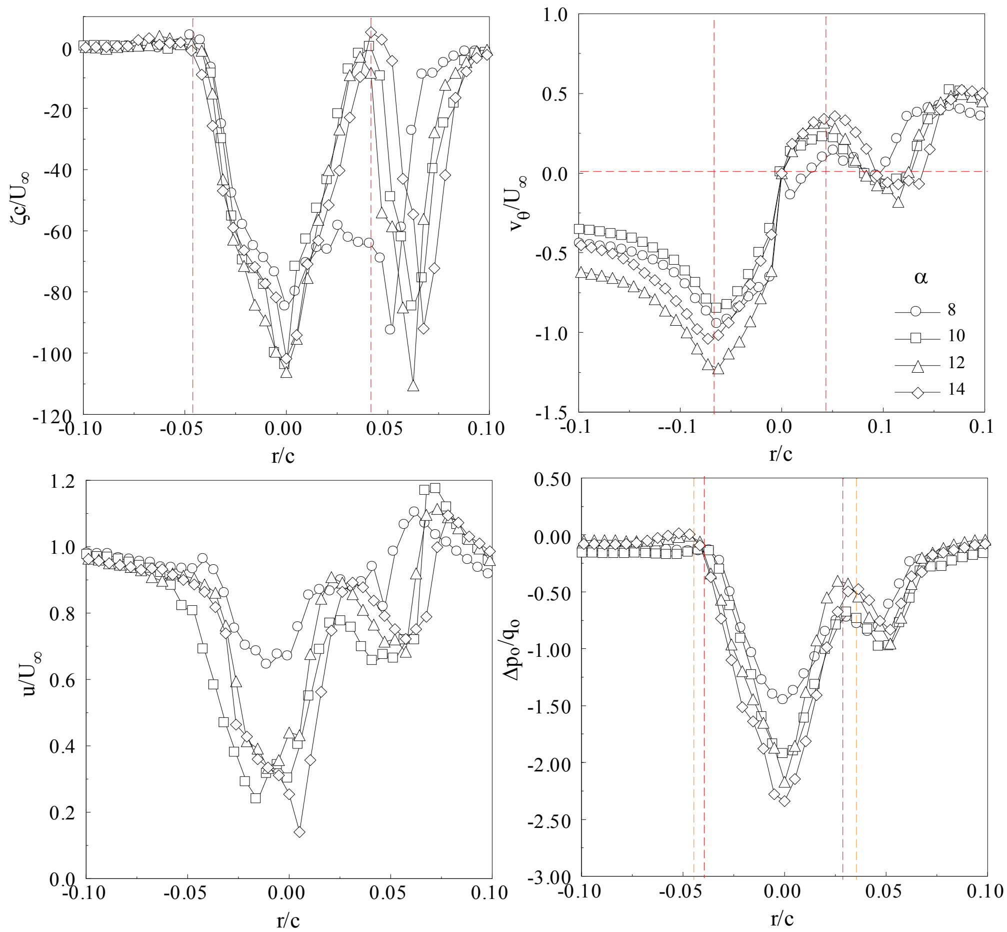

Figure 4.2-6 Variation of vortex flow quantities across the vortex center with angle of attack forDW50 at x/c = 0.3

DW65, the variation of tangential velocity showed asymmetry about the vortex center. The difference in peak tangential velocity is suggestive of vortex development over the wing and it increases with increasing angle of attack except for α = 14°. This discrepancy is by virtue of vortex diffusion induced by the downstream presence of vortex breakdown which is supported by the increase in spanwise extent of total pressure loss at α = 14°. At all angle of attacks, the islands of axial velocity excess and deficit were distinctively evident, and expectedly the axial velocity about the vortex center is wake-like and the related momentum deficit increases with increasing incidence.

4.3 Wake vortex evolution

Wake vortex evolution is studied to quantify the effects of leading-edge vortices on bodies just downstream of the wing. Among the prospective applications is to develop an understanding of the alleviation of wake vortices left behind by the arriving and departing airplanes which limit the capacity of the busiest airports and poses serious accidental hazards to smaller preceding aircraft. Moreover the detailed insight on wake evolution can help improve the safety of formation flights, air refuelling and extend the limits of air combat manoeuvres. Note that the elucidation of wake vortex development can only be of interest prior to the breakdown reaching the trailing-edge because the upstream occurrence of vortex breakdown induces high order of disorganization in the wake vortex flow.

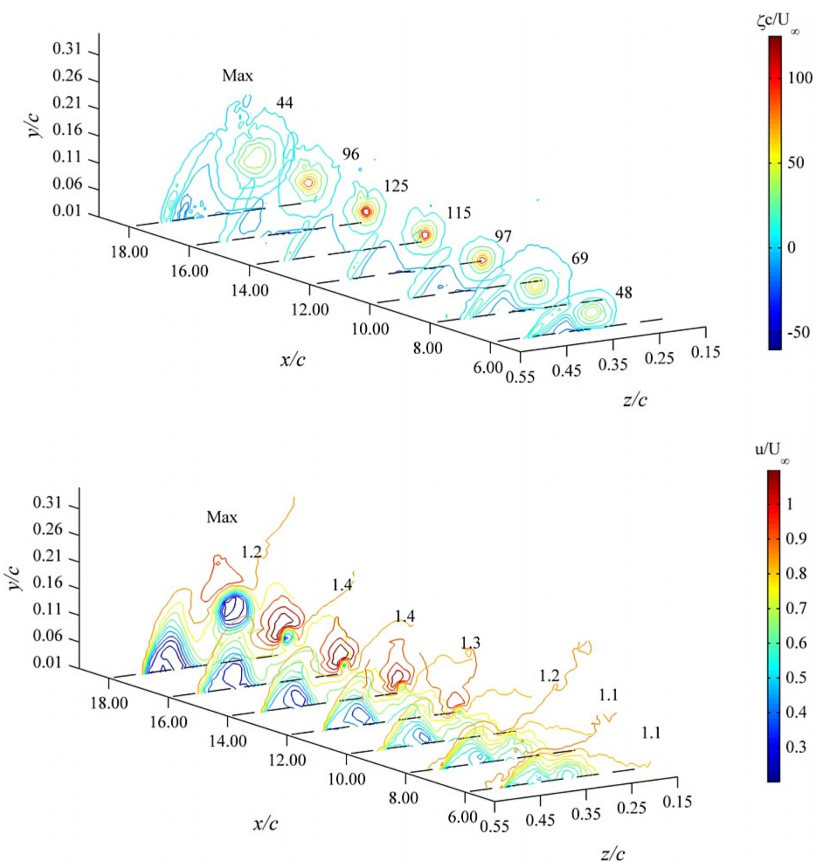

Figure 4.3-1 Variation of normalized axial vorticity and velocity with angle of attack for DW65 at x/c = 1.02

The variation of $\zeta c/U_\infty$, v_θ/U_∞ and u_{core}/U_∞ with radial distance scaled by root wing chord along a horizontal line passing through the vortex center is presented in Figure 4.3-2 for near-wake (x/c = 1.02) of DW65. With increasing incidence the size of vortex core gradually increases where at maximum it is ~0.2 r/c or ~20% of the semi-span. It is noticeable from the tangential velocity plot that the size of the core is almost insensitive to change in angle of attack whereas it witnessed a considerable variation in magnitude. Since the vortex is still developing and entraining the shear layer vorticity the asymmetric distribution is observable but the distribution is reverse, where the peak tangential velocity was greater on the leading-edge side and smaller on the centerline side. The absence of wing surface and disconnection of vorticity feed might be the reasons responsible for this shift in asymmetry. It is to note that symmetric distribution is only witnessed for $\alpha = 8^o$. Similarly the core axial velocity is plotted against the radial distance and showed that with increasing angle of attack the magnitude of peak axial velocity increases but in the meanwhile there appeared a region of large momentum deficit. A close inspection revealed that actually two observable regions of momentum deficit is along the vortex core line; the one towards the wing tip is the wake-like flow representative of secondary vortex whereas the one towards the wing centerline is an island of axial flow deficit appeared in primary vortex. It is to mention that the latter appeared due to the instability caused by the onset of vortex breakdown and the drifting of secondary vortex closer to the primary vortex is responsible for the former. The overall behaviour can be understood by visualizing the

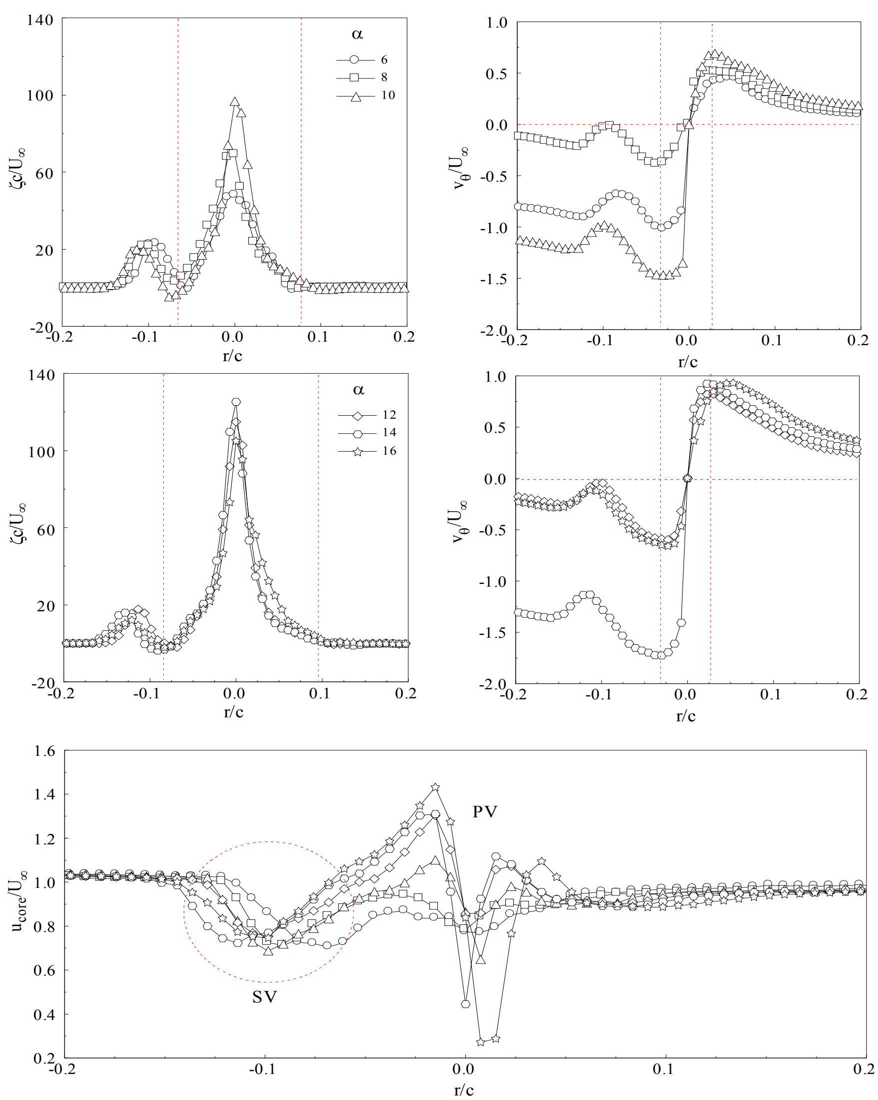

Figure 4.3-2 Variation of vortex flow quantities with angle of attack in wake of DW65 at x/c = 1.02 with angle of attack

combo axial vorticity and velocity contour plots for the range of angles of attack investigated, given in Figure 4.3-1**.** The aforementioned momentum deficit is visible in axial velocity contours alongside the observable diffusion of vorticity contours at $\alpha = 16^o$

Figure 4.3-3 presents an overview of the variation of the critical vortex flow quantities with increasing angle of attack just aft the trailing-edge at x/c = 1.02. It is to observe that normalized axial vorticity, tangential and axial velocities followed the similar trend as of x/c = 0.4. However the core and minimum axial velocity remained fairly constant at ~$0.85U_\infty$ and ~$0.25U_\infty$ respectively. Figure 4.3-3 (e, f) shows the vortex trajectory along the spanwise and traverse axis. With increasing incidence a minimal movement in spanwise direction whereas an observable movement away from the trailing-edge was recorded at the given downstream station.

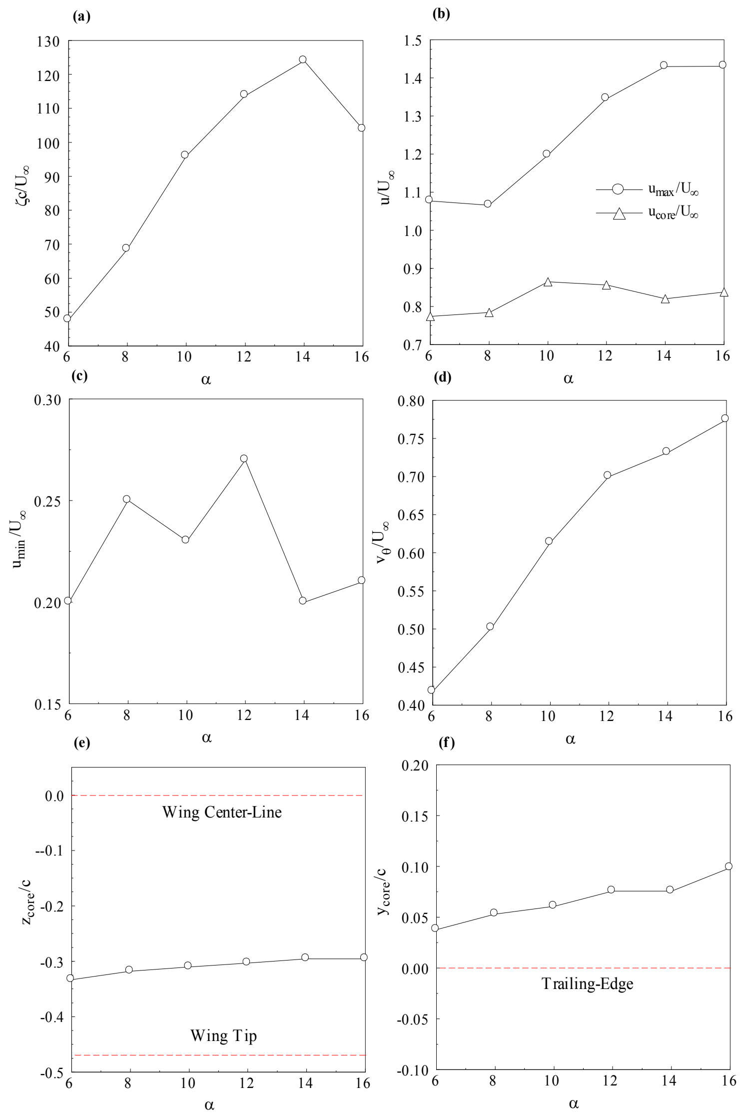

Figure 4.3-3 Variation of critical vortex flow parameters with angle of attack in wake of DW65 at x/c = 1.02 with angle of attack

The streamwise evolution (x/c = 1.02, 1.04, 1.28, 1.40 and 2.0) of the wake generated by the DW65 at $\alpha = 16^o$ is illustrated in Figure 4.3-4 which shows the field of axial vorticity along with axial velocity. Just downstream of the trailing-edge the vorticity fields were dominated by positive concentrations in primary vortex and separated leading-edge sheet while an opposite concentrations in wing wake and secondary vortex. Unlike the trailing tip vortices, within a chord distance all the scattered vorticity merged into a single diffused vortex. In vicinity of the trailing-edge (x/c 1.02 to 1.04) the secondary vortex and wake merged together and resulted in an observable region of opposite sign vorticity which also affected the formation of primary vortex. Further downstream from x/c = 1.04 to 1.28 the primary vortex somehow retained the shape and concentration whereas the secondary concentration moved upwards and closer to the primary vortex under the action induced by the strong tangential flow and by the remainder of the wake. Eventually the interaction between the primary and secondary vortices resulted in a complete coalescing of the contrasting field which culminated in a weaker rotational flow of about half the computed peak vorticity at x/c = 1.02.

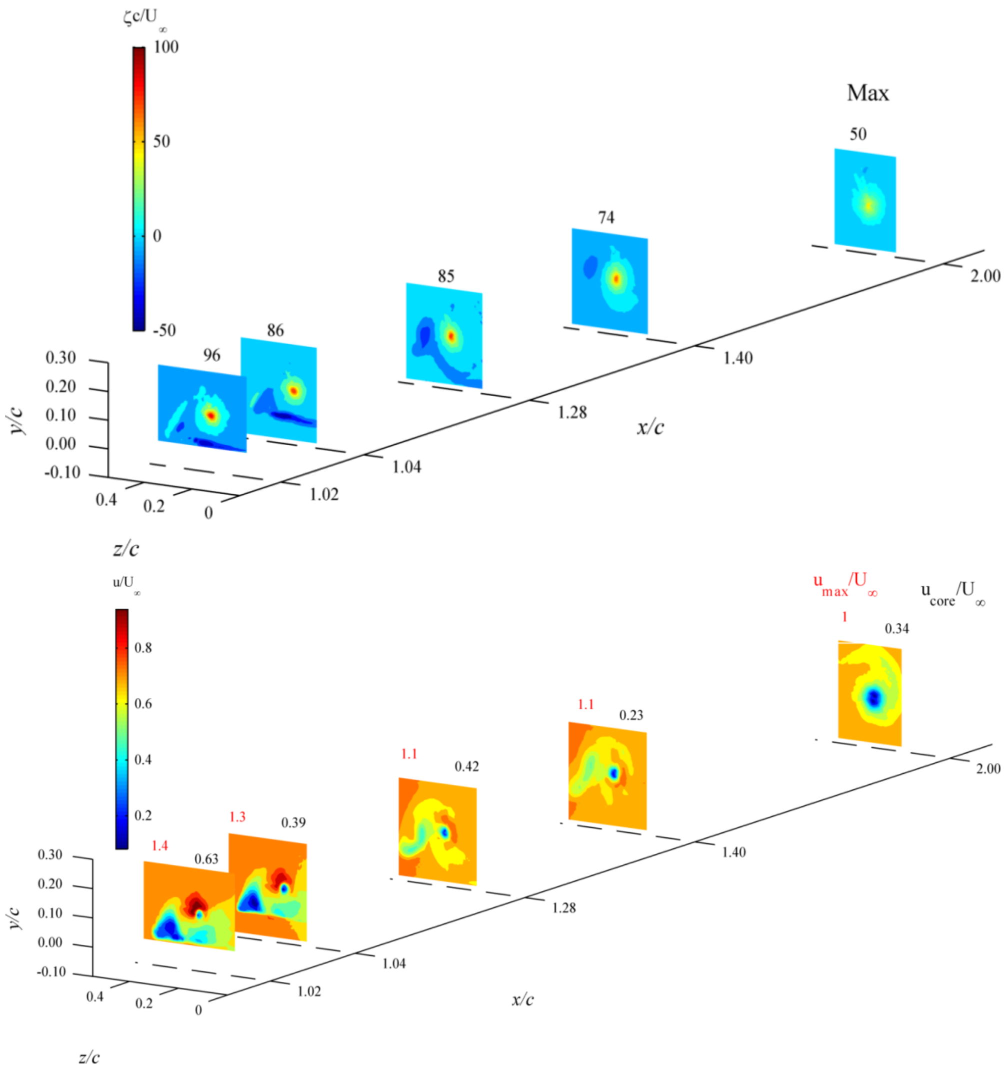

Figure 4.3-4 Streamwise variation of the normalized axial vorticity and velocity field in wake of DW65 at α = 16º

It is mentioned that at α = 16º, the breakdown is in the vicinity of the trailing-edge therefore on leaving the wing surface a patch of wake-like flow appeared in the vortex core center. This rapid deceleration of axial core from ~1.3U∞ to ~0.6U∞ drifted the surrounding jet flow away from the vortex center. Moreover in the absence of any commendable streamwise gradient the energy from the remainder of the jet flow was seized within half a chord distance (x/c = 1.4) and the aforementioned axial flow deficit totally encompassed the vortex core region. At x/c = 2.0, this region of momentum deficit grew in size and filled the entire vortex cross section where axial flow velocity dropped to a minimum of ~$0.1U_\infty$.

The presence of vorticity concentration in secondary vortex and the corresponding entrainment of wake aggravate the level of intricacy therefore to develop further insight into the development of off the wing vortical flow the contours of normalized crossflow velocity are presented in Figure 4.3-5.

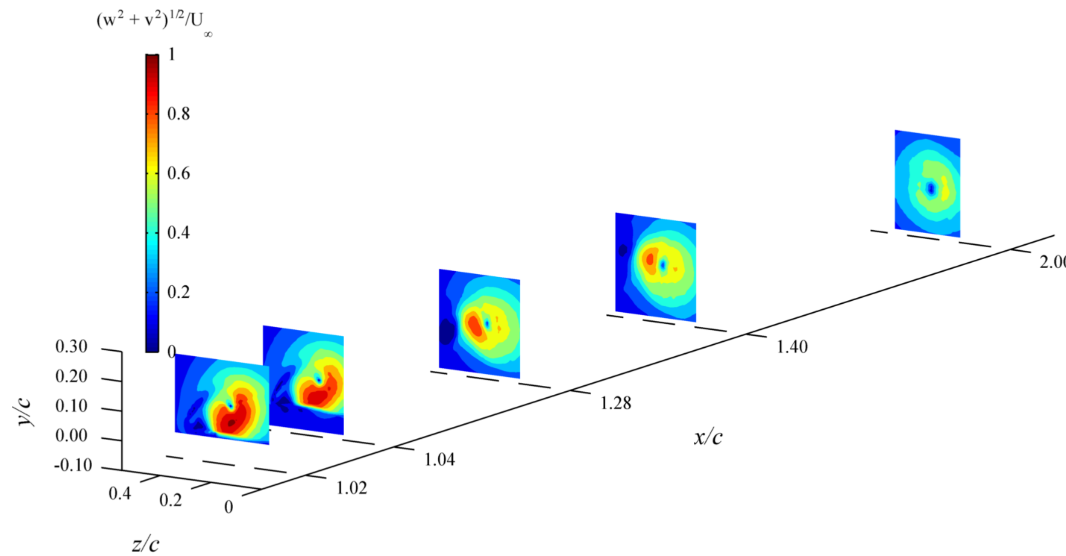

Figure 4.3-5 Streamwise variation of normalized cross flow velocity field in wake of DW65 at α = 16°

The changes in flow structure aft the trailing-edge with increasing downstream stream are illustrated in Figure 4.3-6 which shows $\zeta c/U_\infty$, v_θ/U_∞ and u_{core}/U_∞ plotted against the radial distance along a horizontal line through the presumed vortex center[1]. The peak axial vorticity suffered a gradual drop over the downstream distance (Figure 4.3-7) but interestingly the extent of the vorticity concentrations remained fairly constant over the entire region. It is noted that at x/c = 1.28, a region of opposite sign vorticity appeared alongside the primary concentration, suggesting the presence of secondary vortex and entrained wake along the horizontal plane of the primary vortex. Just aft of trailing-edge the asymmetric distribution in tangential velocity is quite significant and occurred at centerline side of the vortex, indicating the entrainment of shear layer vorticity then with downstream distance the difference in absolute peak decreases and finally it fluctuates within a range of ±15% between the centerline and wing tip side. In agreement with vorticity diffusion, the absolute peak tangential velocity also dropped with increasing distance. The axial velocity along the horizontal axis through the vortex center reported opposing regions of jet-like and wake-like flow. As already discussed the instability along the vortex axis and the ensuing

[1] The vortex is assumed to be broken down but the post breakdown symmetric distribution determines the vortex center

breakdown decelerated the core flow which in later stages dominated the entire vortex cross section. Note that, off the wing, except the wind tunnel buoyancy effects, it is the streamwise deceleration and diffusion of tangential velocity which offered an adverse gradient to the already broken down axial flow. This accelerated the deceleration of core and concluded in large momentum deficit within the vortical region.

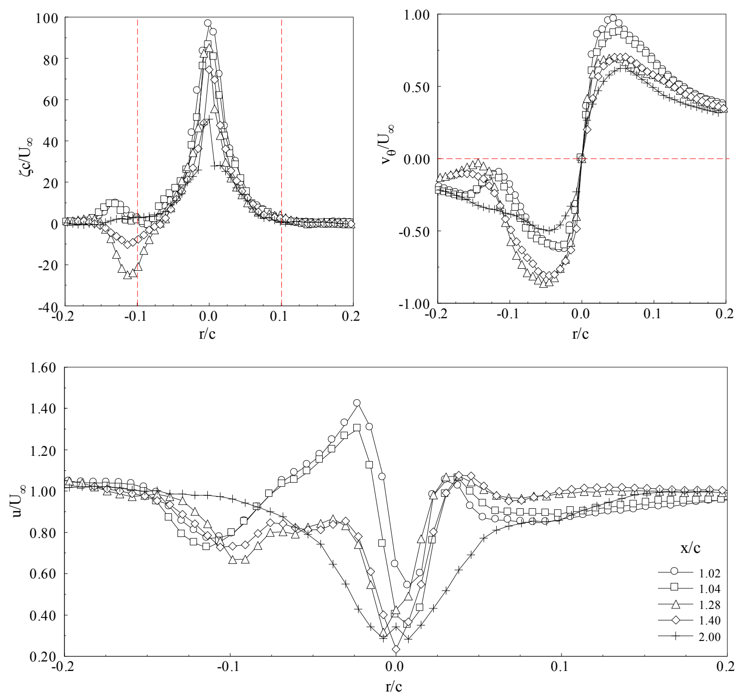

Figure 4.3-6 Streamwise variation of vortex flow quantities across the vortex center for DW65 at α16°

An overview of the variation of the critical vortex quantities with downstream distance is given in Figure 4.3-7. The core axial velocity is reported for the presumed vortex center and suffered steep dropped just aft of trailing-edge, indicative of ongoing process of vortex breakdown which is joined by the comparable drop in axial vorticity. The drop in absolute maximum tangential velocity about a vortex center is almost linear whereas the variation of differential in peak tangential velocities provided further insight on the development of vortical flow. From x/c 1.02 to 1.04, the difference of ~50% is reduced by mutual momentum loss in both sides, indicative of viscous diffusion anticipated by vortex breakdown. From x/c = 1.04 to 1.28, the absolute peak of tangential velocity now occurred on the wing tip side of the vortex center. This switch in velocity differential was probable only in absence of feeding vorticity sheet. Eventually the close proximity of opposing flow extenuated the large tangential velocity and concluded in nearly-symmetric crossflow velocities ~$0.5U_\infty$ at x/c = 2.0.

Once the primary vortex is deprived of continuous vorticity feed, the computation of outer and inner vortex parameters can now be evaluated with ease. Just aft the trailing-edge, the ongoing process of vortex breakdown resulted in ~42% increase in vortex outer radius

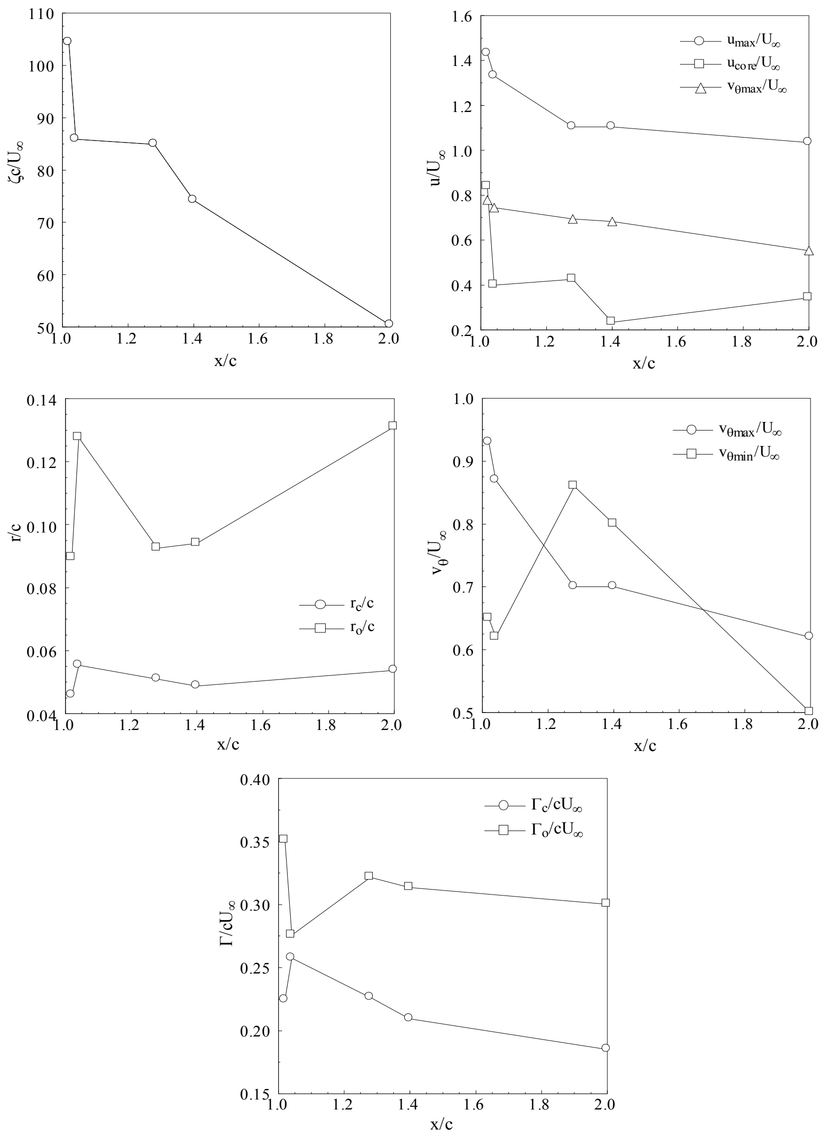

Figure 4.3-7 Streamwise variation of the critical vortex parameters in wake of DW65 at α = 16°

(r_o/c) and ~22% decrease in normalized vortex strength (Γ_o/cU_∞). Further downstream, from x/c = 1.04 to 1.28, a significant decrease of ~27% in outer radius occurred along with an increase in outer circulation, indicative of vorticity entrainment complemented by the tightening of spiralling shear layer. Accordingly the core radius also decreased by ~7% and despite the diffusion of vorticity in the vortex core, the preceding phenomena of flow entrainment and tightening of shear layers helped vortex in sustaining the same vorticity peak. This can be interpreted as the reorganization of the broken down vortex. It is interesting to note that the ratio Γ_c/Γ_o had value of approximately 70.5%, which was similar to the theoretical value of 71.5% for a fully developed laminar vortex. Then from x/c = 1.28 to 1.40, the outer radius remained fairly constant but the corresponding decrease in vortex strength reflected the adverse interaction between the contrasting flows. It is to note that, even though majority of the evolution was taking place in the outer region but the relative drop in core circulation highlighted the activity within the vortex core. At one chord distance downstream of the trailing-edge a rapid drop in core vorticity was accompanied by a drastic increase in outer radius, indicative of substantial turbulent and viscous diffusion. Unlike the trailing tip vortices, at the selected incidence, the leading-edge vortices suffered early breakdown followed by a phase of reorganization which eventually ended up in a pair of highly disorganized weak vortical structure characterized by large momentum core deficit. The high tangential velocities and the associated streamwise deficit are responsible for the early breakdown of the leading-edge vortices.

Figure 4.3-8 presents the filled contours of axial vorticity and axial velocity for 6° and x/c = 1.02, 1.10 and 1.50 for DW50 at α = 6°. It is already mentioned that in the case of non-

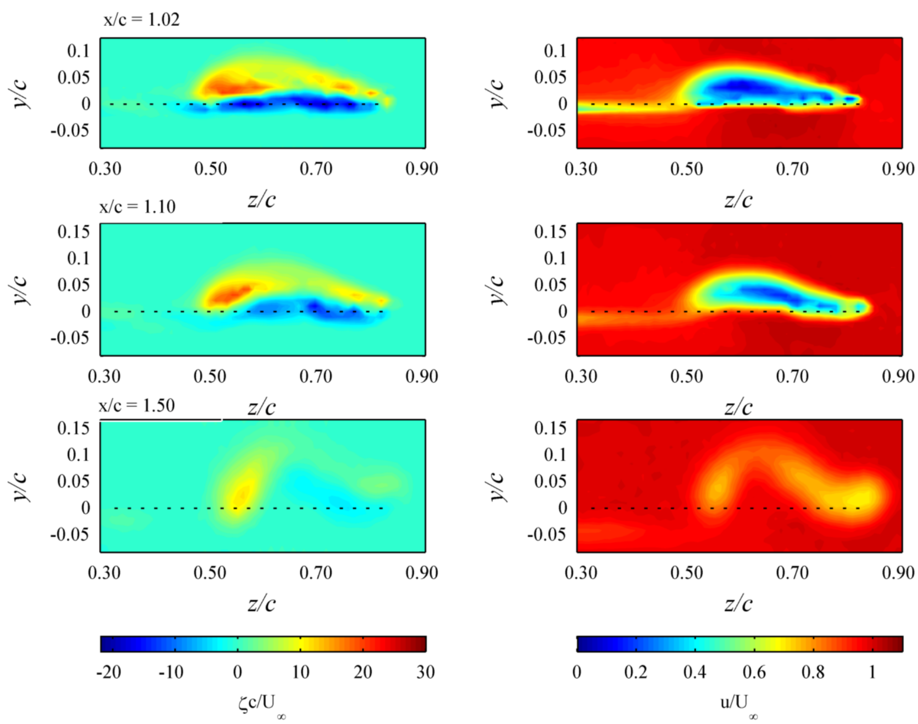

Figure 4.3-8 Planar representation of streamwise variation of normalized axial vorticity and axial velocity fields in wake of DW50 at α = 6°

slender delta wings the onset of vortex breakdown reaching the trailing-edge usually occurs at very low angles of attack therefore measurements made just aft of trailing-edge, unlike DW65, are corrupted by the disorganization of vortical flow. At x/c = 1.02, the vorticity confined by the primary vortex and wake vorticity spanned ~0.35 z/c or ~50% of the semi-span, indicative of vortex diffusion. The corresponding axial flow is understandably wake-like and from the spread of momentum deficit it can be established that vortex suffered the breakdown somewhere upstream of the measurement plane. On leaving the wing surface, the vorticity segregates into two distinct concentrations; separated by a region of weak opposite sign vorticity. Finally at x/c = 1.50, the vorticity is further diffused to ~1/2 of the preceding peak values and minimum of axial velocity recovers to $\sim 0.7U_\infty$.

Figure 4.3-9 presents the evolution of wake flow with angle of attack, measurements were made at x/c = 1.10 for selected incidences. As expected the vortical flow is deprived of any distinct vortex center and characterized by large momentum deficit due to vortex breakdown but the absolute vorticity increases with incidence. Similar trend was followed by the size of the vortical flow.

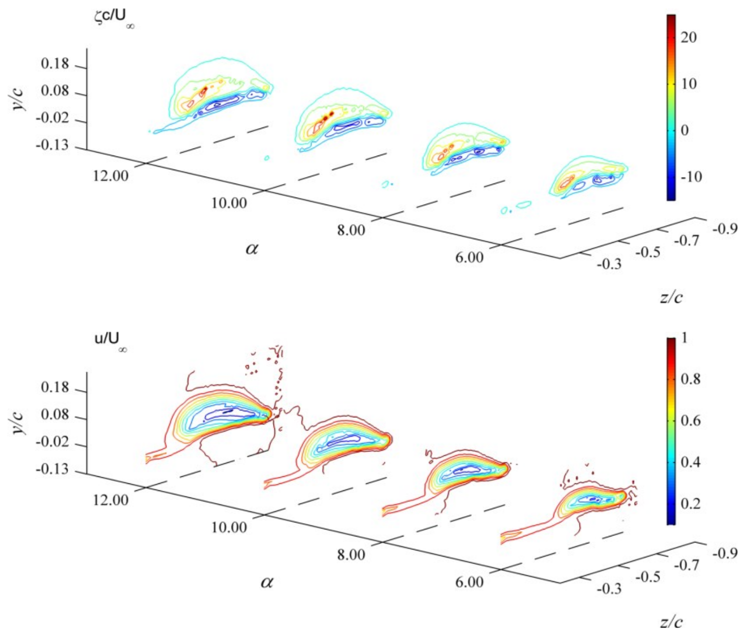

Figure 4.3-9 Variation of normalized axial vorticity and axial velocity with angle of attack for DW50 at x/c = 1.10

Lastly, the qualitative and quantitative illustration of variation in vortical flow with incidence at x/c = 1.50 is given in Figure 4.3-10. It is to mention that measurements at such distance aft of the trailing-edge are often imperious in comparative studies of non-slender delta wings. At $\alpha = 6^o$, the constant absolute cross flow velocity contours revealed an observable rotational flow about a distinctive vortex center this can be inferred as a confirmation of upstream presence of the coherent vortical structure. Figure 4.3-10 (bottom) shows the comparison of the $\zeta c/U_\infty$, u/U_∞, and v_θ/U_∞, it is interesting to note that a region of opposite sign vorticity, secondary vortex and wake entrainment, is visible in the case of $\alpha = 6^o$ whereas a noticeable increase in extent of vorticity spread is also witnessed. In the case of $\alpha = 6^o$, the horizontal variation of axial flow highlighted the presence of two distinct wake-like vortex cores, i.e. a primary vortex and an outboard amalgamation of same sign feeding layer vorticity. Similarly, the distribution and spread of the tangential velocity core[1] reported a higher absolute maximum, asymmetric distribution and a tighter confinement of rolled up shear layer within the vortex core for $\alpha = 6^o$.

[1] Horizontal distance between two consecutive absolute maxima

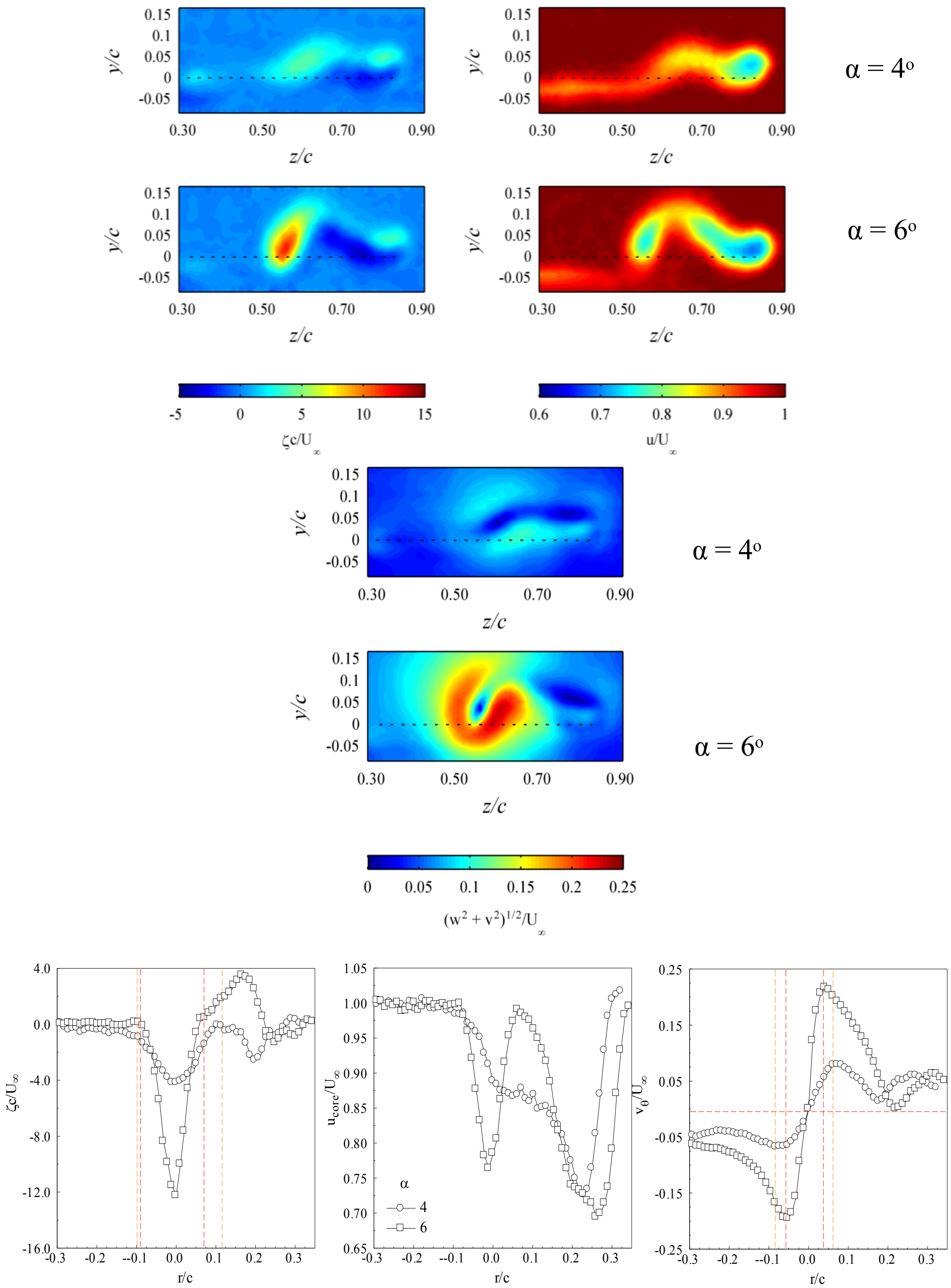

Figure 4.3-10 (Top) Planar representation of variation of normalized axial vorticity, axial velocity and cross-flow velocity for DW50 at x/c = 1.50 and α = 4° & 6°, (Bottom) Variation of vortex flow quantities (from left) normalized axial vorticity, axial velocity and tangential velocity about the vortex center with angle of attack for DW50 at x/c = 1.50

4.4 Vortex breakdown

From literature survey it was learnt that early works in reporting of vortex breakdown locations were limited to flow visualization. Although it is an invaluable tool which provides a description of flow characteristics but the output is more qualitative therefore it is equally important to conduct quantitative measurements in order to document a deeper understanding of flow structure. In view of this observation, measurements were made for a range of angles of attack to capture the vortex breakdown location.

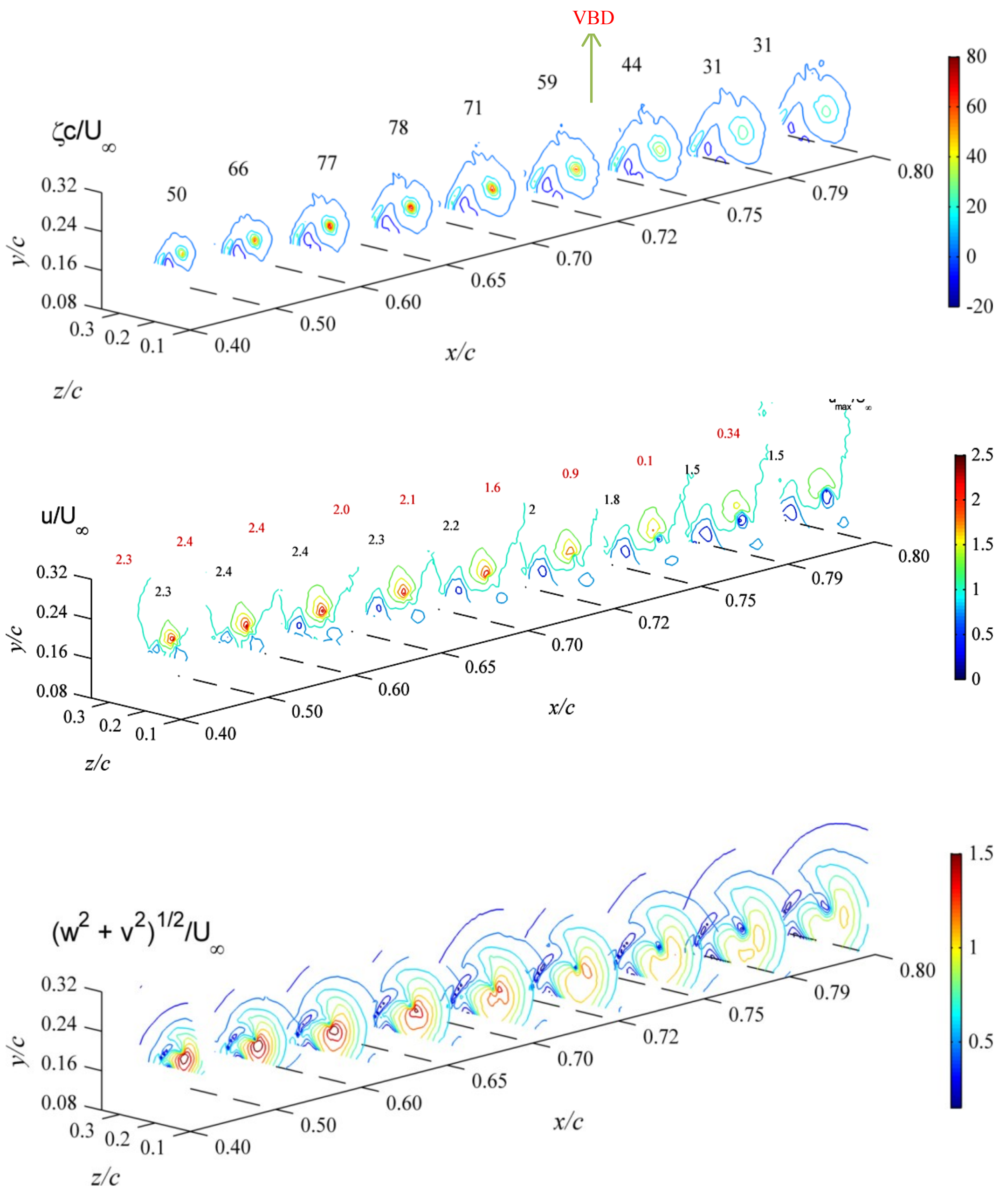

Figure 4.4-1 Streamwise variation of normalized axial vorticity, axial velocity and cross-flow velocity for DW65 at α = 18°

Figure 4.4-1 shows a composite plot of the contours of constant $\zeta s/U_\infty$, u/U_∞, and $(w^2 + v^2)/U_\infty$ over a DW65 at an incidence of 18°. Note that the axial vorticity is non-dimensionalized by local semi-span because it compensates for the streamwise variation in local wing geometry and highlights the breakdown effects. It tended to increase with downstream distance until unless it came in vicinity of vortex breakdown. Recall that, vortex breakdown location can be defined on different bases; either by a rapid drop in core axial velocity or by vorticity diffusion. The exact determination of breakdown location is not possible because the process is accompanied by large degree of unsteadiness and furthermore the downstream presence of the probe also affected the upstream flow condition. Despite the challenges, the flow information is quite revealing and therefore the axial and cross flow velocities are studied alongside the vorticity contours.

A sudden drop in axial vorticity is sighted at x/c = 0.725 and correspondingly there witnessed a proportional decrease in maximum axial velocity whereas in contrast to

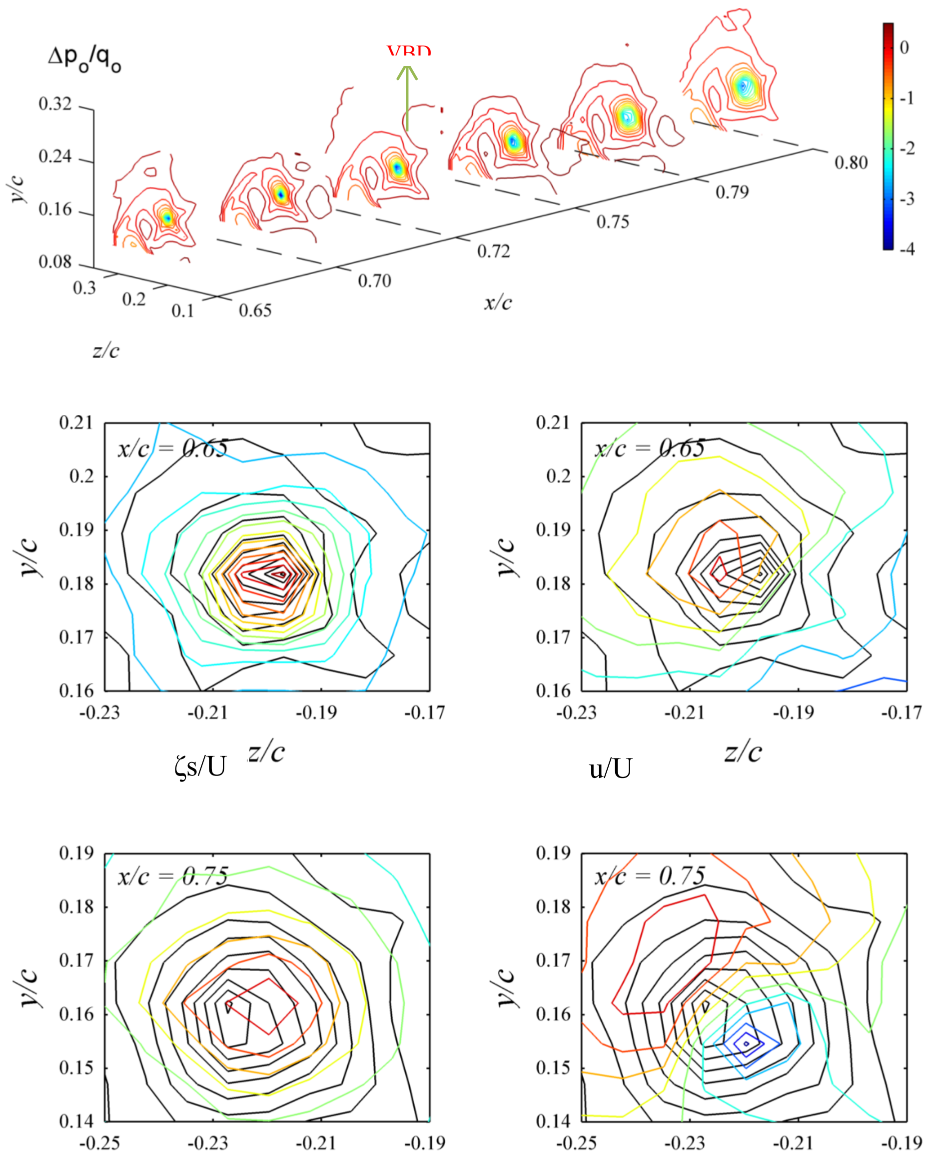

Figure 4.4-2 (top) Streamwise variation of normalized total pressure loss for DW65 at α = 16°, (bottom) Comparison of normalized axial vorticity & velocity and total pressure loss iso-

maximum axial velocity, the core axial velocity suffered a much steeper drop in streamwise direction on reaching within ~10%c (x/c = 0.65) upstream of anticipated breakdown. It is learnt that regardless the type of breakdown, the core is always the primary victim of breakdown induced disturbances. Interestingly, the clean distribution of cross flow velocity also showed a sign of discomposure at around x/c = 0.7. Further downstream, a brisk change in core axial velocity is observed when it went from being jet-like (~ $1.6U_\infty$) to wake-like ($0.9\ U_\infty$) at x/c = 0.75. Similarly a significant diffusion of axial vorticity and cross flow velocity was also reported at the same chordwise location. Note that on breakdown, there appeared an island of wake-like axial flow along the vortex axis which drifted the jet-like flow away from the vortex center. This patch of wake-like flow grew in size and suffered an implausible deceleration within ~2%c to about a stagnant point ~$0.1U_\infty$. From there onwards the vortical flow, in absence of its coherence but in presence of vorticity feed, continued the downstream journey until it leaves the wing surface. The discussion on critical vortex parameters will elucidate the consequence of continuous vorticity feed.

Figure 4.4-2 (top) presents the streamwise evolution of the normalized iso-contours of total pressure loss. It is evident that the maximum pressure loss remained fairly constant in close proximity to the vortex breakdown while in post breakdown region, the extent of total pressure loss increases with downstream distance. In contrast to axial velocity where the breakdown related retardation is characteristically asymmetric, the total-pressure loss showed symmetry even downstream of breakdown. Figure 4.4-2 (bottom) presents a comparison of axial vorticity and velocity with total-pressure loss in vicinity of breakdown. It is to note that upstream of vortex breakdown (x/c = 0.725), i.e. x/c = 0.65, the axial vorticity and velocity contours are coincident with total pressure loss contours. On the other hand, downstream of vortex breakdown there was a mismatch in axial vorticity and total pressure cores whereas neither the maximum nor the local minimum axial velocity cores align with minimum total-pressure core.

The evolution of $\zeta s/U_\infty$, v_θ/U_∞, u_{core}/U_∞, u_{max}/U_∞, and $\Delta p_o/q_o$ distributions for $\alpha = 18^o$ with downstream distance plotted against the radial distance scaled by local semi-span are illustrated in Figure 4.4-3. It is observable that in post breakdown region a drop in peak vorticity core value is accompanied by a corresponding increase in spanwise extent of the vorticity distribution, indicative of vorticity diffusion. The tight confinement of the tangential velocity also diffused over the downstream distance but regardless of breakdown the asymmetry in circumferential distribution is evenly evident in post breakdown region. Comparison of the core axial velocity and maximum axial velocity explained that with in a ~10%c the core redefined itself from being jet-like to wake-like in vicinity of vortex breakdown. The subsequent effect of this rapid core deceleration relocated the pre-existing jet-core away from the vortex center and as a result two distinctive regions of jet-like and wake-like flow are visible along the horizontal line passing through the vortex center. A predictable behaviour has been shown by the maximum axial velocity which remained fairly constant for x/c 0.4 to 0.6 then afterwards a gradual drop is witnessed over the wing surface. Lastly, it was confirmed that the maximum pressure loss fluctuates about a certain minimum value which is insensitive to chordwise location, i.e. upstream or immediate downstream of the vortex burst. On passing the breakdown location the extent of the loss increases from ~28% of local semi-span to ~40% of local semi-span.

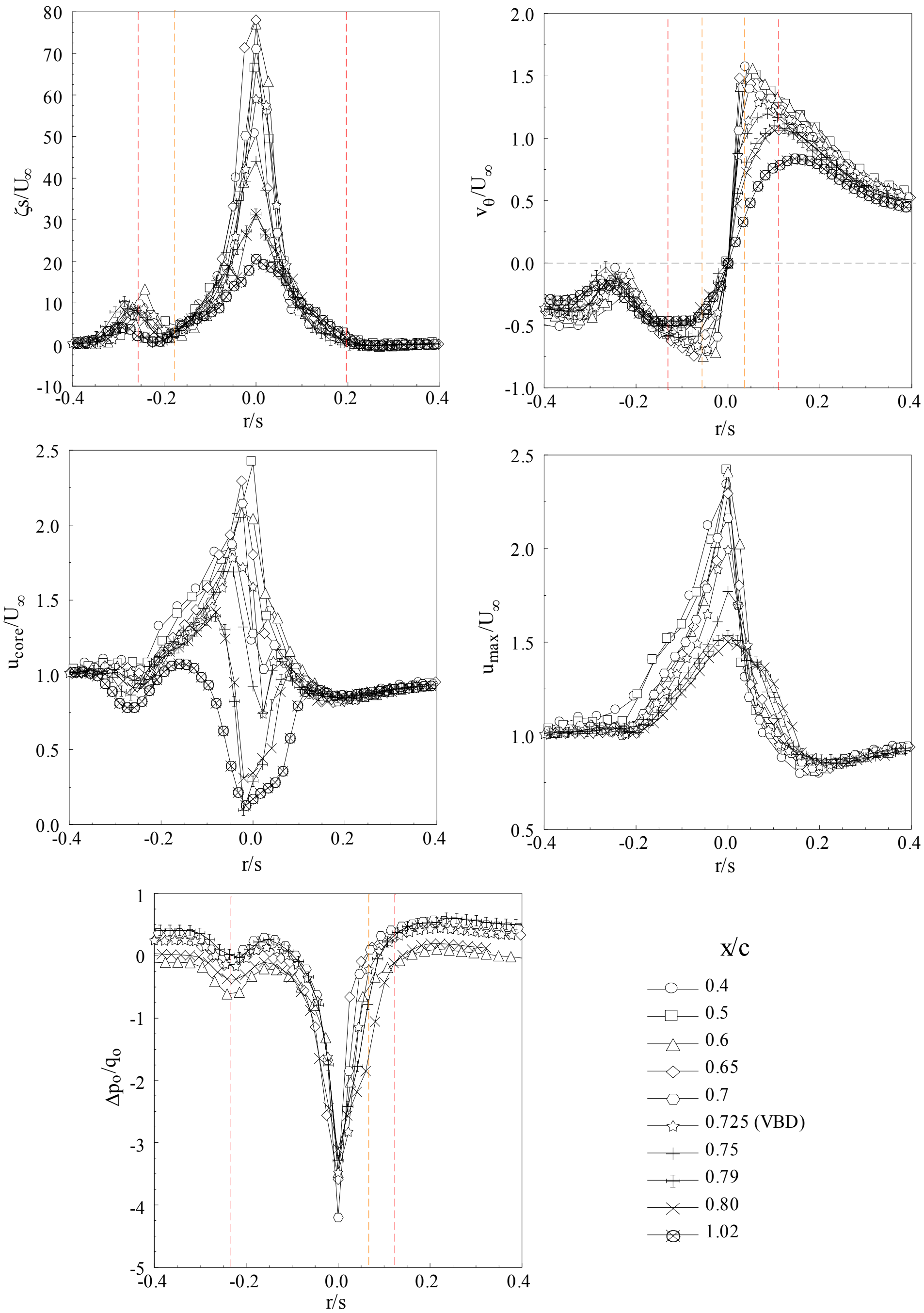

Figure 4.4-3 Stream variation of vortex flow quantities for DW65 at α = 18°

Further insight into the flow in vicinity of the breakdown was obtained from the illustration of critical vortex parameters with downstream distance, given in Figure 4.4-4**.** Prior to the breakdown (x/c = 0.725), the normalized peak axial vorticity dropped to half the peak value over a distance of 0.1c whereas an abrupt shift from jet-like to wake-like was witnessed for core axial velocity. It is to note that the location of maximum and the core axial velocity never matches. This discrepancy or mismatch is understandable, since prior to the breakdown the vortex is developing under the continuous feed of vorticity and, post breakdown the deceleration of the core drifted the jet flow away from the center. The maximum tangential velocity remained fairly constant before suffering a drop at around x/c = 0.6, indicative of vortex diffusion anticipated by the onset of vortex breakdown. In the latter quarter of the wing, from x/c = 0.80 to 1.02, the aforementioned vortex quantities faced a nominal depreciation which concluded the extenuation of adversities associated with vortex breakdown.

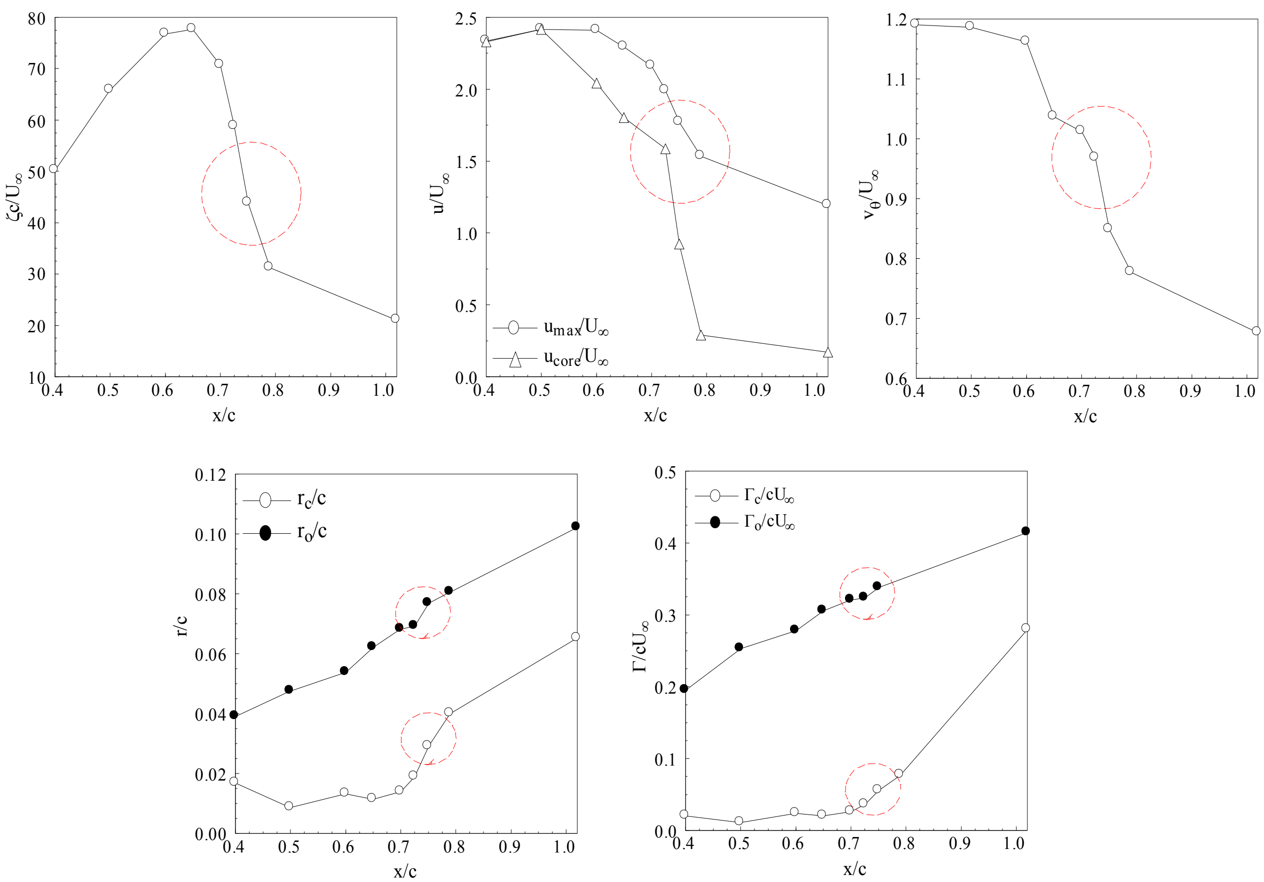

Figure 4.4-4 Streamwise variation of critical vortex parameters for DW65 at α = 18° (red: anticipated VBD)

It is interesting to analyse the vortex sizing and strength vis-à-vis vortex breakdown. Prior to the breakdown, the outer radius varied linearly with downstream distance, indicative of continuous spiralling of shear layers. Interestingly, the core radius and core circulation remained fairly constant before being disturbed by the vortex breakdown. The vortex core size rapidly increases in vicinity of breakdown along with the circulation bounded with the vortex core. Although the initiation of the vortex breakdown is by the excitation of core parameters but since the leading-edge vorticity feed continued regardless of the breakdown, the vortex kept on entraining the shear layer vorticity hence the increase in outer radius is insensitive to vortex breakdown. In the vicinity of the trailing-edge, from x/c = 0.8 to 1.02, the core circulation increased by multiple times. The reason for this peculiarity is the mitigation of differential in distribution of tangential velocity and ratio Γ_c/Γ_o approached ~0.65, closer to the theoretical value of ~0.715 for a fully developed laminar vortex.

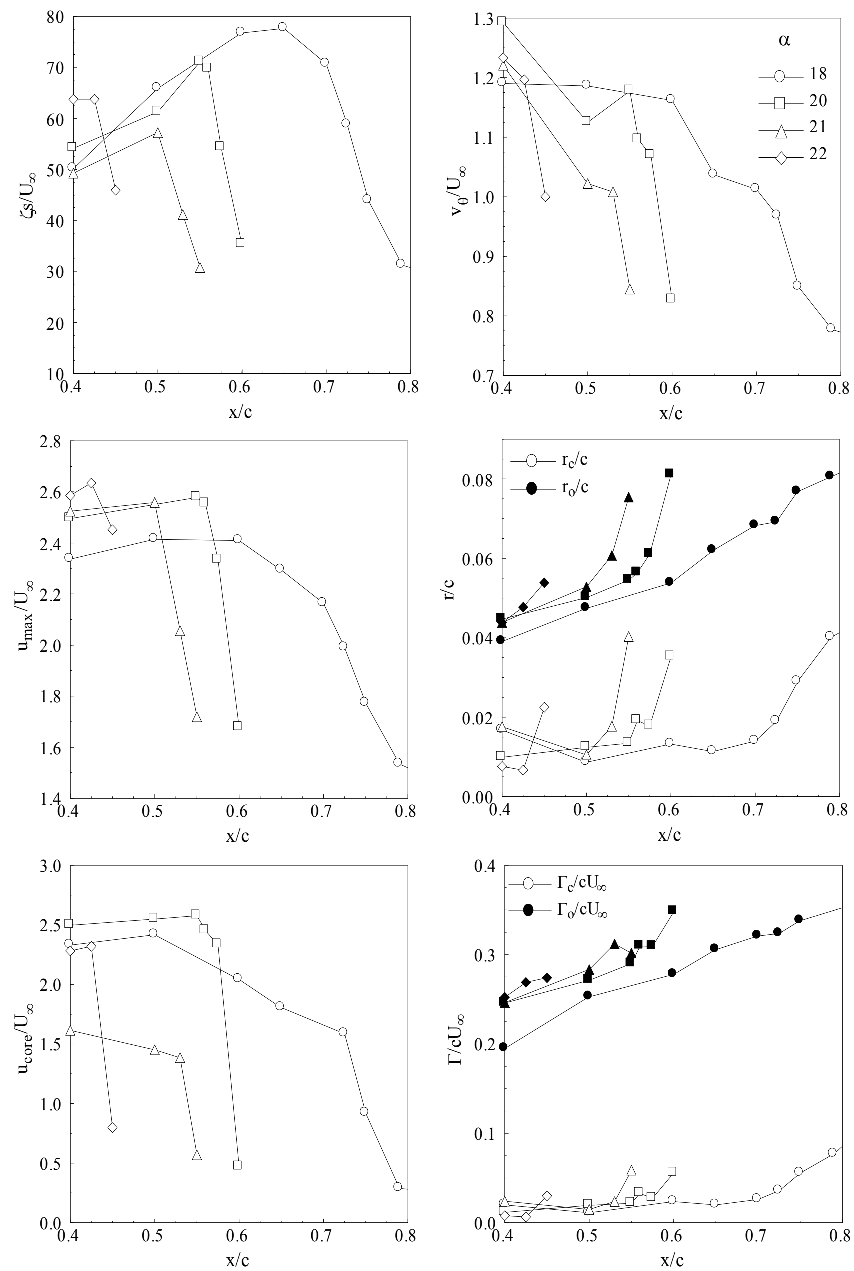

Figure 4.4-5 Streamwise variation of critical vortex parameters for different angles of attack for DW65

Similarly, Figure 4.4-5 illustrates the variation of critical vortex parameters at higher angles of attack. It is observable that with angle of attack the upstream progression of the breakdown location overshadowed the adverse trailing-edge effects, therefore, in contrast to α = 18°, no gradual decreases in peak values were witnessed over the wing surface.

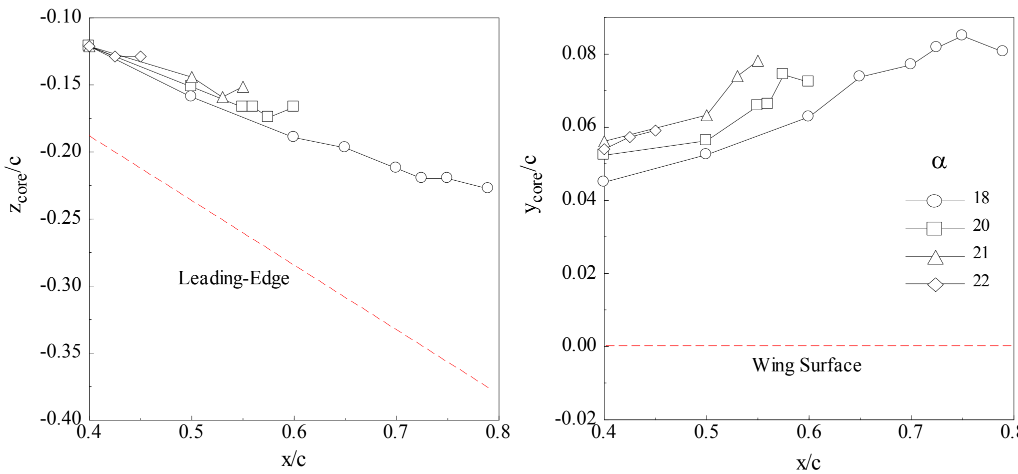

Figure 4.4-6 Streamwise variation of normalized vortex trajectory for DW65 at α = 18°

Figure 4.4-6 shows the normalized vortex trajectory along the spanwise (z/c) and traverse axis (y/c). It is observable from the plots that traverse location followed the predictable trend of moving away from the wing surface with downstream distance whereas the spanwise location (z/c) showed a trend of remaining at the same location in the vicinity of vortex breakdown before following the trend of moving away from the centerline. Figure 4.4-7 presents the approximated location of vortex breakdown over the DW65. It is to mention that the unsteadiness and the associated fluctuations in vortex breakdown location are already discussed in background section and the Figure 2.2-2 reflected the scatter in breakdown measurements. Recall that, in past the documentation of breakdown locations has only been done by flow visualization but under the present study it was reported on basis of three-dimensional flow field information.

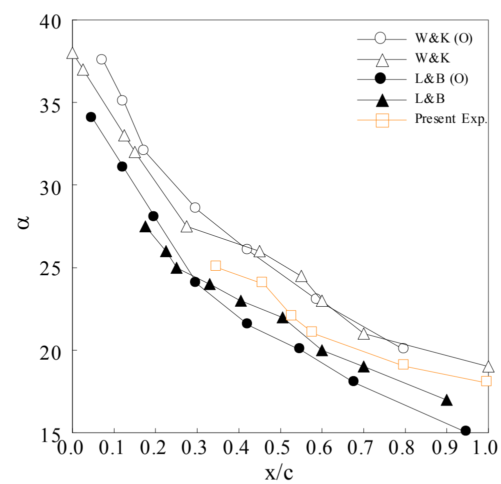

Figure 4.4-7 Vortex breakdown over DW65

In the case of DW50, the vorticity and velocity information are not conducive but the qualitative information can be extracted from the total pressure loss contours. Figure 4.4-9 shows the streamwise evolution of the constant total pressure loss contours at an incidence of α = 6° and 10°.

It is obvious from the constant total pressure loss contours that upon the arrival of anticipated vortex breakdown the pressure loss expanded to fill the entire vortex cross-section. For α = 6°, the pressure distribution showed symptoms of vortex breakdown in vicinity of x/c 0.7. Similarly the approximation of breakdown locations is presented against the published data. It has been understood that in the case of non-slender delta wings the

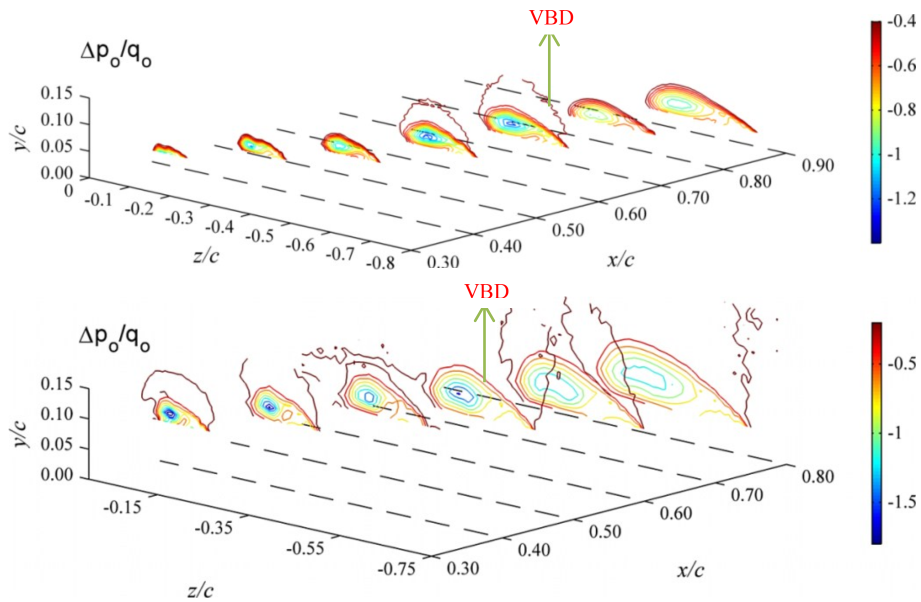

Figure 4.4-9 Streamwise variation of normalized total pressure loss for DW50 at α = 6° & 10°

vortex breakdown is relatively a highly sensitive phenomena and often accompanied by high degree of unsteadiness. Moreover, as already discussed, the accuracy of flow information is further compromised by relatively smaller size and low proximity of vortex to wing surface. Therefore the exact location of vortex breakdown must be referred with caution considering the accumulation of inherited numerical and physical uncertainties.

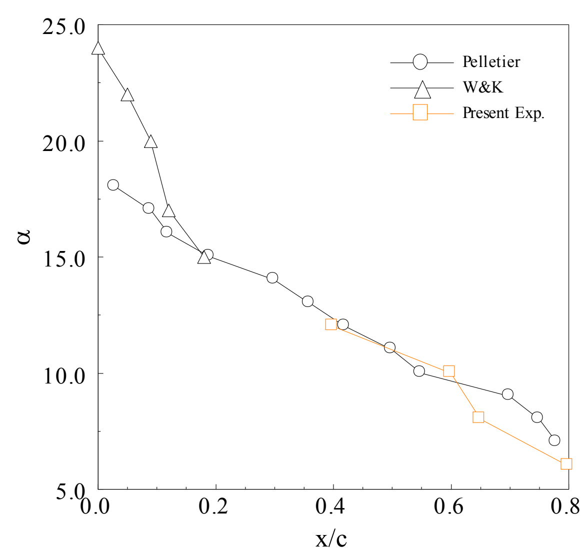

Figure 4.4-8 Vortex breakdown over DW50

Figure 4.4-8 presents the vortex breakdown location for DW50 approximated from streamwise evolution of the aforementioned total pressure loss contours.

4.5 Lift estimation

4.5.1 Experimental and Theoretical Comparison

In this section the aerodynamic characteristics of the two models were discussed, firstly the direct measurements of the lift were reported for two different Reynolds number and then the comparison was made with coefficients computed through wake survey analyses.

Figure 4.5-1 shows a comparison of lift coefficient based on wind tunnel experiments conducted by different researchers at different Reynolds number with direct measurements from the present study. Except Wentz & Kohlman [37] and Verhaagen [41], all others are within a close range of the current experiment. As understood, aerodynamic loads over a delta wing are function of various parameters, i.e. flow quality, model geometry, support mechanism etc., therefore no direct comparison can be made It is noted that positive lift is observed at zero angle of attack as a consequence of negative camber induced by leeward side bevelling.

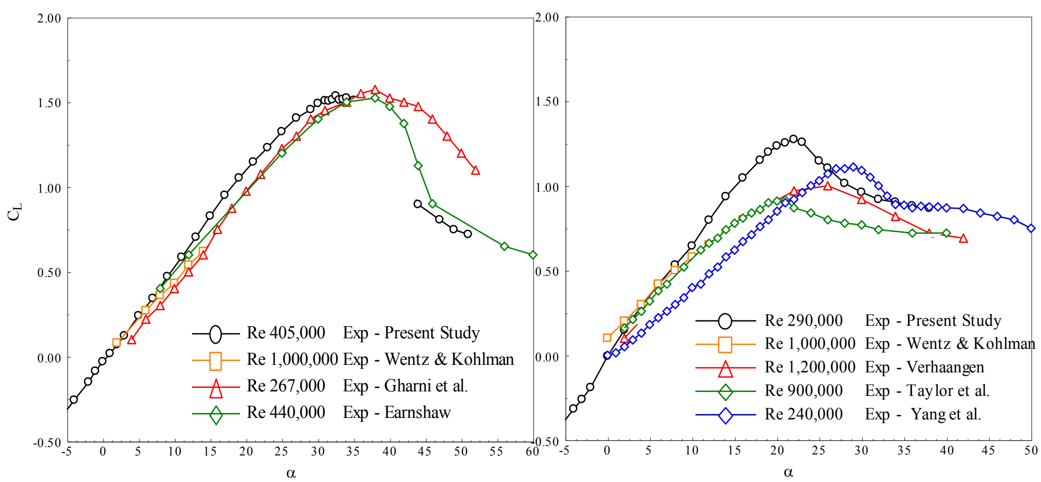

Figure 4.5-1 Lift curve for DW65 (left) and DW50 (right) extracted from literature under different flow condition

The theoretical approximation of lift over a delta wing can be made by Polhamus theory. The total lift is given by the summation of potential lift and vortex lift whereas the required coefficients can be approximated from the graph provided in literature against the wing aspect ratio. These coefficients are reflective of leading-edge vortices strength and related parameters. Figure 4.5-2 compared the force balance measurements against the theoretical Polhamus estimation. The lift curves belonged to DW65 and DW50 at Reynolds number of 409,000 and 290,000 respectively. Although the theoretical estimation is based on various assumptions but, as understood, the higher the sweep angles higher the accuracy of theoretical model. Therefore the results are more in agreement with DW65 than for DW50. The plot also highlights the contribution of distinct mechanisms towards the total lift generation. In comparison, on increasing the angle of attack the proportion of vortex lift to total lift increases for DW65 because of the stronger leading-edge vortices.

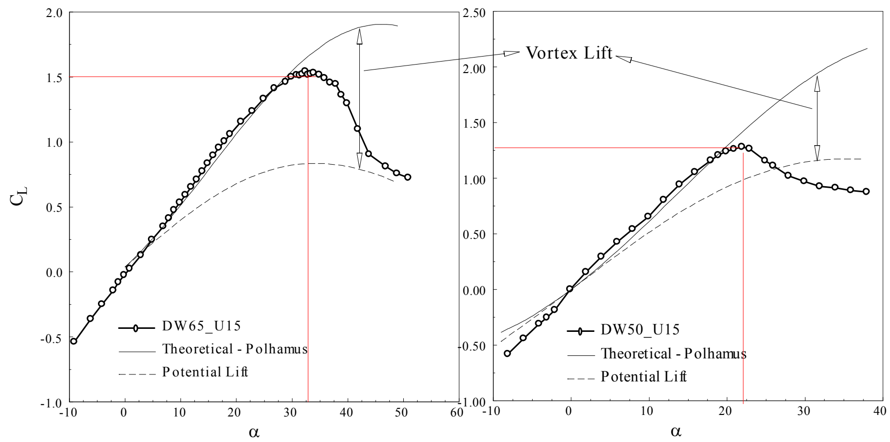

Figure 4.5-2 Comparison of Theoretical and Experimental lift for DW65 and DW50 at $U_\infty = 15$ m/s

4.5.2 Wake survey Analysis for Lift estimation

The Figure 4.5-3 shows the spanwise distribution of the circulation computed by integrating the vorticity field. In order to capture the complete flow information and limiting the wake entrainment effects, the measurement plane was located just aft the trailing-edge at x/c = 1.02. It is visible from the plot that for the range of angles of attack, about 90% of the total circulation is confined by the primary vortex. It is interesting to note

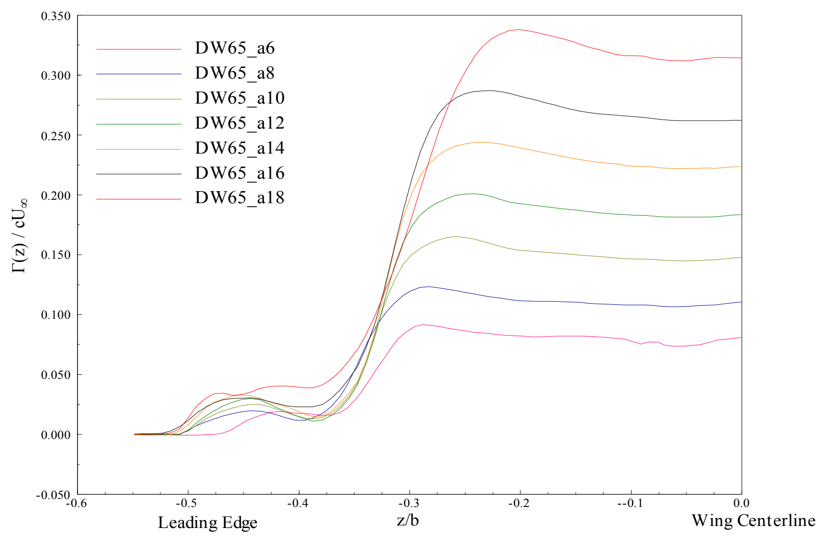

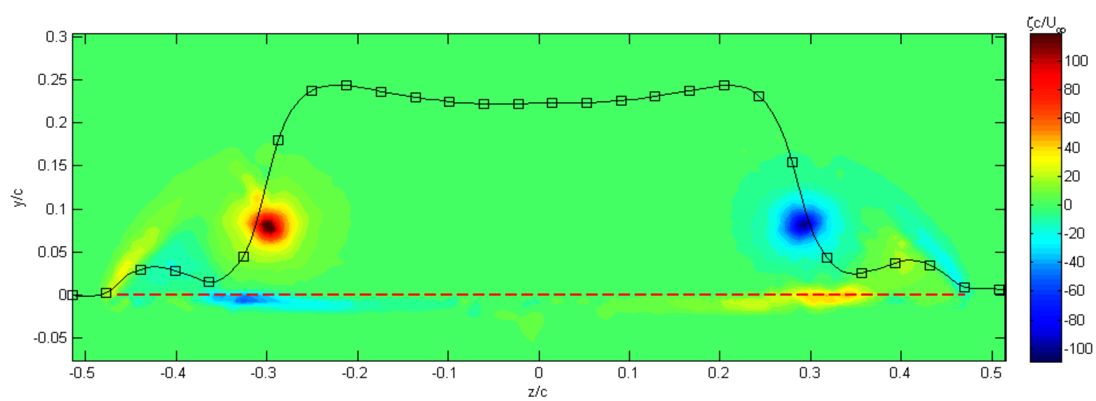

Figure 4.5-3 Bottom: Combined plot of Vorticity field of DW65_a14_x1.02 and spanwise circulation distribution Γ/cU_∞, Top: Half span spanwise circulation distribution of DW65 at different angle of attack

that on increasing the angle of attack, circulation at wing centerline increases in a linear fashion (Figure 4.5-5) given that for all the cases, angle of attack (4°-18°), the vortex breakdown have not reached the wing trailing-edge.

Comparison of direct and indirect C_L for DW65 is given in Figure 4.5-4. It is evident that the agreement between the direct and indirect measurements presents itself quite readily in the fact that the C_L values are within the experimental uncertainty. However, given the assumptions for lifting line theory it always overestimates the lift values while on the other hand Kaplan formulation based on Stokes integral underestimates the lift coefficient. It is noted that on increasing angle of attack both the lift values based on Kaplan – Stoke and Lifting Line theory diverges away from the force balance measurement because they incorporate vorticity values. The sensitivity associated with accurate evaluation of vorticity numerical values is already discussed in background section therefore on increasing the angle of attack the vorticity value increases and so do the inherent uncertainty.

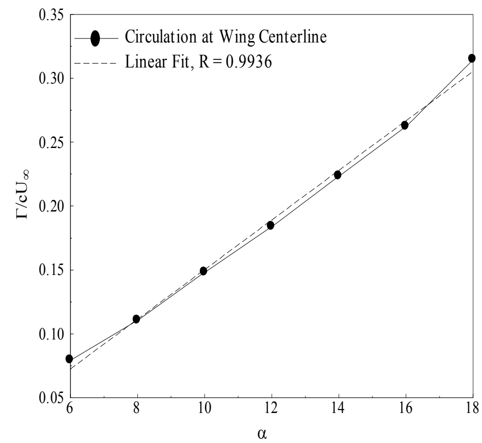

Figure 4.5-5 Γ/cU_∞ at z/c = 0 for DW65

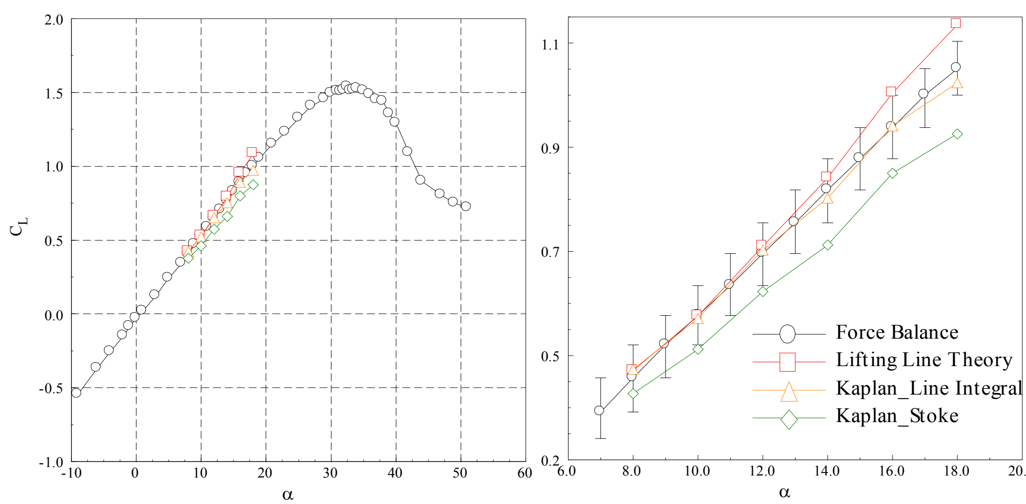

Figure 4.5-4 Direct and indirect lift measurements for DW65

In Figure 4.5-7, the calculations were made at different downstream stations to demonstrate the effect of streamwise distance on lift computation. The dotted lines shown are the high and low values of lift depending on the uncertainty associated with the force balance. The flow information is acquired for DW65 at an incidence of 16°. It is obvious that at x/c = 1.28 and 1.4 the difference between the values is minimum. From here onwards they start diverging and the maximum is recorded at x/c = 2. Unlike the trailing tip vortices, leading-edge vortices losses their coherence and stability within few chord distances downstream of the trailing-edge. The reason might be the high rotational flow which promotes early breakdown and the large size compared to tip vortices induces additional turbulent diffusion. Therefore the discrepancy in lift values is observed for increasing downstream distance.

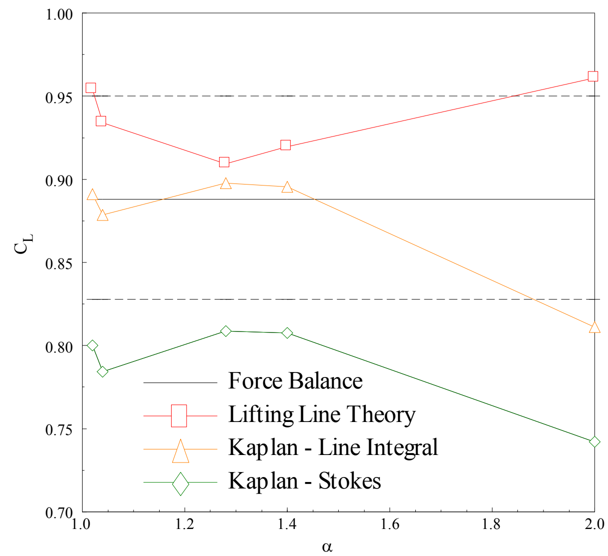

Figure 4.5-7 C_L for DW65_a16 at different streamwise stations

In Figure 4.5-6, circulation distribution against the non-dimensional spanwise distance of downstream stations has been presented to illustrate the in-wake evolution of total circulation. It is to note that discernable region of negative circulation is observed for x/c = 1.28 and 1.40, whereas lift coefficients computed from these stations are within the uncertainty level and close to the force balance average. From the information it can be deduced that about half the chord length downstream of trailing-edge is needed by the vorticity contained in free shear layer and secondary vortex to take-up a computable shape. While at x/c = 2.0, wake entrainment effect and dominance of single sign vorticity is evident as no overshoot is witnessed in circulation distribution.

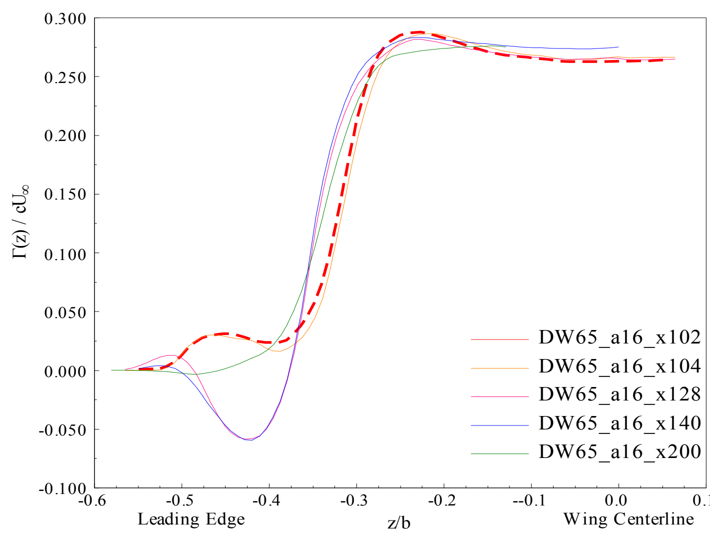

Figure 4.5-6 Γ/cU_∞ for DW65 at various streamwise locations

Figure 4.5-9 displays the lift characteristics of DW50, being the non-slender version, as previously mentioned, the flow field information is susceptible to numerical noise because of small absolute values. In addition, for selected angles of attack the breakdown is in vicinity or upstream of trailing-edge which contaminates the velocity field and intensifies the risk of error accumulation. Therefore the wake survey analyses resulted in discrete data points but are still within the debatable range. For each angle of attack, the spanwise distribution of circulation is presented to illustrate that, total circulation is preserved even though the vortex breakdown already crossed the trailing-edge. Therefore, vortex breakdown should be seen as local diffusion of vorticity rather than a loss of vorticity.

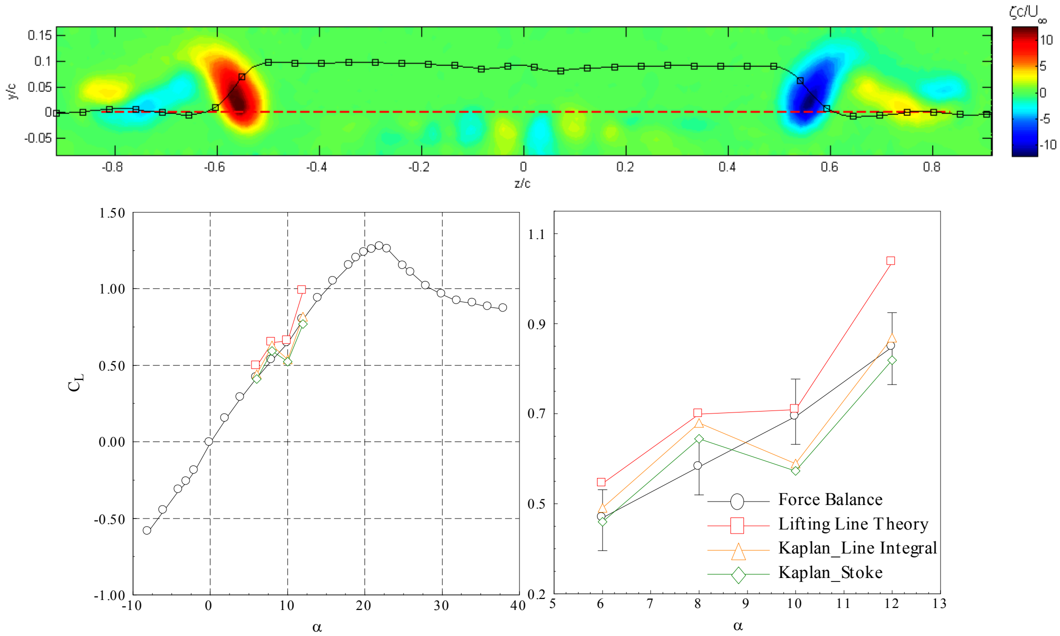

Figure 4.5-9 (Top) Combined plot of non-dimensional vorticity and circulation distribution for DW50_a6_x150, (Bottom) Direct and Indirect Lift coefficient presented for DW50 at U_∞ = 15 m/s

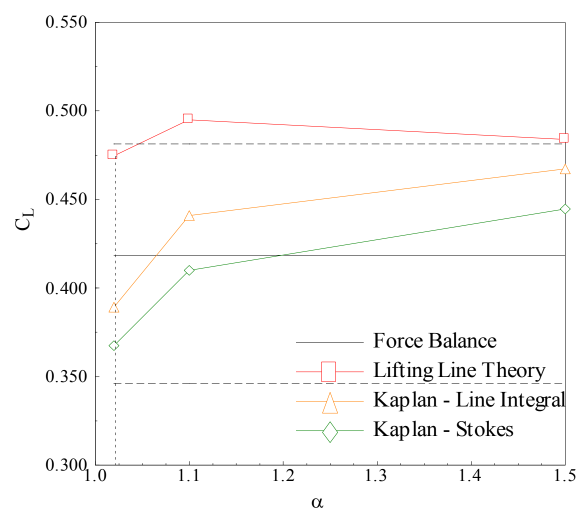

Figure 4.5-8 C_L for DW50_a6 at different streamwise stations

Referring to the Figure 4.5-9 (Top), which presents axial vorticity for DW50 at an incidence of 6º and x/c = 1.50, highlights the containment of circulation by primary vortex and a small region of same sign vorticity in leading-edge area. As the flow progresses downstream the free shear layer rolls up in primary vortex but in the case of DW50, the spanwise extension of rotational flow disintegrates the shear layer in a pair of opposite sign vortices. Moreover the proximity of support mechanism to the trailing-edge is noticeable through vortices near wing centerline and eventually in depreciation of total circulation. The effect of downstream distance on computation of C_L is presented in Figure 4.5-8. Likewise the DW65, on increasing the downstream distance all three formulations converge to a single value and minimum difference is witnessed for x/c = 1.50, which is also the farthest station investigated in present study.

On increasing the downstream distance (Figure 4.5-11, red), as already discussed in section 4.3, the vortical flow rolls up in three distinct regions; main vortex region and two small regions of opposite sign vorticity. It is observed that this re-organization of flow reduces the variation in computation of indirect C_L (Figure 4.5-8).

Figure 4.5-10 (Left) presents the comparison of spanwise circulation distribution over DW50 at different angle of attack where the noise in centerline reflects the close proximity of support arm to wing trailing edge whereas Figure 4.5-10 (Right) compares the distribution over DW65 and DW50. It is noticeable that at a given angle of attack a decrease in sweep angle results in higher circulation, confirms the observation made in background study.

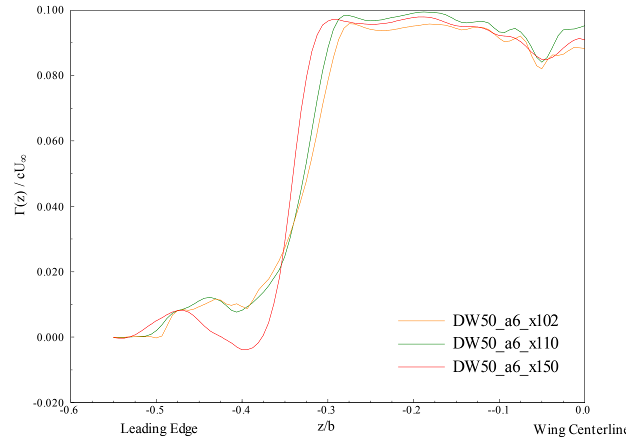

Figure 4.5-11 Γ/cU_∞ distribution for DW50 at various streamwise locations

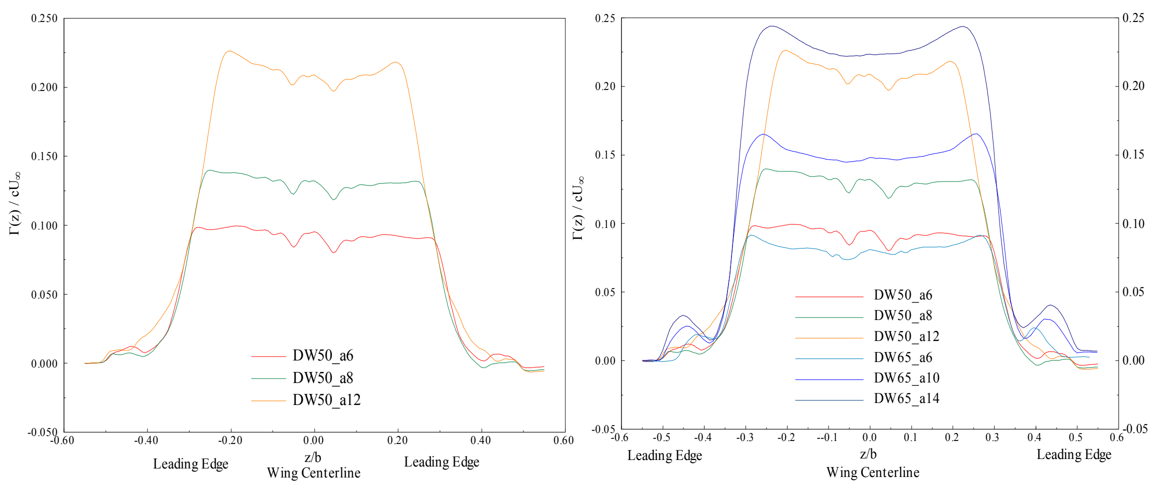

Figure 4.5-10 (Left) Full span circulation distribution for DW50 at various angles of attack, (Right) Full span DW65 and DW50 circulation comparison

4.6 Drag estimation

In this section drag information acquired for DW65 and DW50 will be discussed. Direct measurements from force balance are presented against the indirect evaluation of drag components from wake survey analyses. Particular attention is given to the source characterization of total drag on the basis on lift dependency, i.e. profile drag and induced drag.

Figure 4.6-1 presented the drag coefficient of DW65 and DW50 at Reynolds number of 405,000 and 290,000 respectively. The measurements were made directly using the 2-axis force balance system. It was observable that for lower angles of attack the increase in drag is gradual, up to an incidence of ~ 10^{o}, beyond that the increase is more pronounced until

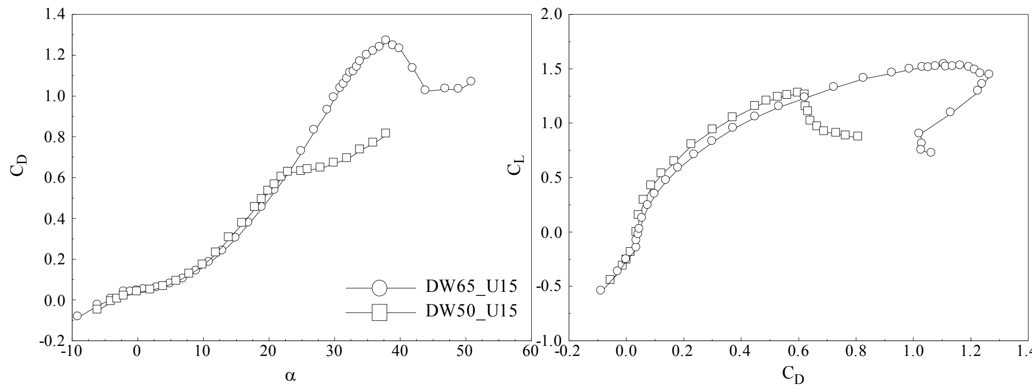

Figure 4.6-1 Drag coefficient and Drag polar for DW65 and DW50 at U_∞ = 15 m/s

the wing stalls. The drag polar indicated that for a given lift condition DW50 has lower drag values then its slender counterpart and has a superior L/D. In the case of DW50, on increasing the Reynolds number Figure 4.6-2 there is an obvious deterioration of aerodynamic drag while on the other hand for DW65 the drag values almost overlapped prior to the breakdown reaches the trailing-edge. This detrimental effect on DW50 overshadowed the lift increment and eventually resulted in an inferior L/D.

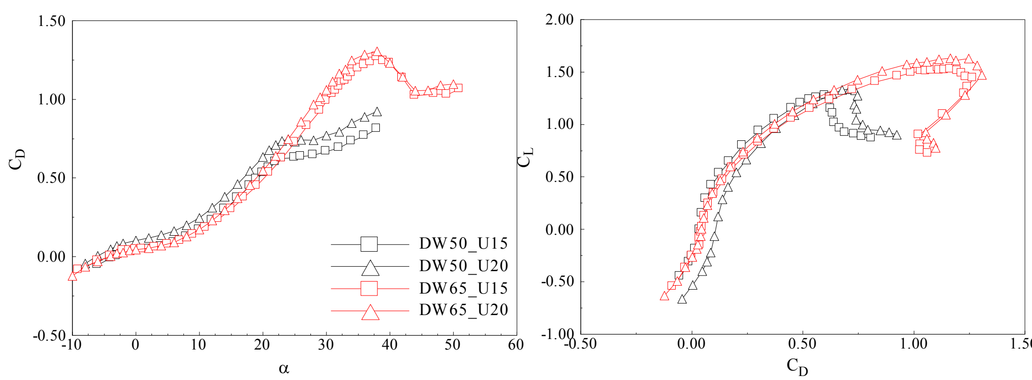

Figure 4.6-2 Drag coefficient and Drag polar for DW65 and DW50 at U_∞ = 15m/s and 20 m/s

Further insight into total drag over the delta wings was obtained from conducting the wake survey analysis presented by Kusunose [49]. It has been discussed that computing the profile drag arises various numerical difficulties and supplement accumulation of errors because of highly three-dimensional flow over the low aspect-ratio wing. On the other hand the resolution of sections undertaken for profile drag calculation is relatively commendable for wings with high aspect ratio. In the case of delta wings, information over a large grid is required to compensate for errors tempted by high core axial velocities and to mitigate the uncertainty in defining the free stream velocity. Therefore it is opted to define the profile drag by subtracting the induced drag (computed by Maskell formulation) from total drag and later on, for comparison, an attempt was made by using the integral approach simplified by wake identification criterion given by Giles & Cummings [63]. It is to mention that induced drag can be analytically approximated by using the relation given by Polhamus [52], $C_{Di} = C_L \tan\alpha$.

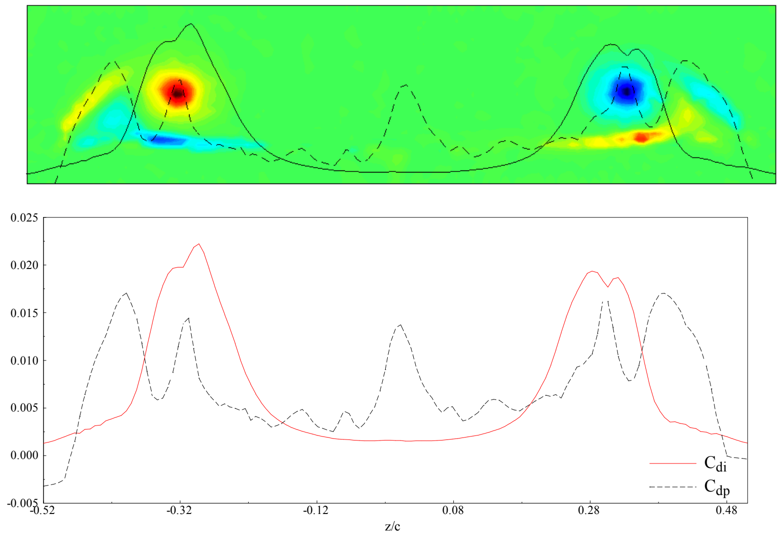

Figure 4.6-3 Spanwise distribution of approximated induced and profile drag for DW65_a10_x1.02

The Maskell formulation required flow information over the entire wind tunnel cross section which is not only problematic but is also prone to free stream background noise. On top of it, the formulation's sensitivity to grid resolution can incorporate numerical noise into the solution. Moreover, only to reach an approximate solution the resulting matrix formation demands supercomputing techniques to carry the desired operations. Therefore the constraints of traversing mechanism and computational labour cited an alternate approach of limiting the calculations for specified vortical wake area. The procedure and steps adopted for induced drag calculation can be found in Lee and Su [64] and Pereira [65]. An overview of which is presented in Appendix along with formualtions intended for profiel drag calculation.

Figure 4.6-3 presented the sectional distribution of profile and induced drag in wake of DW65 at an incidence of $\alpha = 10^{o}$. Understandably the major contributor in the case of profile drag is the high velocity deficit of secondary vortex whereas the high rotational flow of primary vortex contributes toward the induced drag. Note that the profile drag is viscosity dependent and is proportional to momentum deficit therefore multiple peaks occur in distribution along the span representing the spread of velocity deficit and an observable peak is witnessed about the wing centerline reflecting the deficit induced by support mechanism. At the given incidence, the peaks about the centerline contribute to ~15% of the total

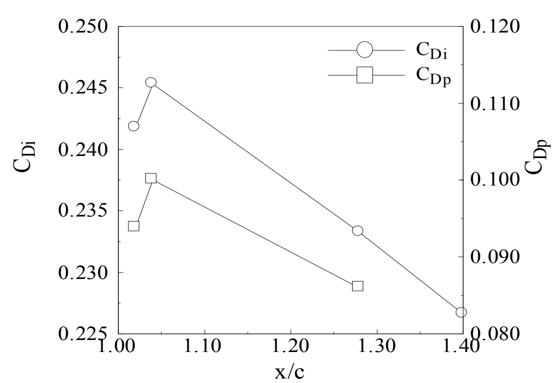

Figure 4.6-4 Effect of downstream location of measurement plane on drag calculation computed for DW65_a16

profile drag. On the other hand the dual peak in induced drag is attributed towards the differential of crossflow velocities across the vortex center. This asymmetry in tangential velocity is already discussed in previous sections. Studying the effect of downstream location of the measurement plane Figure 4.6-4 reveals that drag coefficients tends to increase for few hundredth of chord distance then relatively a linear decrease in both induced and profile drag is observed. This can be attributed to alteration of data through free stream entrainment in velocity deficit wake flow.

Table 4-2 lists the direct and indirect drag measurements computed for each of the individual cases. It has been shown for DW65 that the total drag values are almost in agreement with each other or at least within ±1° resolution of angle of attack. Conversely, disagreement is quite evident for α = 24° case because the breakdown already occurred well upstream of measurement plane. It was understood that the vortex breakdown resulted in highly turbulent trailing flow with high degree of unsteadiness which consequently corrupts the flow information. This disagreement is also observable in DW50 cases where breakdown already reaches the trailing-edge at about α = 6°. It was found that the subsequent effect of upstream breakdown results in noticeable drop in experimental induced drag values which ultimately underestimates the total drag coefficient. In the worst case, prior to the breakdown and considering the uncertainty in angle of attack for DW65, disagreement between the wake survey and force balance is less than 5%.

Table 4-2 Direct and Indirect measurement of Total drag for DW65 and DW50 at U_∞ = 15 m/s

Wing	α	Total Drag[1]	Induced Drag	Profile Drag	Total Drag
DW65[2]	8	0.1191	0.0562	0.0438	0.1
	10	0.1601	0.0791	0.0565	0.1355
	12	0.2098	0.1375	0.0968	0.2343
	14	0.2679	0.1631	0.0876	0.2507
	16	0.3340	0.2418	0.0938	0.3356
	18	0.4079	0.3164	0.0950	0.4114
	24[3]	0.6723	0.4404	0.1430	0.5776
DW50[4]	6	0.0895	0.01672	0.0521	0.069
	8	0.1255	0.03207	0.0519	0.084
	10	0.1695	0.05024	0.0478	0.099
	12	0.2291	0.06391	0.0388	0.103

The behaviour of induced and profile drag for DW65 with respect to increasing angle of attack is made visible in Figure 4.6-5**.** On increasing angle of attack, as the strength of the vortices increasing so do the cross flow velocities the induced drag witnessed an increase while on the contrary profile drag settles down beyond a certain angle of attack or in other words the differential is overshadowed by the increase in induced drag. As expected, the

[1] Direct measurement from Force Balance
[2] Measurements are made at x/c 1.02, TE x/c = 1.0
[3] Vortex breakdown at x/c = 0.345
[4] Measurements are made at x/c 1.10, TE x/c = 1.0

theoretical approximation of induced drag always overestimates the drag coefficient whereas in contrast the wake survey analysis underestimates the induced drag in post break breakdown regions. This is further supplemented by the comparison of drag coefficient obtained for DW50. Figure 4.6-6 shows the obvious discrepancy in computed and direct measurements given the fact that computed induced drag is underestimated for the post

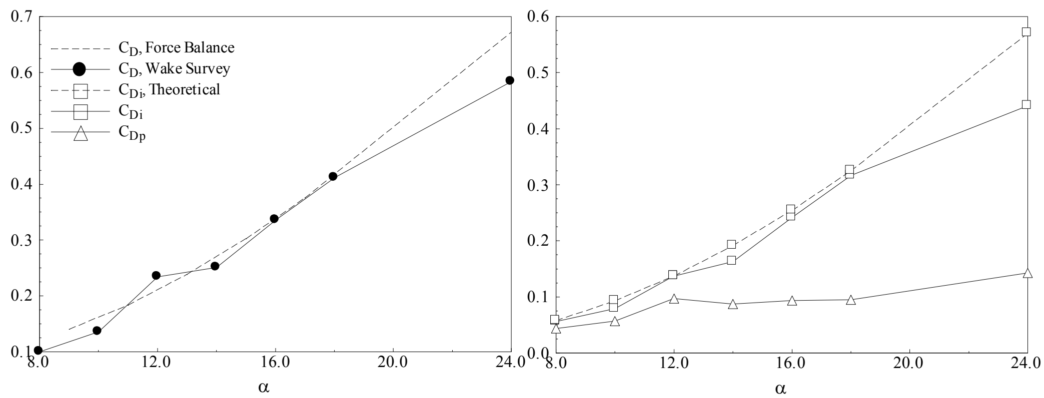

Figure 4.6-5 Comparison of Theoretical, Direct and Indirect Experimental drag for DW65

breakdown cases. Surprisingly, the augmentation of theoretical induced drag and experimental profile drag resulted in total drag coefficient comparable to direct drag measurements. A useful comparison between slender and non-slender delta wings can be drawn by comparing the relative span efficiency factors as given in Table 4-3. However the underestimation of induced drag in the case of DW50 eclipsed the prospective comparison whereas computing the span-efficiency using the theoretical C_{Di} enlightens the effect of breakdown on wake survey analysis.

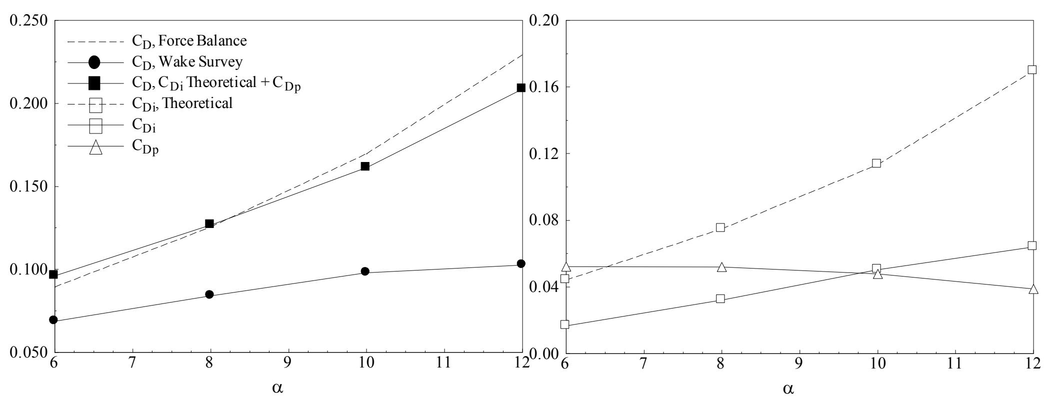

Figure 4.6-6 Comparison of Theoretical, Direct and Indirect Experimental drag for DW50

Lastly, the grid dependence of computed induced drag is studied through reducing the cell size. Figure 4.6-7 presents the comparison between the two different grid sizes for DW65 at an incidence of α = 16°, i.e. 1/8" and 1/2" equivalent to 104,448 and 6860 points respectively. It has been known that if the experimental grid is sufficiently dense then the computed values are insensitive to grid density while on increasing the cell size the accuracy of vorticity distribution is compromised. But despite of this increase in grid size one can easily capture the proper amount of vorticity. Furthermore the cross flow kinetic energy is apparently insensitive to vorticity distribution but increase in cell size beyond a certain threshold triggers the inaccuracy in vorticity distribution and induced drag begins to decay. Figure 4.6-7 made it clear that increase in grid size deteriorates the induced drag coefficient where in worst case scenario a drop of ~15% is recorded.

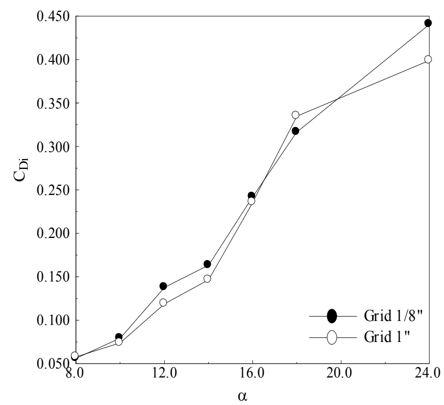

Figure 4.6-7 Effect of Cell Size on Drag calculation for DW65

Table 4-3 Comparison of Theoretical and Experimental Induced Drag and the Span Efficiency

`Wing	α	Theoretical Induced Drag	Experimental Induced Drag	%age Total Drag	Span efficiency	Theoretical Span efficiency[1]
DW65	8	0.0573	0.0562	56	50	49
	10	0.0928	0.0791	58	59	50
	12	0.1374	0.1375	59	51	51
	14	0.1915	0.1631	65	61	52
	16	0.2546	0.2418	72	55	52
	18	0.3236	0.3164	77	54	52
	24	0.5699	0.4044	75	63	48
DW50	6	0.4344	0.0167	24	99	38
	8	0.0748	0.0320	38	84	36
	10	0.1135	0.0502	52	78	35
	12	0.1696	0.0639	62	94	36

[1] Computed using the theoretical Induced Drag

Chapter 5

5 Conclusion

5.1 Vortex flow characteristics

5.1.1 Variation with chordwise location

DW65:

a) Prior to the VBD reaching the trailing-edge, ζ_{peak} remained fairly constant when scaled by wing chord and increased linearly when scaled by local semi-span
b) The vortex core (~20% of local semi-span) when non-dimensionalized with respect to local semi-span, indicative of the conical nature of the flow and u_{max} is also a constant and suffered a drop in the vicinity of the trailing-edge
c) The streamwise pressure gradient created by a streamwise increase in tangential velocity helped increasing the axial core size rather than the core axial velocity
d) The tangential core is ~ half the size of vortex core showing tight confinement of vorticity concentration
e) Vortex core and axial core never matches due to the continuous development of vortices by the leading-edge feeding sheet
f) Downstream of the trailing-edge there appeared a region of momentum deficit along the vortex axis well before breakdown reached the trailing-edge, suggestive of imbalance created by absence of vorticity feed which also shifted the asymmetry in tangential velocity about the vortex center
g) Regardless of angle of attack, the deficit in secondary vortex and core axial velocity remained constant
h) Within a chord distance downstream of trailing-edge, regions of opposite signs of vorticity merged together into a single diffused vortex with large momentum deficit spread across the vortex therefore unlike the trailing vortices, the high tangential velocities and negative interaction between PV and SV terminated the vortex progression downstream of trailing-edge
i) The vortical flow tried to suppress the instability induced by VBD and developed into a laminar vortex but the aforementioned adverse interaction hinders the restructuring and resulted in large scale diffusion, where value of $v_{\theta peak}$ dropped from $1.5U_\infty$ to $0.5U_\infty$
j) For VBD in downstream half of the wing, the onset is recognised by a gradual decrease in critical vortex parameters whereas a sudden drop is observed for cases in upstream half of the wing

k) Instability in iso-contours of cross-flow velocity hinted the downstream presence of VBD
l) The VBD was characterized by an appearance of wake-like region along the vortex axis which drifted the jet-like flow away from the center
m) The momentum deficit encompassed the whole vortex core within 0.1c downstream of the anticipated VBD
n) Despite the VBD, the vorticity from feeding sheet continued to roll-up and vortex increases in outer radius until the termination of leading-edge feed occurred at wing trailing-edge
o) The change in vortex core radius is more pronounced than increase in vortex order radius
p) On VBD the vortex center retained its spanwise position (z/c) for at least few percentage of chord distance

DW50:

If compared with DW65, the quantitative information extracted for DW50 is limited because of the limitations mentioned in chapter 4. Despite that, the experimental investigation is first of its kind and results are qualitatively and quantitatively repeatable therefore the following observations were made to highlight the behaviour of flow over DW50

a) It was found out that the three-dimensional information is not revealing due to the small size and close proximity of the vortex to the wing surface
b) u_{max} always appears in the outer region of the vortex, indicated that the component of feeding sheet in the direction of free stream is a main contributor towards the streamwise acceleration.
c) Total pressure loss is symmetric and concludes that regardless of sweep angle the vortex flow respects the evenness of total pressure loss about the vortex center
d) At low angles of attack and in upper half of the wing, multiple peaks are observable in vorticity field with multiple axial cores, indicating the formation of dual vortices whereas the presence of the probe promoted early breakdown of secondary same sign vortex
e) The VBD crossed the trailing-edge way earlier than DW65 therefore the disorganization across the vortical region is evident for every case investigated in wake except at $\alpha = 6^{o}$
f) Irrespective of upstream condition, within 0.5c downstream of trailing-edge the vortical flow organizes itself into a 3 distinct regions of vorticity concentration; two same sign separated by an opposite sign region
g) The axial core velocity is wake-like before it even leaves the wing surface therefore with downstream in wake of DW50, unlike the slender wing where the deficit

increases with distance, the entrainment from free stream decreases the axial momentum deficit and within 0.5c the axial flow recovered to ~$0.8U_\infty$

h) There witnessed an increase of 3-4 times in critical vortex parameters at x/c = 1.50 when angle of attack was changed from 4^o to 6^o
i) The classical definition of VBD cannot be applied for DW50 because of low absolute vorticity values and wake-like core.
j) The iso-contours of total pressure loss were informative in vicinity of VBD as they suffered an increase and decrease in size and peak, respectively.

5.1.2 Variation with angle of attack

DW65:

a) The vortex concentration increases with increasing angle of attack which resulted in approximately same core size but increased vorticity content
b) The increase in critical vortex parameters is almost linear with increasing angle of attack whereas tangential velocity and core axial velocity suffered a drop at high angle of attack indicating the proximity of VBD
c) The relative change in absolute maximum of tangential velocity distribution is higher than the change in absolute minimum
d) The relative distance of the vortex center from the leading-edge increases with increasing angle of attack
e) Regardless of angle of attack and prior to the VBD reaching the trailing-edge; the vortex outer radius and outer circulation and circulation at wing centerline increases almost linearly with downstream distance

DW50:

a) On increasing angle of attack the vortex tended to resemble the slender wing vortex but axial core always remained wake-like
b) u_{max} even reaches $1.5U_\infty$ but again only in outer region of vortex
c) ζ_{peak} remains constant for higher ranges of angle of attack

5.2 Aerodynamics

a) It was found that the C_{Lmax} increases with Reynolds number for both wings whereas the α_{stall} remained fairly constant
b) In both wings, the main source of profile drag is wake and SV whereas the PVs have their contribution towards the induced drag

DW65:

a) C_L estimated by line integral of tangential velocity was in agreement with direct force measurements while the approximation based on Stoke's theorem and lifting line theory deviated away from the C_L curve. This is because the integrand in the case of former is independent of vorticity and other derived quantities hence the lesser accumulation of numerical errors

b) The computation of lift at distinct downstream stations revealed that the C_L values converged to direct measurements up to x/c = 1.4 and then they started diverging away from the mean value
c) The aerodynamic drag observed a minimal increase with Reynolds number
d) On increasing angle of attack there was an insignificant change in profile drag whereas the induced drag kept on increasing
e) Increase in grid resolution improves the drag computation but substantially increases the computational time
f) Induced drag always constituted more than 50% of the total drag and span-efficiency remained fairly constant and higher than its non-slender counter part

DW50:

a) As the angle of attack increases accordingly the error in lift estimation increases. It was noticed that the early VBD corrupted the flow information which then resulted in erroneous C_L
b) Similarly, early VBD anticipated the underestimation of induced drag and consequently there was an obvious discrepancy in computed and direct drag measurements. While the combination of theoretical induced and computed profile drag were in close agreement with force balance values
c) There was an obvious deterioration of aerodynamic drag on increasing the Reynolds number

Chapter 6

6 References

1. Whitford, R., *Design for air combat,* 1987: Jane's Publication.
2. Benmeddour, A., Y. Mebarki, and X. Huang, *Computational investigation of the centerbody effects on the aerodynamics of delta wings.* RTO-AVT Rep, 2009. 84.
3. Nelson, R.C. and A. Pelletier, *The unsteady aerodynamics of slender wings and aircraft undergoing large amplitude manoeuvres.* Progress in Aerospace Sciences, 2003. 39(2-3): p. 185-248.
4. Rockwell, D., *Three-dimensional flow structure on delta wings at high angle-of-attack- experimental concepts and issues*, in 31st AIAA Aerospace Sciences Meeting & Exhibit, 1993: Reno, NV.
5. Visser, K.D. and R.C. Nelson, *Measurements of circulation and vorticity in the leading-edge vortex of a delta-wing.* AIAA Journal, 1993. 31(1): p. 104-111.
6. Mitchell, A.M. and P. Molton, *Vortical substructures in the shear layers forming leading-edge vortices.* AIAA Journal, 2002. 40(8): p. 1689-1692.
7. Earnshaw, P.B., *An experimental investigation of the structure of a leading-edge vortex.* British Aeronautical Research Council, Reports and Memoranda, 1961(3281).
8. Nelson, R.C. and K. Visser, *Breaking down the delta wing vortex: the role of vorticity in the breakdown process.* AGARD, Vortex Flow Aerodynamics 15, 1991.
9. Payne, F.M., et al. *Visualization and flow surveys of the leading edge vortex structure on delta wing planforms*. 1986. Reno, NV, USA: AIAA.
10. Payne, F.M., et al., *Visualization and wake surveys of vortical flow over a delta-wing.* AIAA Journal, 1988. 26(2): p. 137-143.
11. Taylor, G.S., T. Schnorbus, and I. Gursul, *An investigation of a vortex flow over low sweep delta wings.* 33rd AIAA Fluid Dynamics Conference and Exhibit, 2003.
12. Ol, M.V. and M. Gharib, *Leading-edge vortex structure of nonslender delta wings at low Reynolds number.* AIAA Journal, 2003. 41(1): p. 16-26.

13. Chen, L. and J. Wang, *Numerical simulations of leading-edge vortex core axial velocity for flow over delta wings.* Science in China Series E: Technological Sciences, 2009. 52(7): p. 2029-2036.

14. Gordnier, R.E. and M.R. Visbal, *Compact difference scheme applied to simulation of low-sweep delta wing flow.* AIAA Journal, 2005. 43(8): p. 1744.

15. Gordnier, R.E., et al., *Computational and experimental investigation of a non-slender delta wing.* AIAA Journal, 2009. 47(8): p. 1811-1825.

16. Moore, D. and D. Pullin, *Inviscid separated flow over a non-slender delta wing.* Journal of Fluid Mechanics, 1995. 305: p. 307-346.

17. Taylor, G. and I. Gursul. *Lift enhancement over a flexible delta wing*. 2004.

18. Jin-Jun, W. and Z. Wang, *Experimental investigations on leading-edge vortex structures for flow over non-slender delta wings.* Chinese Physics Letters, 2008. 25: p. 2550.

19. Pagan D and S. JL., *Experimental study of the breakdown of a vortex generated by a delta wing.* La Recherche Aerospatiale (English Edition) 1986. 3: p. 29-51.

20. Kegelman, J.T. and F.W. Roos, *The flow fields of bursting vortices over moderately swept delta wings*, in *28th Aerospace Science Meeting*1990: Reno, NV.

21. Honkan, A. and J. Andreopoulos, *Instantaneous three-dimensional vorticity measurements in vortical flow over a delta wing.* AIAA Journal, 1997. 35(10): p. 1612-1620.

22. Payne, F.M., T.T. Ng, and R.C. Nelson, *Seven-hole probe measurement of leading edge vortex flows.* Experiments in Fluids, 1989. 7(1): p. 1-8.

23. Hall, M.G., *A theory for the core of a leading-edge vortex.* Journal of Fluid Mechanics, 1961. 11(02): p. 209-228.

24. Earnshaw, P., *Measurements of vortex-breakdown position at low speed on a series of sharp-edged symmetrical models.* ARC Reports & Memoranda No. 3424, 1964.

25. Menke, M. and I. Gursul, *Unsteady nature of leading edge vortices.* Physics of Fluids, 1997. 9: p. 2960.

26. Mitchell, A.M., et al., *Analysis of delta-wing vortical substructures using detached-eddy simulation.* AIAA Journal, 2006. 44(5): p. 964-972.

27. Devenport, W.J., et al., *The structure and development of a wing-tip vortex.* Journal of Fluid Mechanics, 1996. 312: p. 67-106.

28. Ol, M.V., *An experimental investigation of leading edge vortices and passage to stall of non-slender delta wings*, in Symposium on Advanced Flow Measurments 2003.

29. Gursul, I., *Recent developments in delta wing aerodynamics.* Aeronautical Journal, 2004. 108(1087): p. 437-452.

30. Green, S.I., ed. *Fluid Vortices*. 1995, Kluwer Academic Publisher.

31. Johari, H. and W.W. Durgin, *Direct measurement of circulation using ultrasound.* Experiments in Fluids, 1998. 25(5): p. 445-454.

32. Kaplan, S.M., A. Altman, and M. Ol, *Wake vorticity measurements for low aspect ratio wings at low Reynolds number.* Journal of Aircraft, 2007. 44(1): p. 241-251.

33. Verhaagen, N. and P. van Ransbeck. *Experimental and numerical investigation of the flow in the core of a leading edge vortex*. in Proceedings of 28th AIAA Aerospace Sciences Meeting. 1990. Reno, NV.

34. Delery, J.M., *Aspects of vortex breakdown.* Progress in Aerospace Sciences, 1994. 30(1): p. 1-59.

35. Payne, F.M. and R.C. Nelson, *An experimental investigation of vortex breakdown on a delta wing.* NASA Langley Research Center Vortex Flow Aerodynamics, 1986. 1: p. 135-161.

36. Pereira, J., *Experimental investigation of tip vortex control using a half-delta shaped tip strake.* Bulletin of the American Physical Society: 64th Annual Meeting of the APS Division of Fluid Dynamics, 2011. 56.

37. Wentz Jr, W.H. and D.L. Kohlman, *Vortex breakdown on slender sharp-edge wings.* Journal of Aircraft, 1971. 8(3): p. 156-161.

38. Jobe, C.E., *Vortex breakdown location over 65 degrees delta wings empiricism and experiment.* Aeronautical Journal, 2004. 108(1087): p. 475-482.

39. Kegelman, J.T. and F.W. Roos. *Effects of leading-edge shape and vortex burst on the flow field of a 70-degree-sweep delta wing*. in 27th Aerospace Science Meeting. 1989.

40. Luckring, J.M., *Reynolds number, compressibility, and leading-edge bluntness effects on delta-wing aerodynamics*, in 24th International Congress of the Aeronautical Sciences, 2004: Yokohama.

41. Verhaagen, N.G., *Leading-edge radius effects on aerodynamic characteristics of 50-degree delta wings.* Journal of Aircraft, 2012. 49(2): p. 521-531.
42. Younis, Y., et al., *Vortical flow topology on windward and leeward side of delta wing at supersonic speed.* Journal of Applied Fluid Mechanics, 2009. 2(2): p. 13-21.
43. Lowson, M.V. and A.J. Riley, *Vortex breakdown control by delta-wing geometry.* Journal of Aircraft, 1995. 32(4): p. 832-838.
44. Allan, M., et al., *Wind-tunnel interference effects on a 70 degree delta wing.* Aeronautical Journal, 2004. 108: p. 505-514.
45. Gursul, I., *Review of unsteady vortex flows over slender delta wings.* Journal of Aircraft, 2005. 42(2): p. 299.
46. Pelletier, A. and R.C. Nelson, *An experimental study of static and dynamic vortex breakdown on slender delta wing planforms.* AIAA 1994-1879, 1994: p. 534-544.
47. Soltani, M.R. and Bragg, M.B., *Measurements on an oscillating 70-degree delta wing in subsonic flow.* Journal of Aircraft, 1990. 27(3): p. 211-217.
48. Menke, M., H. Yang, and I. Gursul, *Experiments on the unsteady nature of vortex breakdown over delta wings.* Experiments in Fluids, 1999. 27(3): p. 262-272.
49. Kusunose, K., *Development of a universal wake survey data analysis code*, in *15th AIAA Applied Aerodynamics Conference* 1997.
50. Brune, G., *Quantitative low-speed wake surveys.* Journal of Aircraft, 1994. 31(2): p. 249-255.
51. Maskell, E., *Progress towards a method for the measurement of the components of the drag of a wing of finite span*, 1973, Royal Aircraft Establishment.
52. Polhamus, E.C., *Predictions of vortex-lift characteristics by a leading-edge suction analogy.* Journal of Aircraft, 1971. 8(4): p. 193-199.
53. Polhamus, E.C., *Charts for predicting the subsonic vortex-lift characteristics of arrow, delta, and diamond wings.* NASA TN D-6243, 1971.
54. Wentz, W.H. and D.L. Kohlman, *Wind tunnel investigations of vortex breakdown on slender sharp-edged wings*, 1969, University of Kansas,[Aerospace Engineering].
55. Al-Garni, A.Z., Saeed, F., and Al-Garni, A.M., *Experimental and numerical investigation of 65 degree delta and 65/40 degree double-delta wings.* Journal of Aircraft, 2008. 45(1): p. 71-76.

56. Thiede, P., ed. *Aerodynamic drag reduction technologies*. Proceedings of the CEAS/DragNet European Drag Reduction Conference Vol. 1. 2001, Springer-Verlag: Potsdam, Germany.

57. William Condon, S., *A wake integral method for experimnetal drag measurements and decomposition*, in *Department of Aeronautics and Astronautics*1994, Stanford University. p. 184.

58. Anderson, J.D., *Fundamental of Aerodynamics*2001.

59. Birch, D.M., *Investigation of the wingtip vortex behind an oscillating airfoil*, 2006, McGill University: Canada.

60. Wenger, C. and D. Devenport, *Seven-hole pressure probe calibration method utilizing look-up error tables: Aerodynamic measurement technology.* AIAA Journal, 1999. 37(6): p. 675-679.

61. Zilliac, G.G., *Calibration of seven-hole pressure probes for use in fluid flows with large angularity.* NASA STI/Recon Technical Report N, 1989. 90: p. 15399.

62. Zilliac, G.G., *Modelling, calibration, and error analysis of seven-hole pressure probes.* Experiments in Fluids, 1993. 14(1): p. 104-120.

63. Giles, M.B. and R.M. Cummings, *Wake integration for three-dimensional flowfield computations: Theoretical development.* Journal of Aircraft, 1999. 36(2): p. 357-365.

64. Lee, T. and Y. Su, *Wingtip vortex control via the use of a reverse half-delta wing.* Experiments in Fluids, 2012: p. 1-17.

65. Pereira, J.L., *Experimnetal investigation of tip vortex control using a half delta shaped tip strake*, 2012, McGill University: Canada.

66. Betz, A., *Verhalten von Wirbelsystemen.* ZAMM Journal of Applied Mathematics and Mechanics/Zeitschrift für Angewandte Mathematik und Mechanik (Translation included in NASA Technical Memorandum TM-71, 1932), 1932. 12(3): p. 164-174.

Appendix

6.1 Wake Survey Analysis

The following is a brief overview of the procedure but details can be found in Betz [66] and extended by Kusunose [49]. Control volume approach was adopted to formulate the drag integrals based on the conservation of linear momentum. The integral approach was subjected to a number of approximations, as follows

i. The incoming stream satisfies the free stream conditions
ii. Survey data belonged to singe traverse plane downstream of model
iii. Flow must be steady and incompressible, i.e. M < ~0.5
iv. No blowing or suction, i.e. solid surface assumption
v. Tunnel cross section must be constant, i.e. parallel wall assumption

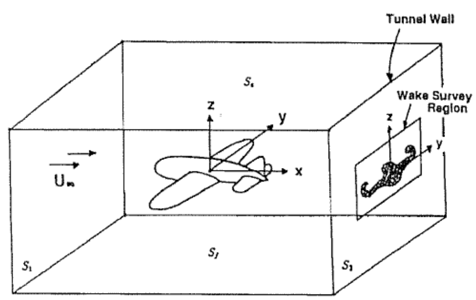

Figure 6.1-1 Control volume and coordinate system for drag formulation

The control volume shows the upstream (S1) and downstream (S2) traverse planes and the bounded wake region (WA). Applying momentum balance in x-direction, the drag integral can be formulated as;

$$D = \int\int_{S_1} (P + \rho u^2) dydz - \int\int_{S_2} (P + \rho u^2) dydz \qquad \text{A.1}$$

Here P is the static pressure and u is the axial/streamwise component of the velocity vector. On replacing the static pressure by total pressure

$$P_T = P + \frac{\rho}{2}(u^2 + v^2 + w^2) \qquad \text{A.2}$$

Keeping in view the assumption (i), equation (A.1) can be rewritten as

$$D = \int\int_{WA} (P_{T\infty} - P_T) dydz + \frac{\rho}{2}\int\int_{S_2} (U_\infty^2 - u^2 + v^2 + w^2) dydz \qquad \text{A.3}$$

Where WA denotes integral only over the vortical area[20], the equation can be more elucidating if written as

$$D = \int\int_{WA}(P_{T\infty} - P_T)dydz + \frac{\rho}{2}\int\int_{S_2}(U_\infty^2 - u^2)dydz + \frac{\rho}{2}\int\int_{S_2}(v^2 + w^2)dydz \qquad \text{A.4}$$

The drag integral constitutes of three distinct integrals; the first term reflects the pressure drag, the second term is profile drag and third represents the vortex/induced drag. Since there is no pressure loss outside the vortical region, therefore the first integral is zero in free-stream region. Note that to fulfill the computation requirements the second integral demands flow information over the complete tunnel cross section downstream of the body. In order to make the formulation consistent by limiting the integrals to vortical region only, Betz [66] introduced an artificial velocity, as follows

$$P_{T\infty} = P + \frac{\rho}{2}(u^{*2} + v^2 + w^2) \qquad \text{A.5}$$

The perturbation velocity is given by $u' = u^* - U_\infty$. The artificial velocity component "u*" correlates the axial velocity and local pressure profile only in wake region. Incorporating these definitions of in equation A.4, the drag integral simplifies to

$$\begin{aligned} D = \int\int_{WA}\Big[(P_{T\infty} - P_T)dydz + \frac{\rho}{2}\int\int_{S_2}(u^* - u)(u^* + u - 2U_\infty)dydz\Big] \\ + \frac{\rho}{2}\int\int_{S_2}(v^2 + w^2)dydz - \frac{\rho}{2}\int\int_{S_2}u'^2 dydz \end{aligned} \qquad \text{A.6}$$

This equation A.6 is derived by Maskell [51] as an extension of Betz [66] formulation. The first integral is used for C_{Dp}. It is to note that integral of perturbation velocity is over the entire plane therefore Maskell introduced a wake-blockage velocity, "u_b" given by

$$u_b = \frac{1}{2S_T}\int\int_{WA}(u^* - u)dydz \qquad \text{A.7}$$

Where ST is the wind tunnel cross-sectional area, rewriting the equation A.6 based on blockage velocity;

$$\begin{aligned} D = \int\int_{WA}\Big[(P_{T\infty} - P_T) + \frac{\rho}{2}(u^* - u)\{u^* + u - 2(U_\infty + u_b\}dydz\Big] \\ + \frac{\rho}{2}\int\int_{S_2}(v^2 + w^2)dydz \end{aligned} \qquad \text{A.8}$$

The first integral is now limited to wake region only and represents the profile drag (D_P) whereas the second integral is induced drag (D_i). The following formulation for the determination of induced drag has been extracted from Birch [66] and Pereira [72]. Maskell derived a procedure to resolve the latter by introducing the idea of scalar functions φ and ψ for planar velocities, i.e. v and w. He defined the following relations for the scalar functions; $v = \frac{\partial\emptyset}{\partial y} + \frac{\partial\psi}{\partial z}, w = \frac{\partial\emptyset}{\partial z} - \frac{\partial\psi}{\partial y}$

[20] Various approaches are used to identify the vortical area, e.g. closed contour encompassing vortex center and contour value of ~0.01% of absolute ζ_{peak}

Substituting these values in equation A.8

$$D_i = \frac{\rho}{2}\int\int_S \left(\frac{\partial \emptyset}{\partial y} + \frac{\partial \psi}{\partial z}\right)^2 + \left(\frac{\partial \emptyset}{\partial z} - \frac{\partial \psi}{\partial y}\right)^2 dydz \qquad \text{A.9}$$

This can be further simplified by using the Green's Theorem and introducing the axial vorticity ζ and source term σ to;

$$D_i = \frac{\rho}{2}\int\int_{wake} \psi\zeta - \phi\sigma\, dS \qquad \text{A.10}$$

In order the solve for the scalar functions, he pointed that the solution of ψ resulted in a Laplace and Poisson equation

$$\frac{\partial^2\psi}{\partial y^2} + \frac{\partial^2\psi}{\partial z^2} = -\zeta\ (inside\ the\ wake)\ \&\ 0(outside\ the\ wake)$$

This equation should be resolved over the entire downstream plane with boundary condition ψ = 0 along the tunnel intersections. The drag integral is subjected to following assumptions, a) Tunnel walls are streamlines, ψ (wall) = 0, b) No flow through the wall, $\frac{\partial\phi}{\partial n} = 0$. Therefore in order to compute the induced drag, four unknowns are required for each grid point (i, j) within the vortical region, i.e. ψ, ϕ, ζ, and σ. the vorticity and source term can be defined in terms of traverse velocities and, as mentioned, are calculated on the basis central difference method.

$$\zeta_{i,j} = \frac{\Delta w}{\Delta y} - \frac{\Delta v}{\Delta z} = \left(\frac{w_{i-1,j} - w_{i+1,j}}{2\eta}\right) - \left(\frac{v_{i,j+1} - v_{i,j-1}}{2\eta}\right) \qquad \text{A.10}$$

$$\sigma_{i,j} = \frac{\Delta v}{\Delta y} + \frac{\Delta w}{\Delta z} = \left(\frac{v_{i-1,j} - v_{i+1,j}}{2\eta}\right) + \left(\frac{w_{i,j+1} - w_{i,j-1}}{2\eta}\right) \qquad \text{A.11}$$

Where η = Δy = Δz, i = 2, 3 …n-1, j = 2, 3 …m-1, Similarly the stream function ψ and velocity potential ϕ were inferred on the basis of central difference method

$$\zeta_{i,j} \approx -\nabla^2\psi_{i,j} \approx -\frac{1}{\eta^2}\left(\psi_{i+1,j} + \psi_{i-1,j} - 4\psi_{i,j} + \psi_{i,j+1} + \psi_{i,j-1}\right) \qquad \text{A.12}$$

$$\sigma_{i,j} \approx -\nabla^2\phi_{i,j} \approx -\frac{1}{\eta^2}\left(\phi_{i+1,j} + \phi_{i-1,j} - 4\phi_{i,j} + \phi_{i,j+1} + \phi_{i,j-1}\right) \qquad \text{A.13}$$

Imposing the tunnel wall boundary conditions as follows

- Left wall j = 2
- Right wall j = m-1
- Ceiling i = n-1
- Floor i = 2

This will form a system of (n-2) x (m-2) equations and same number of unknowns which can be expressed in matrix form as $A\vec{x} = \vec{b}$ where A is a (n-2) x (m-2) by (n-2) x (m-2) matrix of coefficients, $\vec{x}$ is a vector of unknowns (ψ or ϕ) and $\vec{b}$ is a vector of unknowns (σ or ζ). This system of equation can be solved by inverting the matrix A multiplying by computed b vector shall result in x values but it is apparent that size of the matrix depends upon the grid of downstream traverse plane. In present study, at a reasonable resolution of ¼" the A matrix grows up to ~ [23936x23936] and hence can only be inverted with the help of supercomputing techniques. However, the computing misery can be relieved up to some extent by segregating the non-zero entries and therefore the matrix A was redefined by a (n-2) x (m-2) by 5 array system. Because from equation A.12-13 it is evident that maximum number of non-zero entries in one row can never exceed 5. It is to mention that every iterative process needs an initial guess where a close guess reduces the number of iterations. In present study an initial guess is provided by solving the system of equations for a coarser resolution, i.e. 1". This resulted in 'A' matrix of [1496 x 1496] which is easily invertible. In addition, an iterative successive over-relaxation (SOR) technique based on Gauss-Seidel method was applied to further reduce the computing time. The over-relaxation parameter used to speed up the convergence is;

$$\omega = \frac{4}{\sqrt{2 + \left[4 - \cos\frac{\pi}{m} + \cos\frac{\pi}{n}\right]^2}} \qquad \text{A.14}$$

And the values of $\vec{x}$ can be found by;

$$x_i = (1-\omega)XO_i + \frac{\omega\left(-\sum_{j=1}^{i-1} a_{i,j}x_j - \sum_{j=i+1}^{n\times m} a_{i,j}XO_j + b_i\right)}{a_{i,j}} \qquad \text{A.15}$$

x_i s value of $\vec{x}$ being computed, XO_i is the initial guess, $a_{i,j}$ is coefficient in A matrix, and b_i is a value in known $\vec{b}$ vector. This process will be repeated until the difference between successive iteration was less than the desired tolerance level. Once the values were computed, the total-induced drag can be estimated by plugging in the values;

$$D_i \approx \frac{\rho}{2}\sum_{i=2}^{n-1}\sum_{j=2}^{m-1}\left(\psi_{i.j}\zeta_{i,j} - \phi_{i.j}\sigma_{i.j})\eta^2\right) \qquad \text{A.15}$$

6.2 Indirect lift estimation

1. Lifting Line Theory: Summation of spanwise distribution of circulation

$$L = \rho_\infty U_\infty \int_{-b/2}^{b/2} \Gamma(z)dz$$

2. Kaplan [32] - Line Integral: Using the circulation computed from line integration of tangential velocity about the circles centered about vortex axis

$$L = \rho_\infty U_\infty \Gamma\, b'$$

Where b' is twice the distance between the observable core of wing vortex and wing centerline.

3. Kaplan - Stokes Integral: Using the circulation computed from integrating vorticity over a specified area encompassing vortex center